A&A 582, A31 (2015)
DOI: 10.1051/0004-6361/201424955

Astronomy & Astrophysics

Planck intermediate results

XXVIII. Interstellar gas and dust in the Chamaeleon clouds as seen by *Fermi* LAT and *Planck*⋆

Planck and Fermi Collaborations: P. A. R. Ade[79], N. Aghanim[55], G. Aniano[55], M. Arnaud[67], M. Ashdown[64,5], J. Aumont[55], C. Baccigalupi[78], A. J. Banday[85,9], R. B. Barreiro[61], N. Bartolo[28], E. Battaner[87,88], K. Benabed[56,84], A. Benoit-Lévy[21,56,84], J.-P. Bernard[85,9], M. Bersanelli[31,47], P. Bielewicz[85,9,78], A. Bonaldi[63], L. Bonavera[61], J. R. Bond[8], J. Borrill[12,81], F. R. Bouchet[56,84], F. Boulanger[55], C. Burigana[46,29,48], R. C. Butler[46], E. Calabrese[83], J.-F. Cardoso[68,1,56], J. M. Casandjian[67], A. Catalano[69,66], A. Chamballu[67,14,55], H. C. Chiang[25,6], P. R. Christensen[76,34], L. P. L. Colombo[20,62], C. Combet[69], F. Couchot[65], B. P. Crill[62,77], A. Curto[5,61], F. Cuttaia[46], L. Danese[78], R. D. Davies[63], R. J. Davis[63], P. de Bernardis[30], A. de Rosa[46], G. de Zotti[43,78], J. Delabrouille[1], F.-X. Désert[51], C. Dickinson[63], J. M. Diego[61], S. W. Digel[89], H. Dole[55,54], S. Donzelli[47], O. Doré[62,10], M. Douspis[55], A. Ducout[56,52], X. Dupac[37], G. Efstathiou[58], F. Elsner[56,84], T. A. Enßlin[72], H. K. Eriksen[59], E. Falgarone[66], F. Finelli[46,48], O. Forni[85,9], M. Frailis[45], A. A. Fraisse[25], E. Franceschi[46], A. Frejsel[76], Y. Fukui[24], S. Galeotta[45], S. Galli[56], K. Ganga[1], T. Ghosh[55], M. Giard[85,9], E. Gjerløw[59], J. González-Nuevo[61,78], K. M. Górski[62,90], A. Gregorio[32,45,50], I. A. Grenier[67,⋆⋆], A. Gruppuso[46], F. K. Hansen[59], D. Hanson[74,62,8], D. L. Harrison[58,64], S. Henrot-Versillé[65], C. Hernández-Monteagudo[11,72], D. Herranz[61], S. R. Hildebrandt[62], E. Hivon[56,84], M. Hobson[5], W. A. Holmes[62], W. Hovest[72], K. M. Huffenberger[22], G. Hurier[55], A. H. Jaffe[52], T. R. Jaffe[85,9], W. C. Jones[25], M. Juvela[23], E. Keihänen[23], R. Keskitalo[12], T. S. Kisner[71], R. Kneissl[36,7], J. Knoche[72], M. Kunz[16,55,2], H. Kurki-Suonio[23,41], G. Lagache[55], J.-M. Lamarre[66], A. Lasenby[5,64], M. Lattanzi[29], C. R. Lawrence[62], R. Leonardi[37], F. Levrier[66], M. Liguori[28], P. B. Lilje[59], M. Linden-Vørnle[15], M. López-Caniego[61], P. M. Lubin[26], J. F. Macías-Pérez[69], B. Maffei[63], D. Maino[31,47], N. Mandolesi[46,4,29], M. Maris[45], D. J. Marshall[67], P. G. Martin[8], E. Martínez-González[61], S. Masi[30], S. Matarrese[28], P. Mazzotta[33], A. Melchiorri[30,49], L. Mendes[37], A. Mennella[31,47], M. Migliaccio[58,64], M.-A. Miville-Deschênes[55,8], A. Moneti[56], L. Montier[85,9], G. Morgante[46], D. Mortlock[52], D. Munshi[79], J. A. Murphy[75], P. Naselsky[76,34], P. Natoli[29,3,46], H. U. Nørgaard-Nielsen[15], D. Novikov[52], I. Novikov[76], C. A. Oxborrow[15], L. Pagano[30,49], F. Pajot[55], R. Paladini[53], D. Paoletti[46,48], F. Pasian[45], O. Perdereau[65], L. Perotto[69], F. Perrotta[78], V. Pettorino[40], F. Piacentini[30], M. Piat[1], S. Plaszczynski[65], E. Pointecouteau[85,9], G. Polenta[3,44], L. Popa[57], G. W. Pratt[67], S. Prunet[56,84], J.-L. Puget[55], J. P. Rachen[18,72], W. T. Reach[86], R. Rebolo[60,13,35], M. Reinecke[72], M. Remazeilles[63,55,1], C. Renault[69], I. Ristorcelli[85,9], G. Rocha[62,10], G. Roudier[1,66,62], B. Rusholme[53], M. Sandri[46], D. Santos[69], D. Scott[19], L. D. Spencer[79], V. Stolyarov[5,64,82], A. W. Strong[73], R. Sudiwala[79], R. Sunyaev[72,80], D. Sutton[58,64], A.-S. Suur-Uski[23,41], J.-F. Sygnet[56], J. A. Tauber[38], L. Terenzi[39,46], L. Tibaldo[89], L. Toffolatti[17,61,46], M. Tomasi[31,47], M. Tristram[65], M. Tucci[16,65], G. Umana[42], L. Valenziano[46], J. Valiviita[23,41], B. Van Tent[70], P. Vielva[61], F. Villa[46], L. A. Wade[62], B. D. Wandelt[56,84,27], I. K. Wehus[62], D. Yvon[14], A. Zacchei[45], and A. Zonca[26]

(Affiliations can be found after the references)

Received 10 September 2014 / Accepted 25 February 2015

ABSTRACT

The nearby Chamaeleon clouds have been observed in γ rays by the *Fermi* Large Area Telescope (LAT) and in thermal dust emission by *Planck* and IRAS. Cosmic rays and large dust grains, if smoothly mixed with gas, can jointly serve with the H I and ^{12}CO radio data to (i) map the hydrogen column densities, $N_{\rm H}$, in the different gas phases, in particular at the dark neutral medium (DNM) transition between the H I-bright and CO-bright media; (ii) constrain the CO-to-H_2 conversion factor, $X_{\rm CO}$; and (iii) probe the dust properties per gas nucleon in each phase and map their spatial variations across the clouds. We have separated clouds at local, intermediate, and Galactic velocities in H I and ^{12}CO line emission to model in parallel the γ-ray intensity recorded between 0.4 and 100 GeV; the dust optical depth at 353 GHz, τ_{353}; the thermal radiance of the large grains; and an estimate of the dust extinction, A_{VQ}, empirically corrected for the starlight intensity. The dust and γ-ray models have been coupled to account for the DNM gas. The consistent γ-ray emissivity spectra recorded in the different phases confirm that the GeV–TeV cosmic rays probed by the LAT uniformly permeate all gas phases up to the ^{12}CO cores. The dust and cosmic rays both reveal large amounts of DNM gas, with comparable spatial distributions and twice as much mass as in the CO-bright clouds. We give constraints on the H I-DNM-CO transitions for five separate clouds. CO-dark H_2 dominates the molecular columns up to $A_V \simeq 0.9$ and its mass often exceeds the one-third of the molecular mass expected by theory. The corrected A_{VQ} extinction largely provides the best fit to the total gas traced by the γ rays. Nevertheless, we find evidence for a marked rise in $A_{VQ}/N_{\rm H}$ with increasing $N_{\rm H}$ and molecular fraction, and with decreasing dust temperature. The rise in $\tau_{353}/N_{\rm H}$ is even steeper. We observe variations of lesser amplitude and orderliness for the specific power of the grains, except for a coherent decline by half in the CO cores. This combined information suggests grain evolution. We provide average values for the dust properties per gas nucleon in the different phases. The γ rays and dust radiance yield consistent $X_{\rm CO}$ estimates near 0.7×10^{20} cm^{-2} K^{-1} km^{-1} s. The A_{VQ} and τ_{353} tracers yield biased values because of the large rise in grain opacity in the CO clouds. These results clarify a recurrent disparity in the γ-ray versus dust calibration of $X_{\rm CO}$, but they confirm the factor of 2 difference found between the $X_{\rm CO}$ estimates in nearby clouds and in the neighbouring spiral arms.

Key words. ISM: structure – gamma rays: ISM – cosmic rays – dust, extinction – local insterstellar matter

⋆ Appendices are available in electronic form at http://www.aanda.org

⋆⋆ Corresponding author: I. Grenier, isabelle.grenier@cea.fr

1. Introduction

The interstellar gas reserves of the Milky Way are commonly evaluated by means of a large set of multiwavelength tracers. Frequently used are the ubiquitous 21 cm line emission from atomic hydrogen (H I, see Kalberla et al. 2010), the widespread 2.6 mm line emission from ^{12}CO as a proxy for H_2 molecules (Dame et al. 2001; Planck Collaboration XIII 2014), submillimetre to infrared thermal emission from dust grains mixed with the gas (Planck Collaboration XXI 2011), and γ rays with energies above a few hundred MeV spawned by cosmic rays (CRs) permeating the gas and interacting with its nucleons (Strong et al. 1988). Knowledge of the mass, physical state, volume distribution, and dynamics of the different gas phases is the key to understanding the life cycle of the interstellar medium (ISM) in our Galaxy. To this end we need to carefully investigate the validity domain of the total-gas tracers and to quantify their departure from a linear behaviour due to radiation transfer and/or environmental evolution. In this context, the synergy between the *Planck*[1] and *Fermi* LAT all-sky surveys offers new perspectives to study the properties and limitations of these tracers in the multi-phase complexity of clouds down to parsec scales in the solar neighbourhood.

1.1. Specific goals

The ISM is optically thin to thermal dust emission at far infrared to millimetre wavelengths. The emission arises from large grains in thermal equilibrium with the ambient interstellar radiation field (ISRF). Several studies have reported an apparent increase in dust emissivity (intensity radiated per gas nucleon) and opacity (optical depth per gas nucleon) with increasing gas column density in both the atomic and molecular gas (Stepnik et al. 2003; Planck Collaboration XXIV 2011; Martin et al. 2012; Roy et al. 2013; Ysard et al. 2013; Planck Collaboration XI 2014; Planck Collaboration Int. XVII 2014). Interestingly, this might be a hint of dust evolution across the gas phases. Alternatively, dust opacities can be underestimated because of irradiation and temperature changes along the lines of sight, and overestimated by underrating the total gas for reasons that include significant H I opacity, insufficient sensitivity to CO emission, significant amounts of CO-dark H_2, and opaque CO in dense regions. In this context, the joint analysis of the interstellar γ radiation and thermal dust emission can help constrain the total gas column density, $N_{\rm H}$, in order to follow variations of the dust properties.

For a uniform CR irradiation through a cloud, the γ rays provide a measure of the total gas, regardless of its thermodynamic and chemical state, and without absorption limitations across the whole Galaxy. They thereby give valuable insight into (i) saturation corrections to $N_{\rm H\,I}$ column densities in the cloud; (ii) the in-situ CO-to-H_2 conversion for the derivation of H_2 column densities; and (iii) the mass content of the dark neutral medium (DNM) that escapes radio and millimetre surveys in the form of optically thick H I and/or CO-dark H_2. Irregular CR depletion or concentration inside a cloud can be tested using spectral variations because of the energy dependent propagation of the particles through the magnetic field as they resonantly diffuse on small-scale magnetic turbulence or by focusing or mirroring on the larger-scale structure of the magnetic field. The current γ-ray observations span two to three decades in particle energy and can be used to test these effects.

The integrated $J = 1 \rightarrow 0$ CO line intensity, $W_{\rm CO}$, is often assumed to scale linearly with the $N_{\rm H_2}$ column density (Dame et al. 1987), but the value of the conversion factor, $X_{\rm CO} \equiv N_{\rm H_2}/W_{\rm CO}$, remains uncertain, both in the solar neighbourhood (Abdo et al. 2010; Pineda et al. 2010; Planck Collaboration XIX 2011; Ackermann et al. 2012a) and at large scales in the Galaxy along the metallicity and UV-flux gradients (Strong et al. 2004; Abdo et al. 2010; Ackermann et al. 2011b; Pineda et al. 2013; Bolatto et al. 2013). Cloud-to-cloud variations in average $X_{\rm CO}$ can reflect dynamical differences in the relative mass contained in the molecular envelopes (more exposed to CO photodissociation, thus with a higher $X_{\rm CO}$) and in well-shielded cores (with lower $X_{\rm CO}$, Sheffer et al. 2008). Dust and γ-ray proxies for the total gas have been used separately to measure $X_{\rm CO}$ in different locations, at different angular resolutions, and with different methods, leading to discrepant values (see Bolatto et al. 2013, for a review of past references). We aim to compare the calibration of $X_{\rm CO}$ with dust and γ rays in the same cloud and with the same method for the first time.

At the atomic-molecular interface of the ISM, a combination of H I and H_2 gas with little or no CO can escape the H I and CO surveys because of high levels of H I self-absorption and low levels of CO excitation. Such a mix of DNM has been theoretically predicted in translucent clouds ($1 \leq A_V \leq 5$ mag) or translucent envelopes of giant molecular clouds (van Dishoeck & Black 1988). In this zone, a large fraction of H_2 is associated with C^0 and C^+ instead of with CO because H_2 is more efficient at self-shielding against UV dissociation than CO. The lack of correlation between the OH column-density and $W_{\rm CO}$ suggests large quantities of H_2 that are either unseen in CO surveys (Barriault et al. 2010; Allen et al. 2012) or detectable only by summing lines over wide regions without any mapping (Pineda et al. 2010).

The γ-ray studies have revealed the ubiquity of the DNM, both in mass fraction and spatial extent (Grenier et al. 2005). In the solar neighbourhood, it appears to be as extended as the dense H I and as massive as the CO-bright H_2. Recent analyses of *Fermi* data have confirmed its ubiquity in nearby clouds (Abdo et al. 2010; Ackermann et al. 2012a). It contributes almost one million solar masses in the star-forming complex of Cygnus X (Ackermann et al. 2012b). The DNM presence has been repeatedly suggested in dust studies as emission excesses over the $N_{\rm H\,I}$ and $W_{\rm CO}$ expectations (Blitz et al. 1990; Reach et al. 1994, 1998; Magnani et al. 2003; Lee et al. 2012; Planck Collaboration XXI 2011). According to the *Planck* data, little CO emission has been missed outside the boundaries of the present 2.6 mm surveys, down to a sensitivity of 1 or 2 K km s^{-1} (Planck Collaboration XIII 2014). Fainter CO cannot account for the brightness of the excesses seen off the Galactic plane (Planck Collaboration XIX 2011). DNM mass fractions, however, remain uncertain for various causes: from dust emission because of the potential emissivity variations mentioned above (Planck Collaboration XXI 2011; Planck Collaboration XIX 2011); from dust stellar reddening because of the uncertain colour distribution of the background star population, the contamination of unreddened foreground stars, and some incompleteness along the lines of sight (Paradis et al. 2012; Ackermann et al. 2012b); and from C^+ line emission at 158 μm because of the difficult separation of the contributions from the DNM, the atomic cold neutral medium (CNM), and photon-dominated regions (PDR; Pineda et al. 2013; Langer et al. 2014).

[1] *Planck* (http://www.esa.int/Planck) is a project of the European Space Agency (ESA) with instruments provided by two scientific consortia funded by ESA member states (in particular the lead countries France and Italy), with contributions from NASA (USA) and telescope reflectors provided by a collaboration between ESA and a scientific consortium led and funded by Denmark.

In this context, we aim to couple the total gas tracing capability of the CRs and of dust emission to extract reliable column densities in the DNM and to characterize the transition between the H I-bright, DNM, and CO-bright media in a nearby cloud complex.

1.2. Choice of cloud

With its proximity, its moderate molecular mass of the order of 10^4 $M_\odot$ (Mizuno et al. 2001), and its moderate star-formation activity, the Chamaeleon-Musca complex provides a useful target to probe gas tracers in the 10^{20-22} cm^{-2} range in $N_{\rm H}$. The clouds lie at distances of 140−180 pc (Mizuno et al. 2001) or 120−150 pc (Corradi et al. 2004). We adopt a distance of 150 pc for mass derivations, but we note that the $N_{\rm H}$ measurements do not depend on this choice.

Because of its location at relatively high Galactic latitudes and with typical linear sizes of 10−20 pc, variations in column density are more likely to reflect changes in volume density than pile-up along the line of sight or confusion with background structures. The available observations have angular resolutions ranging from 5′ to 15′ that limit the cross-talk between the structures of the different gas phases.

The Chamaeleon clouds should be bathed in a relatively uniform ISRF. The lack of OB stellar clusters ensures a relatively quiet environment in terms of: (i) UV irradiation for dust heating; (ii) photo-ionization with little H II mass; (iii) stellar-wind turbulence for standard CR diffusion (unlike in the turbulent Cygnus X, Ackermann et al. 2011a); and (iv) lack of internal CR sources in the form of supernova remnants. Early *Fermi* LAT analyses have shown that the clouds are pervaded by a CR flux close to the average in the local ISM and with an energy spectrum, the so-called Local Interstellar Spectrum (LIS), that is consistent with particle measurements in the solar system (Ackermann et al. 2012a).

The derivation of the dust spectral energy distribution (SED) so far from the ecliptic plane is minimally affected by uncertainties in the zodiacal light removal from the IRAS and *Planck* data (Planck Collaboration XI 2014). The subtraction of the cosmological microwave background and fluctuations in the cosmic infrared background do not significantly affect the bright SEDs (Planck Collaboration XI 2014). The clouds also lie conveniently away from the *Fermi* bubbles that dominate the γ-ray sky at energies above a few GeV (Su et al. 2010; Ackermann et al. 2014).

1.3. Analysis rationale

We can take advantage of the sensitivity, angular resolution, and broad frequency coverage of *Planck* and *Fermi* LAT to reassess the relationship between GeV γ rays, dust emission, and H I and CO line intensities. We defer the joint analysis of γ rays and dust extinction or reddening to later work. We use instead two spectral characterizations of the dust thermal emission recently proposed to match the *Planck*, IRAS, and Wide-field Infrared Survey Explorer (WISE) data. The first is based on modified blackbody spectra parametrized by the optical depth at 353 GHz, τ_{353}, the temperature T, and spectral index β (Planck Collaboration XI 2014). The second uses the physical model of Draine & Li (2007) to estimate the dust optical extinction and to renormalize it according to the starlight intensity ($U_{\rm min}$, defined in Sect. 2.2) to better match reddening measurements from quasars (Planck Collaboration Int. XXIX 2015). We denote this corrected extinction A_{VQ} hereinafter. To follow spatial variations in the dust heating rate, we have also considered a third dust tracer, the radiance R, which is the bolometric integral of the thermal intensity (Planck Collaboration XI 2014).

The atomic gas largely dominates the mass budget. Consequently it is the largest contributor to the γ-ray and dust signals. Atomic clouds in different locations and states may have different CR or dust content, so we have developed a careful kinematical separation of the different H I structures present in the region under study. We have distinguished the H I gas associated with the star-forming CO clouds, an intermediate-velocity H I arc crossing the field, and the Galactic H I background.

The γ-ray emission detected toward the Chamaeleon region is shown in Fig. 1. It is dominated by hadronic interactions between CR and gas nuclei. The ISM itself is transparent to γ rays at these energies. Earlier studies have indicated that the bulk of the Galactic CRs radiating in the energy bands selected for this work have diffusion lengths far exceeding typical cloud dimensions (Hunter et al. 1997; Abdo et al. 2010; Ackermann et al. 2011b). They also indicate an efficient CR penetration in all the gas phases studied here (H I, DNM, and CO-bright). The interstellar part of the γ-ray emission can therefore be modelled, to first order, as a linear combination of the gas column densities summed for the various gas phases and different clouds present along the lines of sight. The γ-ray intensity $I(l, b, E)$ in the (l, b) Galactic direction and at energy E can be expressed as $I(l, b, E) = \sum_{i\in\{\rm HI1,HI2,...,CO,DNM\}} q_i(E)\, N_i(l, b) + \ldots$ The $q_i(E)$ parameters are to be determined by fits to the *Fermi* data. They bear information on the CR flux and gas mass in the different interstellar structures. The model includes other sources of non-gaseous origin (e.g. point sources) that are detailed in Sect. 3.2.

The ISM is also optically thin to the thermal emission of large dust grains. For a uniform dust-to-gas mass ratio, $R_{\rm DG}$, and uniform mass emission coefficient, κ_ν, of the grains in a cloud, the dust column density can be modelled to first order as a linear combination of the gas column densities in the different phases and clouds: if we denote with $D \in \{A_{VQ}, \tau_{353}, R\}$ any of the three dust tracers, we can express it as $D(l, b) = \sum_{i\in\{\rm HI1,HI2,...,CO,DNM\}} y_i\, N_i(l, b) + \ldots$ The y_i coefficients are to be fitted to the data of the $D(l, b)$ tracer. They give measures of the average dust properties per gas nucleon in the different interstellar structures, namely the $A_{VQ}/N_{\rm H}$ ratio, the opacity $\tau_{353}/N_{\rm H}$ at 353 GHz, and the specific power $4\pi R/N_{\rm H}$ of the grains. The models are detailed in Sect. 3.3.

The interstellar γ-ray emission and the dust tracers shown in Fig. 1 exhibit very strong structural similarities. They reflect the common presence of CRs and dust in the H I and CO bright media, but also in the DNM, for which we have no independent template. This inconspicuous phase, however, shows up jointly as γ-ray and dust emission excesses over $N_{\rm H\,I}$ and $W_{\rm CO}$ expectations, with comparable spatial distributions. We have therefore iteratively coupled the γ-ray and dust models to account for the DNM contribution to the total gas. The method is described in Sect. 3.4. The use of the γ rays and of three different dust tracers enables tests of the robustness of the DNM reconstruction.

In order to show the spatial distributions of the dust and γ rays at the angular resolution sampled by the LAT, we have convolved the dust maps with the energy-dependent response of the LAT. To do so, we have assumed the γ-ray emissivity spectrum $q_{\rm LIS}$ of the local interstellar matter. The maps of the LAT-averaged quantities, $\tilde{A}_{VQ}$, $\tilde{\tau}_{353}$, and $\tilde{R}$, are shown in Fig. 1 for the overall energy band. They illustrate the close resemblance in spatial distribution between the dust and γ-ray photon counts of interstellar origin. Figure 1 also shows that the three dust maps largely agree on the overall distribution of the grains at

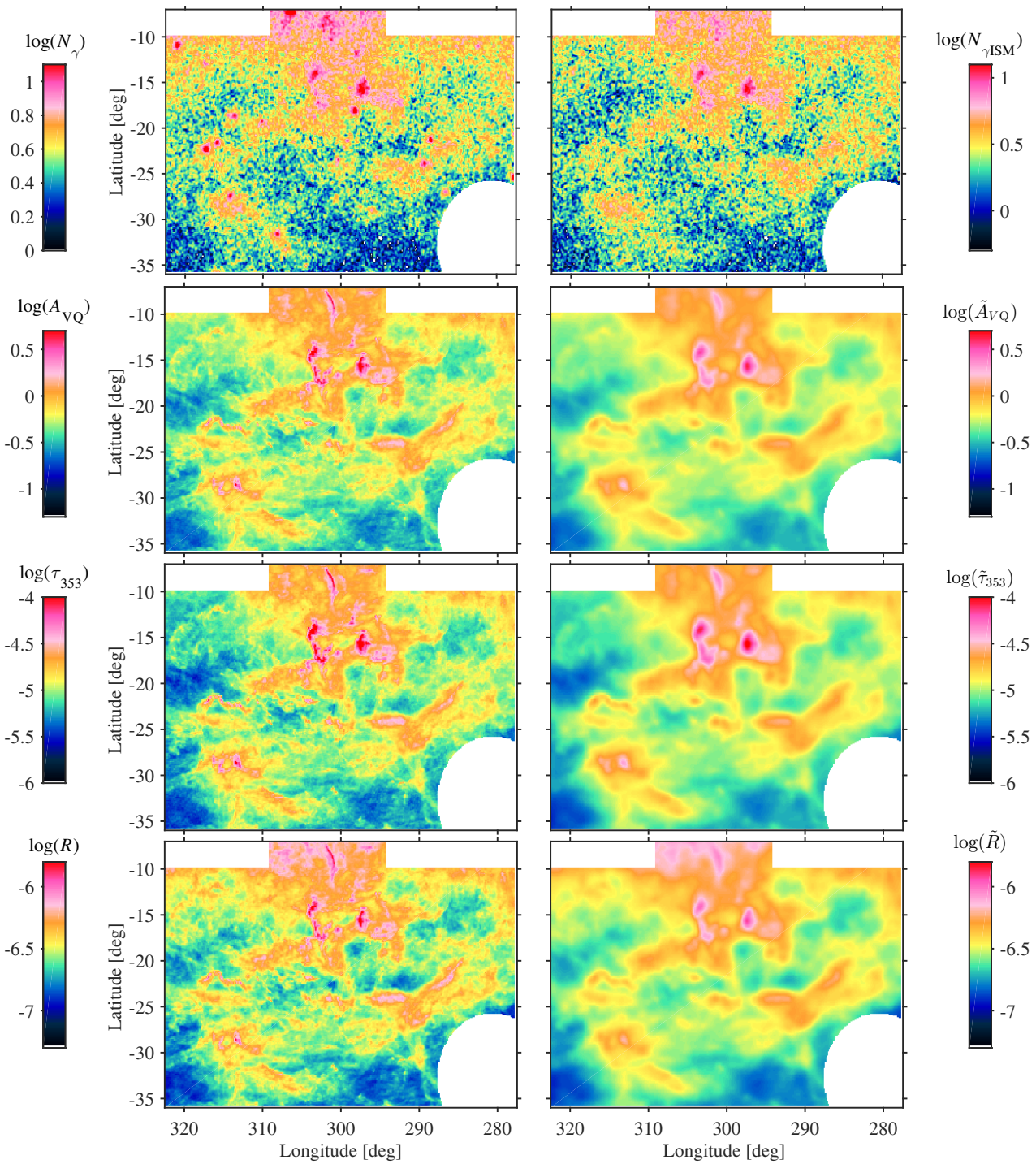

Fig. 1. Maps toward the Chamaeleon region of the γ-ray counts recorded in the 0.4−100 GeV band and of the dust quantities (modified extinction A_{VQ} in magnitudes, optical depth τ_{353}, and radiance R in W m^{-2} sr^{-1}). The total γ-ray photon counts are shown *on the left* and those spawned by cosmic-ray interactions with gas (after subtraction of other ancillary components) *on the right*. The γ-ray maps have been constructed on a 7.′5 pixel grid and smoothed with a Gaussian kernel of 0.′1 for display. The dust quantities are shown at 5′ resolution in *the left panels*, and at the *Fermi* LAT resolution *on the right* (after convolution with the energy-dependent response function of the LAT, assuming the local interstellar γ-ray spectrum over the 0.4−100 GeV band, tilded variables). Regions excluded from the analysis have been masked out.

the original 5′ resolution, but that they significantly differ in contrast (see e.g. at latitudes $b > -15°$). The radiance has 3 times less dynamical range than the optical depth, in particular toward the densest molecular zones. The dynamical range of A_{VQ} is intermediate between that in R and τ_{353}. These differences are still present when seen at the LAT resolution. They signal potential variations of the dust properties per gas nucleon that can be tested against the independent γ rays.

1.4. Contents

The paper is organized as follows. Section 2 presents the γ-ray, dust, H I, and CO data; Sect. 3 summarizes the models developed to study the H I, CO, and DNM contributions to the dust and γ-ray data, and how the DNM templates are built. In Sect. 4, we describe the results of the model fits, their errors, and the impact of the H I optical depth correction. Sections 5 and 6 focus on

the CR spectrum pervading the different gas phases and on the column-density maps inferred for the DNM. In Sects. 7 and 8 we discuss the results on the $X_{\rm CO}$ factors and the average dust properties in each phase. In Sect. 9, we present evidence for a marked evolution in dust opacity and a milder evolution in $A_{V\rm Q}/N_{\rm H}$ ratio and specific power as the gas becomes denser. In Sect. 10, we discuss the transitions between the different gas phases in five separate clouds within the local complex. We summarize the main conclusions and discuss follow-on studies in the last section. Appendices A to E present additional information on the kinematical separation of the H I structures, checks on the $W_{\rm CO}$ calibration, fits without a DNM contribution, and the table of q_i and y_i coefficients.

2. Data

We have selected a region around the Chamaeleon complex at Galactic longitudes $277.5° \leq l \leq 322.5°$ and latitudes $-36° \leq b \leq -7°$, and we have masked a disc around the Large Magellanic Cloud and toward regions with large contamination from gas in the Galactic disc, at $-10° \leq b \leq -7°$ and $l < 294°$ or $l > 309°$. The analysis region is shown in Fig. 1. We have selected a broad region to provide enough contrast in the diffuse H I gas. All maps are projected on the same 0.125°-spaced Cartesian grid as that of the CO survey from the Harvard-Smithsonian Center for Astrophysics (CfA). A finer grid would oversample the Parkes Galactic All Sky Survey (GASS, McClure-Griffiths et al. 2009) H I data and yield too many empty bins, with zero photons, at high energy in γ rays.

2.1. γ-ray data

We have analysed five years of LAT survey data, starting on 5 August 2008. We have applied tight rejection criteria (CLEAN class selection, photon arrival directions within 100° of the Earth zenith and time intervals when the LAT rocking angle was below 52°) in order to reduce the contamination by residual CRs and γ rays from the Earth atmospheric limb (see Nolan et al. 2012 for details). To improve the LAT angular resolution below 1.6 GeV, we have kept only the photons that converted to pairs in the front section of the tracker (Atwood et al. 2009). At higher energy, we took all photons that produced pairs in the front and back sections of the tracker. We have used the reprocessed Pass 7 photon data, its associated instrument response functions (IRFs, version P7REP-V15) and the related isotropic spectrum[2]. The LAT exposure was calculated for the adopted photon selection with the RELEASE-09-32-05 of the LAT Science Tools[3]. Systematic errors on the LAT sensitive area increase from 5% to 10% with energy over the 0.4−100 GeV range selected for the analysis (Ackermann et al. 2012c).

We have calculated the effective point-spread-function (PSF), the exposure map, the γ-ray emissivity spectrum $q_{\rm LIS}$ of the local interstellar gas (Casandjian 2012) and the spectrum of the isotropic background in 12 energy bins, with a bin width of 0.2 dex, and centred from $10^{2.7}$ to $10^{4.9}$ MeV. To ensure statistics robust enough to follow details in the spatial distributions of the different interstellar components, we have analysed the data in 4 broader and independent energy bands, bounded by $10^{2.6}$, $10^{2.8}$, $10^{3.2}$, $10^{3.6}$, and 10^{5} MeV. We have also analysed the entire $10^{2.6}$−10^{5} MeV interval as a single band. The LAT energy resolution decreases from 15% to 8% across these energies. Given the large width of the analysis bands, we have not corrected the fluxes for the energy resolution.

The LAT PSF is strongly energy-dependent (Atwood et al. 2009). For the local interstellar spectrum (LIS), the half widths at half maximum of the effective PSF are respectively 0.°44, 0.°27, 0.°16, 0.°07 with increasing energy in the four bands, and 0.°14 in the overall band. To account for the spillover of γ-ray emission produced outside the analysis region, we have modelled both point sources and interstellar contributions in a region 4° wider than the region of analysis. This choice corresponds to the 99.5% containment radius of the PSF in the lowest energy band.

The observed γ-ray emission also includes a contribution from the large-scale Galactic inverse Compton (IC) emission emanating from the interactions of CR electrons with the ISRF. It can be modelled with GALPROP[4], version 5.4. The run 54-LRYusifovXCO4z6R30-Ts150-mag2 has been tested against the LAT data (Ackermann et al. 2012d). It assumes a 30 kpc radius for the Galaxy and a radial distribution of CR sources such as pulsars in the Galactic plane. The particles are allowed to diffuse in the plane and into a halo that is 4 kpc high. We have used this run to generate an energy-dependent template of the Galactic inverse Compton emission across the field of view.

2.2. Dust data

We have used the all-sky maps of the dust optical depth τ_{353}, temperature T, and spectral index β, which were constructed at an angular resolution of 5′ from the combined analysis of the *Planck* 857, 545, and 353 GHz data, and of the IRAS 100 μm data (product release 5, Planck Collaboration XI 2014). Compared to previous works (e.g. Schlegel et al. 1998), the use of the *Planck* data has greatly improved in precision and in angular resolution the spectral characterization of the dust emission, in particular in regions of large temperature contrast inside molecular clouds and near stellar clusters or IR sources. We summarize here important aspects of this characterization.

Modified blackbody intensity spectra, $I_\nu = \tau_{\nu_0} B_\nu(T)(\nu/\nu_0)^\beta$, where $B_\nu(T)$ is the Planck function for dust at temperature T, were fitted to the observed SED in each direction. The fits were performed at 30′ resolution with τ_{ν_0}, T, and β as free parameters. The fits were then repeated at 5′ resolution by fixing β as obtained in the first step. This procedure limited the noise impact on the T–β degeneracy. SEDs were checked to be consistent with the data at all frequencies (see Fig. 11 in Planck Collaboration XI 2014), in particular in bright interstellar areas such as the Chamaeleon region. We note that the contamination from CO line emission in the 353 GHz filter band, amounting to a few per cent of the signal, was not removed, so as to avoid adding large noise in all directions away from CO clouds.

The derivation of the optical depth, τ_ν, and opacity, σ_ν, at frequency ν follows the relations

$$\tau_\nu = \frac{I_\nu}{B_\nu(T)} = \sigma_\nu N_{\rm H} = \kappa_0 \left(\frac{\nu}{\nu_0}\right)^\beta R_{\rm DG}\, \mu_{\rm H} N_{\rm H} \quad (1)$$

for the observed specific intensity I_ν of the dust emission, the Planck function $B_\nu(T)$ at temperature T, the hydrogen column density $N_{\rm H}$, the mean gas mass per hydrogen atom $\mu_{\rm H} = 2.27 \times 10^{-27}$ kg, the dust-to-gas mass ratio $R_{\rm DG}$, and

[2] http://fermi.gsfc.nasa.gov/ssc/data/access/lat/BackgroundModels.html

[3] The Science Tools are available from the *Fermi* Science Support Center, http://fermi.gsfc.nasa.gov/ssc/

[4] http://galprop.stanford.edu/

the mass emission or absorption coefficient κ_0 at reference frequency ν_0. We have used the map of optical depth, τ_{353}, estimated at 353 GHz, and its associated uncertainty.

The radiance, in W m^{-2} sr^{-1}, gives the integral in frequency of the thermal spectrum and it relates to the specific power, Π, radiated per gas nucleon as

$$R = \tau_{353} \int_0^\infty \left(\frac{\nu}{\nu_{353}}\right)^\beta B_\nu(T)\mathrm{d}\nu = \frac{\Pi N_\mathrm{H}}{4\pi}. \quad (2)$$

We have propagated the errors on τ_{353}, T, and β to calculate the uncertainties on the radiance. These uncertainties are upper limits to the real values, since we could not include the negative covariance terms between the anti-correlated T and β (Planck Collaboration XI 2014). Within the region of analysis, the optical depth uncertainties range from 2% to 4% and the radiance uncertainties range from 10% to 20%, with a strong peak in frequency around 14%.

The dust model of Draine & Li (2007) has also been fitted to the SEDs recorded by *Planck*, IRAS, and WISE from 12 to 850 μm (Planck Collaboration Int. XXIX 2015). All-sky maps were thereby constructed for the mass surface density of the dust, the optical extinction, the mass fraction locked up in PAH grains, and the lower U_min cutoff in the U^{-2} distribution of starlight intensities heating the bulk of the grains. The comparison between the resulting extinction values and independent estimates based on quasar colours has revealed deviations that significantly correlate with U_min. The modelled extinction has thus been renormalized according to U_min to compensate for this bias (Planck Collaboration Int. XXIX 2015). For our work, we have used the renormalized A_{VQ} extinction map at 5′ resolution (denoted QDL07 by Planck Collaboration Int. XXIX 2015). We stress that A_{VQ} is a quantity drawn from the thermal emission of the grains, in spite of its absorption-related name. We also note that the physical parameters of the Draine & Li (2007) model yield poorer fits to the observed SEDs than modified blackbody spectra. Nonetheless, we show below that, after renormalization, the A_{VQ} map is better correlated with the interstellar γ rays than the optical depth deduced from the modified blackbody characterization (see Fig. 1 and the results in Sect. 3).

The τ_{353}, radiance, and A_{VQ} maps have been derived with the *Planck* data from the first release. We have checked that the results of the present work are not significantly changed when we use the most recent version of the *Planck* data available within the Planck consortium.

2.3. HI data and kinematical component separation

The H I Galactic All Sky Survey (GASS) is the most sensitive and highest resolution survey of 21 cm line emission of the southern sky (McClure-Griffiths et al. 2009). We have used the GASS data corrected for stray radiation, instrumental baselines and radio interference contamination, and with both IFs to remove the negative ghosts occasionally caused in frequency-switching mode by the presence of high-velocity-cloud lines in one of the bands (Kalberla et al. 2010). We have used the GASS data server[5] to resample the original data cubes onto our spatial grid. Our choice of 0.′1 for the Gaussian interpolation kernel gives an effective full width at half maximum (FWHM) resolution of 14.′5 and a root-mean square (rms) noise of 0.07 K per channel. We have kept the original velocity resolution of 0.82 km s^{-1} in the 3D (longitude, latitude, velocity) cube.

[5] http://www.astro.uni-bonn.de/hisurvey/gass/index.php

All velocities mentioned hereinafter are given with respect to the local standard of rest.

Line profiles in the 3D cube have been used to kinematically separate the four main structures that can be distinguished in velocity (see Fig. A.1), namely:

- the local atomic gas in the Chamaeleon complex;
- the gas in an intermediate velocity arc (IVA), crossing the whole region around −25° in latitude;
- the more distant gas at large height above the Galactic plane;
- gas from the Large Magellanic Cloud (LMC) and its tidal tails.

The wide velocity range of the IVA component, spanning the $-40 \le v \le -4$ km s^{-1} interval, is due to very broad line wings in addition to a small velocity gradient along the structure. The origin and distance of this dynamically unusual cloud are unknown; it is half as massive as the nearby Chamaeleon region if it is at the same distance.

The four features are well defined in the longitude, latitude, velocity (l, b, v) cube, but they occasionally merge because of the gas dynamics and large line widths. In order to separate them, we have developed a specific separation scheme which is described in Appendix A. It is based on fitting each H I spectrum as a sum of lines with pseudo-Voigt profiles. The prior detection of line peaks and shoulders in each spectrum limits the number of lines to be fitted and it provides objective initial values for their velocity centroids. All fits match the data to better than 80 or 90% of the total intensity. In order to preserve the total intensity exactly, the small residuals between the modelled and observed spectra have been distributed among the fitted lines according to their relative strength in each channel.

We have defined 3D boundaries in longitude, latitude, and velocity for each of the four components. The spatial separations between the IVA and Galactic disc components on the one hand, and between the Galactic disc and LMC components on the other, run along curves of minimum intensity at medium latitudes. The details are given in Appendix A.

We have constructed the $N_\mathrm{H\,I}$ column-density map of each component by selecting the lines with centroids falling within the appropriate velocity interval, depending on the (l, b) direction, and by integrating their individual profiles in velocity. This procedure gives more reliable column-density estimates than a direct integration of the H I spectra over the chosen velocity interval. The difference is exemplified in the case of two partially overlapping lines with different peak temperatures. Integrating the observed spectrum in velocity on both sides of a boundary set between the lines would incorrectly attribute the intensity of the wings spilling over the boundary. The large over-(under-)estimation of $N_\mathrm{H\,I}$ from the weak (bright) line would affect the derivation of average cloud properties per gas nucleon in both components. The method used here corrects for the line spillover across velocity boundaries. It also avoids sharp spatial jumps across the resulting maps. This approach thereby enables the exploration of differences in CR and dust volume densities in different structures along the line of sight.

We have checked that changes in velocity cuts of a few km s^{-1} have little impact on the resulting $N_\mathrm{H\,I}$ maps. The lines of the local and IVA components strongly overlap in velocity around $l = 283°$ and $b = -25°$. Changing the velocity cut by 1 or 2 km s^{-1} results in a 3 to 6% change in the total mass in the corresponding velocity range. The difference arises mainly from the region of strong overlap.

We have integrated the line profiles for a given choice of spin temperature (T_s) to correct for the H I optical depth. The same

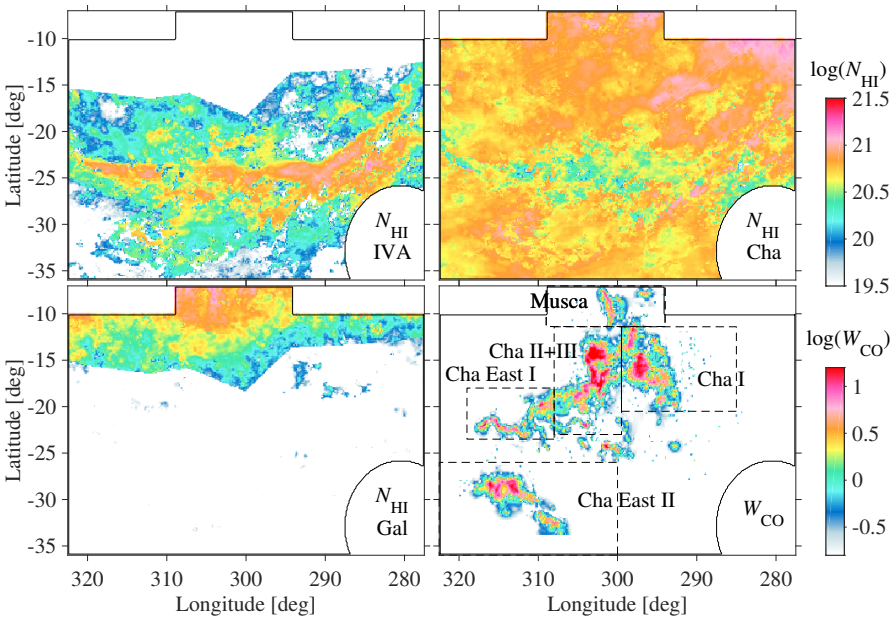

Fig. 2. Maps of the $N_{\rm H\,I}$ column densities (in cm^{-2}) and $W_{\rm CO}$ line intensities (in K km s^{-1}) obtained for different velocity components in the analysis region: $N_{\rm H\,I}$ for the intermediate velocity arc; $N_{\rm H\,I}$ and $W_{\rm CO}$ for the local Chamaeleon complex; and $N_{\rm H\,I}$ for the Galactic disc background. The $N_{\rm H\,I}$ column densities have been obtained for optically thin emission. The solid black contour marks the analysis region. The dashed rectangles outline the boundaries of the five substructures described in Sect. 2.5 and analysed in Sect. 10.

temperature correction has been applied to all H I components. In addition to the optically thin case, maps have been produced for uniform spin temperatures of 125, 200, 300, 400, 500, 600, 700, and 800 K.

The maps obtained for the optically thin case are shown in Fig. 2. Within the region of analysis, the local, IVA, and Galactic disc components exhibit a comparable range of column-densities, with peak values in slight excess of 10^{21} cm^{-2}. With comparable intensities, but distinct spatial distributions, they can be treated as independent components contributing to the overall dust or γ-ray emission.

We have checked that the anti-correlation that can be seen in Fig. 2 between the local and IVA components corresponds to the presence of two lines of different brightness along those directions. Examples are given in Appendix A. The trough that crosses the local Chamaeleon map is visible in Fig. A.1 at positive velocities prior to any component separation. One may speculate that a large-scale shock has expelled gas from the low velocity Chamaeleon region and caused both the anti-correlation and the unsually broad wings of the IVA lines.

2.4. ^{12}CO data

To trace the distribution of the ^{12}CO ($J = 1 \rightarrow 0$) emission at 115 GHz, we have used the NANTEN observations of the Chamaeleon clouds with a 2.′6 beam, 8′ spacing grid, 0.1 km s^{-1} velocity resolution, and a typical noise below 0.4 K per channel (Mizuno et al. 2001). Because of the undersampling, we have checked the NANTEN $W_{\rm CO}$ intensities against the fully sampled CfA survey data (8.′8 FWHM beam with 7.′5 spacing, from Boulanger et al. 1998) across the subset of clouds that have been observed by both instruments (Cham I, II, and III). After removing negative ghosts and flattening baselines in the NANTEN data cube (see Appendix C for details), we have obtained consistent intensities between it and data from the CfA survey. Unlike what was found in other high-latitude regions (Planck Collaboration XIX 2011), Fig. C.1 shows that the NANTEN and CfA photometries fully agree in this region. The derivation of the $X_{\rm CO}$ factor from the present analyses therefore can be directly compared to previous estimations based on CfA data in the solar neigbourhood (Abdo et al. 2010; Ackermann et al. 2012a,e; Bolatto et al. 2013).

The ground-based data were preferred over the *Planck* CO products for the present work because of the high noise level in the *Planck* TYPE 1 CO map and because the dust optical depth was used in the component separation to extract the *Planck* TYPE 3 CO map (Planck Collaboration XIII 2014). Figure C.1 also shows a systematic photometric difference between the measurements by *Planck* and the two radio telescopes. Re-analysing the *Planck* data for CO in this specific region is beyond the scope of this paper, however.

The most sensitive (TYPE 3) *Planck* CO map shows only three tiny clumps beyond the boundary of the NANTEN survey. They lie at low latitude to the west of the Cha East II cloud in Fig. 2. Because of their small intensity, <5 K km s^{-1}, and small extent, <0.25 deg^2, and because of the photometry mismatch between the *Planck* and radio line data, they were not added to the $W_{\rm CO}$ map. Their absence does not affect the $X_{\rm CO}$ results or the CO-cloud masses presented below.

The CO line velocities span -12 to $+8$ km s^{-1} (see Fig. 3 of Mizuno et al. 2001). The cloudlet detected at $-12 < v < -4$ km s^{-1} appears to be an extension of the local complex rather than a molecular counterpart to the intermediate velocity arc. We did not attempt to separate its small contribution as an independent component. We have thus integrated the CO lines over the whole $-12 \leq v \leq +8$ km s^{-1} interval to produce the $W_{\rm CO}$ intensity map shown in Fig. 2.

We have also used the moment-masked CfA CO survey of the Galactic plane (Dame et al. 2001; Dame 2011) to complement the NANTEN data at low latitudes. We have checked that, when convolved with the LAT PSF, the contribution of the Galactic disc emission inside the analysis region is too faint to be detected as an additional component in the γ-ray analyses presented below. This is even more true for the dust analyses because of their better angular precision, so we have dropped the Galactic disc contribution from these analyses.

2.5. Individual substructures

In order to study the relative contributions of the different gas phases to the total column density, we have considered five separate substructures in the complex, away from the zone where H I lines may overlap between the local and IVA components:

– Musca at $294° \leq l \leq 309°$, $b > -11.°4$;

– Cha I at $285° \leq l < 299.°5$, $-20.°5 \leq b \leq -11.°4$;
– Cha II+III at $299.°5 \leq l < 308°$, $-23° \leq b \leq -11.°4$;
– Cha East I at $308° \leq l \leq 319°$, $-23.°5 \leq b \leq -18°$;
– Cha East II at $l \geq 300°$, $b \leq -26°$.

These limits and names, which are shown in Fig. 2, approximately follow Mizuno et al. (2001).

2.6. Ionized gas

In view of the very faint diffuse free-free emission detected at 40 GHz across this field in the nine years of observations of WMAP, we have ignored the contribution from the warm ionized gas in this study. To verify this assumption, we have taken the 9-year free-free map, based on the maximum-entropy separation and the extinction-corrected Hα map as a prior (Gold et al. 2011). We have translated the intensities into H II column densities for a gas temperature of 10^4 K and effective electron densities of 2 or 10 cm^{-3} (Sodroski et al. 1997). The resulting column densities, in the 10^{14-15} cm^{-2} range, show little spatial contrast. Such a quantitatively small and spatially smooth contribution to the total gas column density would not be detected against the other more massive and more structured gaseous components.

3. Models and analyses

3.1. Gas components on test

All the analyses use only four H I and CO maps:

– the $N_{\rm H\,I}$ map from the local Chamaeleon clouds;
– the $N_{\rm H\,I}$ map from the intermediate velocity arc;
– the $N_{\rm H\,I}$ map from the Galactic disc;
– the $W_{\rm CO}$ map from the local Chamaeleon clouds.

Faint H I emission from the LMC outskirts and its streams is present in the analysis region. This emission has not been detected in the γ-ray and dust fits presented in Sects. 3.2 and 3.3. There is no detection either of the faint CO emission from the Galactic disc background near the low latitude edge of the region. Both these components have thus been dropped from the analyses. In addition to the four H I and CO components listed above, we have constructed DNM templates from the γ-ray data and dust tracers, so that any analysis uses a total of five gaseous components.

We have performed multivariate fits to separate and study the individual contribution of each component to the γ-ray and dust data shown in Fig. 1. We have performed three studies in parallel, jointly analysing either the γ rays and A_{VQ} maps (γ+A_{VQ}), the γ rays and dust optical depth (γ+τ_{353}), or the γ rays and dust radiance (γ+R).

3.2. γ-ray model

Because of the arguments presented in Sect. 1.3 on the ISM transparency to γ rays and on the smooth penetration of cosmic rays through the different forms of gas probed by the H I and CO lines or in the intermediate DNM phase, we have modelled the γ-ray emission as a linear combination of template maps representing the different ISM components. The model also includes a contribution from the Galactic IC emission, point sources of non-interstellar origin, and an isotropic flux to account for the extragalactic γ-ray background and for any residual cosmic rays misclassified as γ rays.

The γ-ray intensity in each (l, b) direction, $I(l, b, E)$ in $\gamma\,{\rm cm^{-2}\,s^{-1}\,sr^{-1}\,MeV^{-1}}$, is modelled at each energy E as

$$I(l,b,E) = q_{\rm LIS}(E) \times \left[\sum_{i=1}^{3} q_{{\rm H\,I},i}(E)\, N_{{\rm H\,I},i}(l,b) + q_{\rm CO}(E)\, W_{\rm CO}(l,b) + q_{\rm DNM}(E)\, D^{\rm DNM}(l,b) \right] + q_{\rm IC}(E)\, I_{\rm IC}(l,b,E) + q_{\rm iso}(E)\, I_{\rm iso}(E) + \sum_j q_{S\,j}(E)\, S_j(E)\, \delta(l_j,b_j) + q_{S\,\rm ext}\, S_{\rm ext}(l,b,E), \quad (3)$$

where $N_{{\rm H\,I}\,i}$ denotes the three H I maps listed in Sect. 3.1 and $D^{\rm DNM}$ stands for the DNM map derived from the dust data. The derivation of the DNM templates is described in Sect. 3.4. The q coefficients of the model are to be determined from fits to the *Fermi* LAT data.

The $q_{{\rm H\,I},i}$, $q_{\rm IC}$, and $q_{\rm iso}$ parameters are simple normalization factors to account for possible deviations from the input spectra taken for the CR-gas interactions ($q_{\rm LIS}(E)$), for the isotropic intensity ($I_{\rm iso}(E)$), and for the IC intensity ($I_{\rm IC}(l, b, E)$). We check that there are no spectral deviations form the LIS, as they may signal a CR penetration or exclusion problem between the different gas phases or clouds.

Together with the LIS, the $q_{{\rm H\,I},i}$ parameters give estimates of the average γ-ray emissivity per nucleon in the different atomic clouds. With the further assumption of a uniform CR flux, they serve to scale the mass probed by the γ rays in the other phases.

As a reliable input for the gas emissivity spectrum, we have used the $q_{\rm LIS}$ emission rate, in photons ${\rm s^{-1}\,sr^{-1}\,MeV^{-1}}$ per nucleon, measured with five years of LAT data with the same IRFs and the same selection criteria in instrumental and Earth-limb background rejections, but with all front and back conversions in the tracker at all energies (Casandjian 2012). The LIS measurement was based on the correlation between the γ rays and the H I column densities derived from the Leiden/Argentine/Bonn (LAB) survey (Kalberla et al. 2005), for a spin temperature of 140 K, in the local Galactic ring spanning 7 to 10 kpc in Galactocentric distance. We have employed the LIS to apply the energy-dependent IRFs to model the gas emission. Large deviations from the LIS are unlikely in the nearby clouds of the Chamaeleon region (Ackermann et al. 2012a), but small variations are possible in the complex as a whole or between gas phases. The absolute intensity of the LIS also changes for different choices of H I spin temperature. This prompted us to leave the γ-ray emissivities of the different gaseous components free to renormalize in each energy band.

Sixty individual point sources have been detected inside the analysis region. Most of them are listed in the 2FGL catalogue (Nolan et al. 2012). New ones have been added from the source list in preparation within the LAT collaboration for the next catalogue. A number of "c" sources have been flagged in the 2FGL catalogue for their likely confusion with ISM clumps or with temperature artefacts in the dust map of Schlegel et al. (1998) that was part of the interstellar background model used for source detection. The "c" sources have not been confirmed as significant point sources in the present analysis, and they have been removed from the fits. We have used the spectral characteristics given in the catalogues to compute the source flux spectra, $S_j(E)$. Their individual flux normalizations, $q_{S\,j}$, have been left free in each energy band to compensate for the fact that their input spectral characteristics have been derived above a different interstellar background model. The contribution from

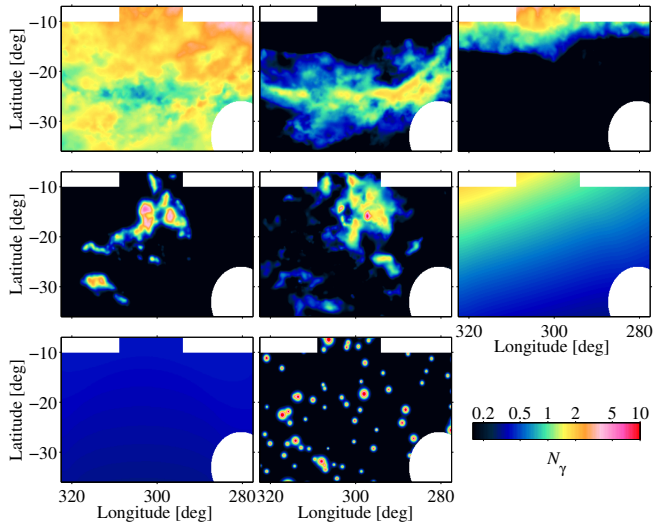

Fig. 3. Photon yields, on a 0.°125-pixel grid, from the various components of the γ-ray model in the 0.4−100 GeV band. *From left to right* and *from top to bottom*, the yields come from the $N_{\rm H\,I}$ column densities in the local, IVA, and Galactic disc clouds, the $W_{\rm CO}$ intensity in the local clouds, the $N_{\rm H_{DNM}}$ column density derived from A_{VQ}, the IC emission, the isotropic background, and point sources.

sources lying within 4° outside the analysis perimeter has been summed into a single map, $S_{\rm ext}(l, b, E)$, for each energy band, and its global normalization, $q_{S\,\rm ext}$, has been left free. Similarly, because the IC model and isotropic intensity have been studied over the whole sky and with less data, we have left their normalization free in each band.

We have modelled the $I(l, b, E)$ intensity inside the analysis region and in a 4°-wide peripheral band to account for its faint contribution inside the analysis perimeter through the wings of the LAT PSF. The modelled intensity $I(l, b, E)$ has been processed through the LAT IRFs to account for the position- and energy-dependent exposure on the sky and for the energy-dependent PSF. The resulting photon map, integrated over a specific energy band, can be directly compared to the observed data. We have used a binned maximum-likelihood with Poisson statistics to fit the model coefficients (q) to the LAT data in each of the four energy bands and in the overall one.

Figure 3 shows the photon yields obtained for the various components of the model in the overall energy band, with the DNM template provided by the A_{VQ} extinction. The photon yields from the ISM dominate the total signal. The variety of spatial distributions and the relative strengths of the interstellar components allow their effective separation despite the limited resolving power of the LAT.

3.3. Dust models

We have considered three linear models for the dust analyses, using either the $A_{VQ}(l, b)$ extinction, the $\tau_{353}(l, b)$ optical depth, or the $R(l, b)$ radiance as a tracer of the total dust column density. Mild variations in dust emissivity over spatial scales comparable to the cloud size would preserve a significant correlation between the structures observed with dust and the $N_{\rm H}$ distribution. We have therefore modelled the A_{VQ} and τ_{353} data in each direction as the linear combination of the different gaseous contributions, with free normalizations. The correlation visible in Fig. 1 between the dust radiance and either the interstellar γ rays or the other dust maps has prompted us to use the same linear model even though the radiance is more sensitive to small-scale variations in grain temperatures. We have added a free isotropic term to all models to account for the residual noise and the uncertainty in the zero level of the dust maps (Planck Collaboration XI 2014; Planck Collaboration Int. XXIX 2015)

$$D(l,b) = \sum_{1}^{3} y_{\rm H\,I,\,\it i}\, N_{\rm H\,I\,\it i}(l,b) + y_{\rm CO}\, W_{\rm CO}(l,b) + y_{\rm DNM}\, N_{\rm H\,\gamma}^{\rm DNM}(l,b) + y_{\rm iso}, \quad (4)$$

where $D(l, b)$ stands for A_{VQ}, τ_{353}, or R. The y coefficients of the model are to be determined from fits to the data. The $N_{\rm H\,\gamma}^{\rm DNM}(l, b)$ column-density map in the DNM phase has been constructed from the γ-ray data (see Sect. 3.4).

The $y_{\rm H\,I,\,\it i}$ coefficients in each analysis respectively give the average values of the $A_{VQ}/N_{\rm H}$ ratio, $\tau_{353}/N_{\rm H}$ opacity, and $R/N_{\rm H}$ ratio (thus the specific power ratio $4\pi R/N_{\rm H}$) in the different H I maps. The $y_{\rm DNM}$ and $y_{\rm CO}$ parameters can probe changes of these characteristics in the denser DNM and CO-bright phases.

Toward dense regions, fitting a single modified blackbody spectrum to the combination of SEDs produced in various ISRF conditions along the sightlines yields an overestimate of the colour temperature, thus an underestimate of τ_{353} and of the opacity (Ysard et al. 2012). This bias is gradual, but significant only beyond the high $N_{\rm H}$ range of our sample. In any case, it would enhance rather than suppress any rising trend in opacity derived from the y coefficients or in the curves and maps of Sect. 9.

The dust models have been tested against the data using a least-squares (χ^2) minimization. We expect the uncertainties in the different models to exceed those of the observed dust maps because of our assumption of uniform grain distributions through the clouds and because of the limited capability of the H I and CO data to trace the total gas (because of the data sampling, self-absorption, etc.). In the absence of a reliable estimate for the model uncertainties, we have set fractional error levels in order to obtain a reduced χ^2 value of 1 in the dust fits. This has been achieved for fractions of 16%, 18%, and 13%, respectively for the A_{VQ}, τ_{353}, and R models.

The results presented below, however, show curvature in the evolution of $A_{VQ}/N_{\rm H}$, $\tau_{353}/N_{\rm H}$, and $4\pi R/N_{\rm H}$ with increasing $N_{\rm H}$ (see Fig. 10 of Sect. 9). In this context, changing the statistical weight of the outlier data points can affect the values of the best-fit slopes of the linear model. We have therefore also performed the χ^2 fits using the smaller uncertainties of the τ_{353} and R maps. The results differ only slightly from those obtained with the model uncertainties set to achieve a unit reduced χ^2. We discuss this case in the rest of the paper as the results provide a better statistical description of the average slopes in the multivariate fits. None of our conclusions depends on this choice.

3.4. DNM templates and analysis iterations

Earlier γ-ray works cited in Sect. 1 have shown that both the dust column density and the interstellar γ-ray intensity present significant and similarly structured residuals above the linear expectations from the $N_{\rm H\,I}$ column densities and $W_{\rm CO}$ intensities. In the Chamaeleon region analysis, we have independently fitted the γ-ray intensity and the three dust maps according to Eqs. (3) and (4) with only the H I and CO maps as gaseous components. Figure D.1 shows extended regions where the data significantly exceed the best-fit models (positive residuals). These excesses

have comparable spatial distributions in all data sets. They extend to several degrees (or parsecs) around the CO clouds. As these residuals delineate gas not accounted for by the H I and CO line intensities, we can use their specific distribution, above the noise, to build a DNM template.

Since the work by Grenier et al. (2005), dust data in optical depth or reddening have been used to construct DNM templates for γ-ray analyses to complement the H I and CO data. The present analysis allows a more reliable derivation of the DNM gas contribution in three ways.

- First, by closing the loop between the γ-ray and dust fits. The DNM template estimated from the dust emission is provided to the γ-ray model; conversely, the DNM map derived from the γ-ray intensity is provided to the dust model. The residuals are obtained in each case by subtracting from the observations the best-fit contributions from the $N_{\rm H\,I}$, $W_{\rm CO}$, and ancillary (other than gas) components. Only positive residuals above the noise are kept (see below).
- Second, by iterating between the dust and γ-ray fits in order to reach a solution where the q and y model coefficients, in particular those associated with the H I and CO maps, minimally compensate for the missing DNM gas structure (see Appendix D.1). They still do at some level because the DNM templates provided by the γ rays or dust emission are not perfect.
- Third, by testing three different tracers of the total dust column density in parallel analyses.

We have not smoothed the dust maps to the γ-ray resolution in the iteration. The dust maps have a finer angular resolution than the model templates and the fit results are not sensitive to structure on angular scales below the resolution of the template maps. It is therefore possible, and important, to keep the dust resolution to model the clumpy CO component. We also note that the diffuse DNM structures independently seen in the γ-ray and dust data (in Fig. D.1) extend over large angular scales, which can be resolved by the modest γ-ray or H I resolutions.

Special attention was paid to the construction of a DNM template from the positive residuals found in γ rays and in dust. A simple cut of the residuals at zero is not acceptable as it creates an offset bias by cutting out the negative noise, but not the positive noise. For both the dust and γ-ray emission, the residual histograms showed Gaussian noise near or below zero, and a significant positive wing extending to large values. We have therefore denoised the residual maps using the multiresolution support method implemented in the `MR filter` software (Starck & Pierre 1998). We have used six scales in the B-spline-wavelet transform (à trous algorithm) and a hard 2σ threshold, using all scales for detection in dust and starting with the second scale in γ rays in order to limit the Poisson noise. We have also implemented a simple clipping method, first fitting a Gaussian to the noise-dominated part of the residual histogram, then setting the clipping threshold at the level where the histogram counts exceed the Gaussian. We have checked the consistency of the denoised and clipped maps in the regions rich in signal. We have adopted the former because the wavelet denoising is more efficient in the regions void or nearly void of signal.

Figure 1 shows that the Poisson noise in the γ-ray map is still large after five years of data acquisition. To gather the largest photon statistics, we have used all four energy bands to construct the γ-ray DNM templates by summing the residuals obtained in each band before denoising. This was preferred over the direct use of the residual map obtained in the overall-band fit because the emissivity spectra of all components are better adjusted.

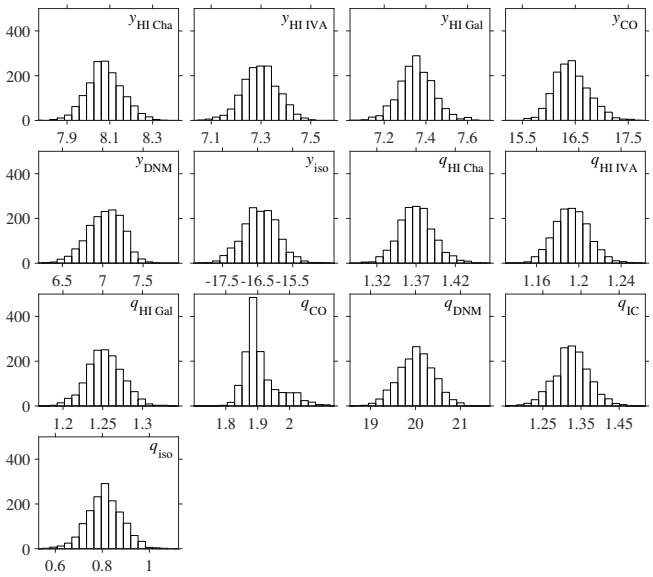

Fig. 4. Number distributions of the model coefficients obtained in the 1500 jackknife fits of the γ+A_{VQ} analysis for the optically thin H I case and overall energy band in γ rays. The $y_{{\rm H\,I},i}$ and $y_{\rm DNM}$ quantities are in units of 10^{-22} mag cm^2, $y_{\rm CO}$ in 10^{-2} mag K^{-1} km^{-1} s, $y_{\rm iso}$ in 10^{-2} mag, $q_{\rm CO}$ in 10^{20} cm^{-2} K^{-1} km^{-1} s, and $q_{\rm DNM}$ in 10^{20} cm^{-2} mag^{-1}. The $q_{{\rm H\,I},i}$, $q_{\rm IC}$, and $q_{\rm iso}$ values are simple normalization factors.

3.5. Jackknife tests

The variation of the log-likelihood ratio and χ^2 value around the best-fit parameters, namely the information matrix (e.g. Strong 1985), yields formal errors on each parameter. They include the effect of the correlation between parameters. Given the large number of pixels in the analysis, the small set of free parameters in each model, and the tight correlations present between the maps, the statistical errors on the best-fit coefficients are generally small (3–9% for the gas γ-ray emissivities, 4–13% for $q_{\rm IC}$, and 0.3–0.7% for the dust parameters).

More systematic uncertainties may arise from spatial variations of the model coefficients across the field, from the presence of deviant sub-regions (e.g. near young stellar clusters), or from spatial variations in the mean level of H I and CO self-absorption. To check the magnitude of these uncertainties, we have performed jackknife tests for the last analysis iteration. We have masked 20% of the analysis region with a random set of 2.°625-wide squares and performed the γ-ray and dust fits on the unmasked zones. The process has been repeated 1500 times for each analysis. We have found robust distributions for the best-fit coefficients, as illustrated in Fig. 4 for the γ+A_{VQ} model. All the parameters are well constrained in all analyses, with standard deviations of 2–6% for the gas γ-ray emissivities and 1–3% for the dust parameters. From a statistical point of view, the average coefficients that characterize our linear models apply to the whole region. They are not driven by a particular subset.

To construct the final statistical uncertainties on the q and y coefficients, we have added quadratically the standard deviations of the jackknife distributions and the 1σ errors inferred from the information matrices.

4. Results

The values of the best-fit q and y coefficients that have been obtained for the different γ-ray and dust fits are given in Table E.1. In this section, we discuss the results on the relative quality of the fits obtained with the different dust tracers, with and without

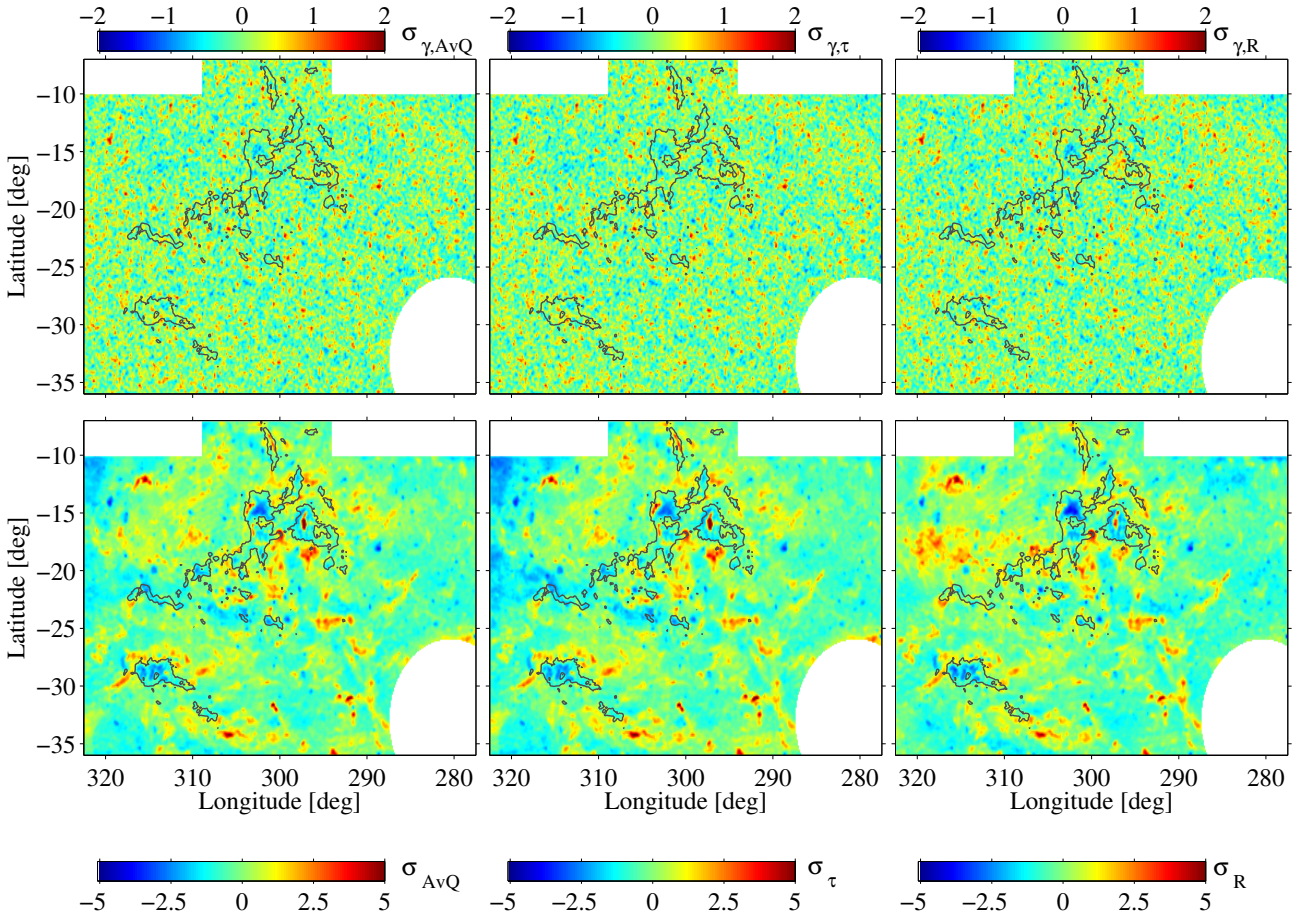

Fig. 5. *Upper row*: photon count residuals between the data and best-fit model, in sigma units on a 0.°125-pixel grid, in the 0.4−100 GeV band, with the DNM template from the dust A_{VQ} (*left*), τ_{353} (*middle*), or radiance (*right*). *Lower row*: dust residuals between the data and best-fit model, in sigma units, for the fit in A_{VQ} (*left*), τ_{353} (*middle*), and radiance (*right*). The grey contours outline the CO clouds at the 2.3 K km s^{-1} level.

the DNM component, and for different optical depth corrections in the H I.

4.1. Comparison of the dust tracers

As a first test, we have replaced the combination of H I, CO, and DNM templates in the γ-ray fits by a single dust map to trace the total gas. The quality of the fit greatly changes with the choice of dust tracer: the highest likelihood value is obtained with the $U_{\rm min}$-corrected A_{VQ} extinction, then with τ_{353}, and the poorest fit with the radiance. The values obtained for the log-likelihood ratios and the Neyman-Pearson lemma (Neyman & Pearson 1933) indicate that A_{VQ} is a better representation of the γ-ray observations than the other two dust maps with rejection probabilities $<2\times10^{-11}$. This statement remains valid for all choices of H I spin temperature. The τ_{353} and A_{VQ} quantities are both drawn from the dust emission SEDs, but the latter incorporates a $U_{\rm min}$-dependent correction to better match the dust reddening constraints. The present test against the γ rays, independent of dust, strongly confirms that the renormalization of A_{VQ} brings it in closer linear agreement with the total gas. It implies that the $U_{\rm min}$ parameter of the Draine & Li (2007) model does not only trace the ISRF, but also opacity variations.

4.2. Detection of the DNM component

We have then checked that the γ-ray fits considerably improve when adding the dust-derived DNM template to the H I and CO data. We obtain very large log-likelihood ratios between the best-fit models with and without a DNM component (respectively 1463, 1418, and 1354 for the γ+A_{VQ}, γ+τ_{353}, and γ+R analyses), so the DNM structures are detected with a formal significance greater than 36σ. Reciprocally, the γ-ray DNM template is detected at even larger confidence levels in the dust fits when we use a χ^2 minimization with the observed uncertainties, when they are available (for τ_{353} and the radiance). We cannot obtain a measure of the DNM detection when we set the dust-model uncertainties to achieve a reduced χ^2 of 1.

We then note that the combination of H I, CO, and DNM data represents the γ-ray emission better than a single dust map. The large confidence probabilities of the improvement (log-likelihood ratios of 68, 419, and 189, for A_{VQ}, τ_{353}, and R, respectively) indicate the presence of significant differences in the average dust properties in each gas phase.

4.3. H I optical depth correction

The γ rays can help constrain the *average* level of H I optical-depth correction by comparing the $T_{\rm S}$-dependent contrast of the $N_{\rm H\,I}$ maps with the structure of the γ-ray flux emerging from the H I gas. It has been shown in the case of the Cepheus and Cygnus clouds that the mean spin temperature so inferred agrees with the more precise, but sparse, measurements obtained from paired absorption/emission H I spectra (Abdo et al. 2010; Ackermann et al. 2012b). We have found no such pairs toward the Chamaeleon region in the literature

(e.g. Heiles & Troland 2003; Mohan et al. 2004), but the results of the three analyses indicate that the γ-ray fits significantly improve with decreasing H I opacity correction, for all energy bands. Figure B.1 indicates that a uniform temperature $T_S >$ 340 K, >300 K, and > 640 K is preferred at the 95% confidence level in the γ+A_{VQ}, γ+τ_{353}, and γ+R analyses, respectively. The results indicate that optically thin conditions largely prevail in the local and IVA H I clouds, in agreement with the low mean brightness temperature of 4.1 K in the sample and with the large fraction of lines that peak below 100 K in brightness temperature (98.9%).

As the (uniform) spin temperature is decreased, the correction to $N_{\rm H\,I}$ increases, the γ-ray emissivity of the H I clouds decreases and the opacity and specific power of their dust grains decreases. The H I-related coefficients of the γ-ray and dust models increase by 10−15% as the spin temperature rises from 125 K to optically thin conditions. H I optical depth corrections have therefore a small effect on the derivation of $X_{\rm CO}$ factors and dust properties per gas nucleon in this region.

In view of these results and with the added arguments that we detect no change of the CR spectrum in the present H I structures (see Sect. 5), nor in the larger, less transparent column densities probed in other clouds (Ackermann et al. 2012b), we consider the optically thin H I case as that which best represents the Chamaeleon region data. Unless otherwise mentioned, all plots and results hereafter have been generated for this case.

Nonetheless, we find it useful to quote both types of uncertainties for our results: the statistical errors described above, and those related to the uncertain optical depth of the H I lines. For the latter, we have taken the range of q and y coefficients obtained for the fits with T_S larger than the 95% confidence limits quoted above. These ranges provide lower limits to the systematic uncertainties, since we can only explore models with uniform spin temperature, not properly representative of the variety of opacities present in the CNM (Heiles & Troland 2003). We use the notation, $x = x_0 \pm \sigma_x\ ^{+\Delta x}_{-\Delta x'}$, to give both types of uncertainties.

4.4. Residual maps

The residual maps of Fig. 5 indicate that the linear models provide excellent fits to the γ-ray data in the overall energy band. They do so in the four separate energy bands as well. The residuals are fully consistent with noise at all angular scales except, marginally, toward the brightest CO peaks of Cha I and Cha II when the DNM template comes from the dust radiance. Whereas the dust-derived DNM templates provide adequate structure and column density in addition to the H I and CO contributions to fully account for the γ-ray observations, Fig. 5 shows that significant residuals remain in all dust tracers. The positive residuals follow the bulk distribution of the DNM and they are partly due to the limitations in angular resolution and sensitivity of the γ-ray DNM template compared to its dust homologue. Clumps in the residual structure can also reflect localized variations in dust properties per gas nucleon that are not accounted for in the linear models. This is the case toward the dense CO clouds where the dust models often exceed the data because of a rapid increase in dust emissivity and decrease in specific power as $N_{\rm H}$ increases. These effects are discussed in Sect. 9. The asymmetry of the residuals between the cores of Cham I and II in all dust and γ-ray fits requires further investigations with less optically-thick CO tracers such as ^{13}CO.

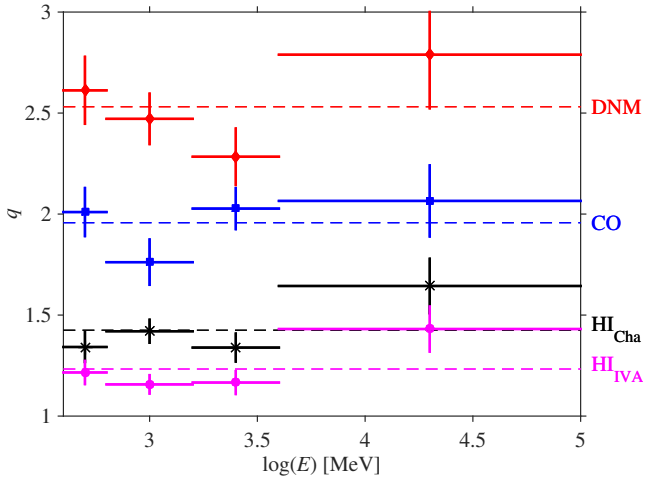

Fig. 6. Spectral variation, relative to the local interstellar spectrum $q_{\rm LIS}$, of the γ-ray emissivities obtained for the local gas components in the γ+A_{VQ} analysis. The $q_{\rm CO}$ value is given in units of 10^{20} cm^{-2} K^{-1} km^{-1} s, $q_{\rm DNM}$ in 8×10^{20} cm^{-2} mag^{-1}, and the H I emissivities refer to the optically thin H I case. The dotted lines mark the mean emissivities.

5. Cosmic-ray content of the clouds

We have used wide γ-ray energy bands to increase the photon statistics to better separate the spatial patterns of the different emission components. Nevertheless, Fig. 6 indicates that the q normalizations relative to the local CR emissivity spectrum ($q_{\rm LIS}$) do not significantly change with energy. Figure 6 illustrates this point for the γ+A_{VQ} analysis, and we find the same trends for the γ+τ_{353} and γ+R ones. The spectra of the emission originating from the different gas phases and in the different clouds are therefore all consistent with the shape of the input $q_{\rm LIS}$ spectrum. At the precision level of the current data, we find no spectral evidence for concentration or exclusion of CRs with increasing gas volume density, up to the 10^{3-4} cm^{-3} densities sampled by CO observations.

The input $q_{\rm LIS}$ emissivity spectrum is the average found over the large masses of atomic gas lying in the Galaxy within 1.5 kpc about the solar circle. Its normalization in terms of emission rate per nucleon corresponds to a low H I spin temperature of 140 K (Casandjian 2012). The Chamaeleon complex results are given for the optically thin case preferred by the fits. We therefore expect the relative q normalizations in Table E.1 to exceed unity for the same CR flux as in the LIS. To ease the comparison, we have calculated the present γ-ray emissivities for the same spin temperature of 140 K. The results indicate that the CR flux in the atomic gas of the Chamaeleon complex and of the IVA clouds is respectively (22 ± 5)% and (8 ± 4)% higher than the solar-circle average. The concordance is remarkable given the large differences in size, mass, and linear resolution between these small clouds and the broad Galactic ring. The emissivities in the Chamaeleon clouds and in the less massive and velocity-sheared IVA also compare well, within 20% at all energies. It will be important to determine the distance of the IVA in order to investigate whether the 20% difference is due to the unusual dynamical state of the cloud or to a larger altitude above the Galactic disc. Both cases would bring important constraints on CR diffusion.

In order to compare with previous measurements in the solar neighbourhood (Ackermann et al. 2013, 2012e), we have calculated the integral emissivity of the H I gas between 400 MeV

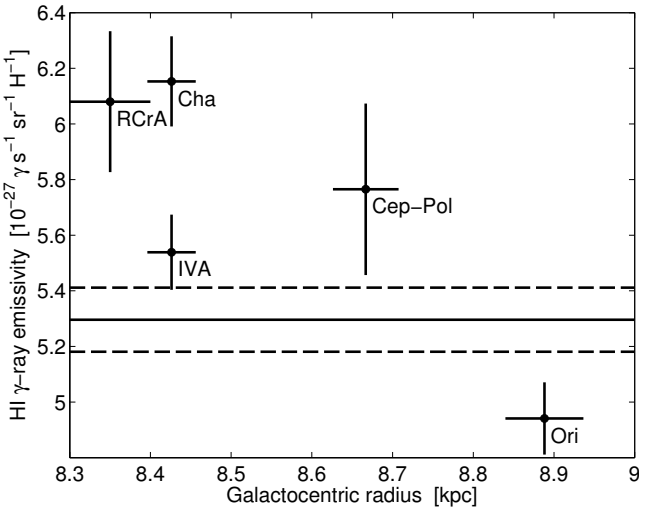

Fig. 7. Distribution, with Galactocentric radius, of the 0.4−10 GeV emissivities measured in the atomic gas of nearby clouds, for an H I spin temperature of 125 K. The $\pm1\sigma$ error bars are purely statistical. The solid line marks the mean emissivity measured within 1.5 kpc about the solar circle, for an H I spin temperature of 140 K. The dashed lines give the $\pm1\sigma$ error.

and 10 GeV, for a spin temperature of 125 K. The values are shown in Fig. 7 together with the average emissivity at the solar circle, integrated over the same energy band, but for a spin temperature of 140 K. To calculate the Galactocentric positions of the clouds, we have taken distance ranges of 250−400 pc for the Cepheus-Polaris complex (Schlafly et al. 2014), of 390−500 pc for the Orion clouds (Ackermann et al. 2012e; Schlafly et al. 2014), and of 100−200 pc for the R CrA, Chamaeleon, and IVA clouds (Mizuno et al. 2001; Corradi et al. 2004; Ackermann et al. 2012a). We separate the clouds in Galactocentric radius, but do not expect a CR gradient over such a small distance range. The data points indicate that an equivalent CR flux pervades the nearby Chamaeleon, R CrA, Cepheus, and Polaris clouds. We note that the low CR flux anomaly reported earlier for the Chamaeleon complex was due to an error in evaluating the exposure (Ackermann et al. 2012a, 2013). The emissivity in Orion may be ∼25% lower than in the other nearby complexes of the Chamaeleon, R CrA, Cepheus, and Polaris. This difference is small and commensurate with systematic uncertainties in component separations, so a careful re-analysis of the region with three times more γ-ray data (now available), higher H I resolution, and iterative construction of the DNM map is required to assess this difference.

The uniformity of the CR spectrum across the different gas phases gives weight to the total-gas tracing capability of the γ-ray map. Various mechanisms can alter the CR flux inside dense clouds, but most are inefficient for particle energies in the GeV-TeV range corresponding to the LAT observations. The particles can diffuse efficiently on magnetic irregularities with wavelengths commensurate with their gyroradii ($\ll$1 mpc), but the required power to maintain the Alfvén waves against ion friction with the predominant gas neutrals inside dense clouds (Cesarsky & Volk 1978) would be too large. Particle depletion inside a dense core may also happen because of increased γ-ray losses in dense gas. It leads to a net CR streaming flux inward, which in turn generates Alfven waves on the outskirts of the core, on the flux tubes connected to the surrounding medium. These waves impede particle progression into the core (Skilling & Strong 1976). The exclusion is strongly energy dependent and only efficient at particle energies below 0.1 GeV if one ignores the magnetic field compression inside the dense cloud or 1 GeV if one includes it (Skilling & Strong 1976; Cesarsky & Volk 1978). In the Chamaeleon region, with a CR flux inferred to be near the local ISM average and with maximum $N_{\rm H_2}$ column densities around 2×10^{22} cm^{-2}, exclusion is predicted to be negligible (<2%) for the particles that produce γ rays in the LAT band (Skilling & Strong 1976). Random magnetic mirrors in the clouds have also been investigated, but they affect only CR particles at low energies, invisible to the LAT (Cesarsky & Volk 1978; Padovani & Galli 2011). Only CR trapping in the magnetic bottles created between dense cores might affect the emerging γ-ray intensity if the trapped particles die owing to radiative then ionization losses before escaping the bottles or before being replenished by residual diffusion. The prediction of a 3- to 5-fold increase in contrast in γ-ray intensity, compared to that in gas density (Cesarsky & Volk 1978), would strongly bias the $X_{\rm CO}$ factor upward. However, more detailed numerical simulations indicate that TeV particles effectively scatter off magnetic turbulence and smoothly diffuse throughout the complex uniform and turbulent field of a molecular cloud (Fatuzzo et al. 2010). All these concentration and exclusion processes would leave an energy-dependent signature that we do not detect.

6. Gas column-densities in the dark neutral medium

The $q_{\rm DNM}$ coefficients of the γ-ray model (Eq. (3)) provide spectral information on the radiation produced in the DNM. The lack of energy dependence of these coefficients (see Fig. 6) indicates that the spectrum of the DNM-related γ-ray emission closely follows that produced by CR interactions with gas in the local ISM in general, and with the atomic and molecular gas of the Chamaeleon complex in particular. The fact that the γ-ray-derived and dust-derived DNM templates jointly yield reasonable values for the dust properties per gas nucleon in the DNM provide further evidence that both the dust and γ rays reveal large quantities of gas missed with the H I and CO data.

We have converted the γ-ray and dust DNM templates into gas column densities, $N_{\rm H_{DNM}}$, under the assumption that the same CR flux permeates the diffuse H I and DNM phases. The spectral uniformity of the γ rays borne in the two phases supports this assumption (see Fig. 6). To derive the $N_{\rm H_{DNM}}$ maps, we have used the templates built from the γ-ray and dust fits in the three analyses. The conversion of the γ-ray templates uses the emission rate per nucleon measured in the atomic gas of the Chamaeleon complex, $q_{\rm HI\,Cha}(E)\times q_{\rm LIS}(E)$. The conversion of the dust templates uses the average $\overline{A_{VQ}/N_{\rm H}}^{\rm DNM}$, $\overline{\tau_{353}/N_{\rm H}}^{\rm DNM}$, and $4\pi\overline{R/N_{\rm H}}^{\rm DNM}$ ratios measured in γ rays as $(\overline{D/N_{\rm H}})^{\rm DNM} = q_{\rm HI\,Cha}/q_{\rm DNM}$ (see Sect. 8). We have applied the weighted means of the ratios obtained in the four γ-ray energy bands to produce the maps shown in Fig. 8.

The faintest signals shown in the plots are 2σ above the noise. We have noted in Sect. 4 how strongly the quality of the different fits responds to the inclusion of the DNM maps in all the models. Figure 8 also indicates that they share remarkably similar spatial distributions in the different analyses. The $N_{\rm H_{DNM}}$ values obtained with the different tracers are remarkably close, considering the lower contrast due to the relatively broad LAT PSF. The layout of the DNM phase is intimately connected to the overall structure of the complex, and exhibits column densities similar to those in H I. These moderate densities give further grounds to the assumption of a uniform CR flux through the H I and DNM phases, since the diffusion and loss mechanisms discussed in the previous section set in at much larger densities in the compact molecular cores. The most sensitive CO map from

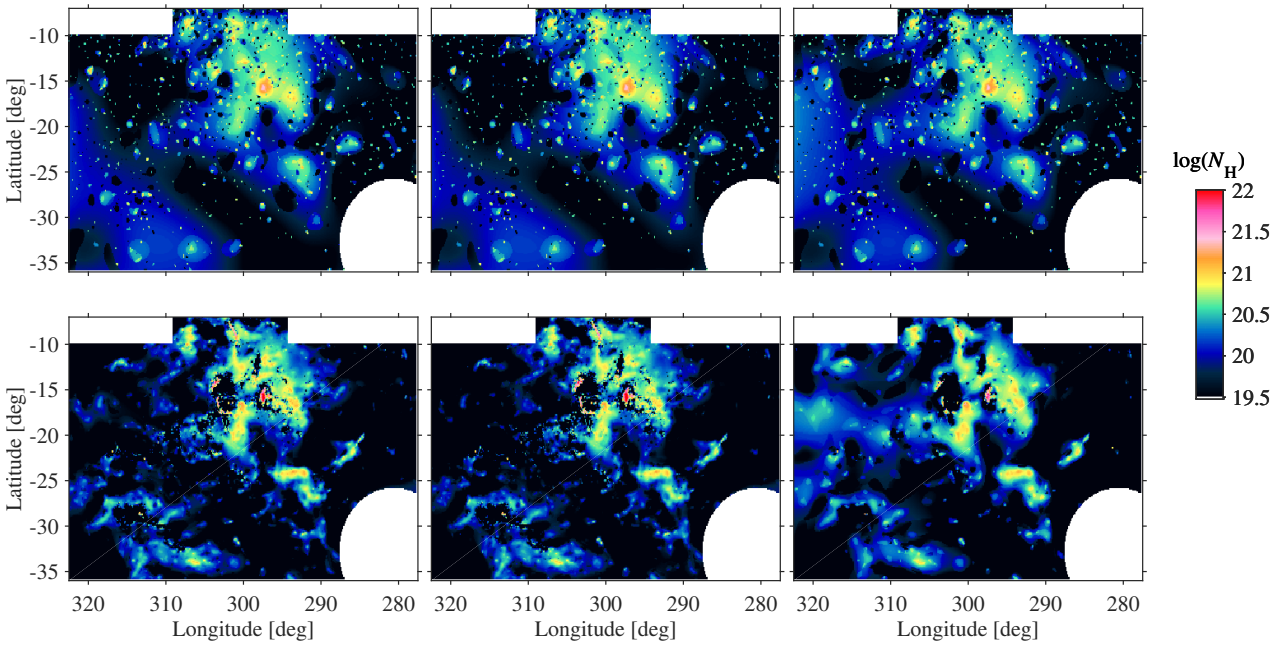

Fig. 8. Gas column-density maps in the DNM (in cm^{-2}) obtained from the γ-ray (*upper row*) and the dust (*lower row*) data after subtraction of the best-fit N_{HI} and W_{CO} contributions and other components unrelated to gas. The dust tracers are respectively A_{VQ}, τ_{353}, and R *from left to right*.

Planck (TYPE 3, Planck Collaboration XIII 2014) confirms that the extended DNM clouds cannot be explained by overlooked CO beyond the faint edges mapped with NANTEN down to about 1 K km s^{-1}.

High $N_{H_{DNM}}$ peaks reaching 10^{22} cm^{-2} are found that partially overlap bright CO cores. Their detection in γ rays and with three dust tracers confirms their reality, which plausibly relates to the saturation of the W_{CO} intensities because of the large optical thickness of the dense molecular gas to ^{12}CO ($J = 1 \rightarrow 0$) line emission. We have checked that the factor of 2 difference between the peak values measured in γ rays and with the dust radiance is due to the reduced angular resolution of the LAT. The additional three-fold increase to the peak column densities measured with τ_{353} relates to the dust evolution discussed in Sect. 9, so values beyond 5×10^{21} cm^{-2} should be considered with care. The high $N_{H_{DNM}}$ peaks are surrounded by regions devoid of DNM, where the W_{CO} structure traces the γ-ray and dust distributions fairly well. We need more γ-ray statistics at high energy to further test these peaks at the best LAT angular resolution against ^{12}CO and ^{13}CO line emissions. The $N_{H_{DNM}}$ values below about 2×10^{20} cm^{-2} near $l = 319°$, $b = -18°$ and $l = 318°$, $b = -11.°5$, should also be taken with care as they depend on the choice of dust tracer in a region of warm grains.

7. The X_{CO} factor

The fits in the separate γ-ray energy bands provide independent measures of the X_{CO} conversion factor relating the W_{CO} intensity and N_{H_2} column density. Assuming the same CR flux in the H I and CO-bright phases, the factor is given by $X_{CO\gamma} = q_{CO}/(2q_{HI\,Cha})$. We can take advantage of the energy-dependent variation of the LAT resolving power (FWHM of the PSF) to probe X_{CO} at different linear scales in the clouds (here we assume a distance of 150 pc). We have computed the effective PSF widths for the q_{LIS} spectrum and for the energy-dependent exposure of the LAT in this region. Figure 9 shows no modification of the X_{CO} factors at parsec scales in the clouds in the case of the γ+A_{VQ} analysis. We find the same lack of any trend in the other two analyses. Table 1 lists the weighted averages of the values obtained in the four energy bands. They closely match the result obtained in the overall energy band, which combines photons obtained with different angular resolutions into a single map, but which has more robust photon statistics. The $X_{CO\gamma}$ results for the three analyses are consistent within the band-to-band dispersion.

Table 1. X_{CO} conversion factors obtained from the γ-ray and dust fits in the separate analyses.

X_{CO}[a]	γ-ray fits[b]	Dust fits
γ+A_{VQ}	$0.69 \pm 0.02^{+0.03}_{-0}$	$1.01 \pm 0.02^{+0.05}_{-0}$
γ+τ_{353}	$0.65 \pm 0.02^{+0.04}_{-0}$	$1.27 \pm 0.03^{+0.07}_{-0}$
γ+R	$0.79 \pm 0.02^{+0.02}_{-0}$	$0.66 \pm 0.02^{+0.02}_{-0}$

Notes. [(a)] In units of 10^{20} cm^{-2} K^{-1} km^{-1} s. [(b)] The γ-ray values are the weighted averages of the results obtained in the four energy bands.

These findings agree with the theoretical prediction that CR exclusion be negligible in the less massive Chamaeleon clouds, with a loss of less than a few per cent from slower convection into the CO clouds (Skilling & Strong 1976). Conversely, CR concentration inside the CO phase, or magnetic trapping between the dense cloudlets that populate the CO clouds, would bias $X_{CO\gamma}$ upward, but the effect is expected to be small because high-energy CRs effectively scatter off magnetic turbulence (Fatuzzo et al. 2010). We find no evidence for such trapping at the smallest linear scales probed by the LAT.

The $X_{CO\gamma}$ results compare well with other γ-ray measurements in nearby clouds, which range from $(0.63 \pm 0.02\,^{+0.09}_{-0.07}) \times 10^{20}$ cm^{-2} K^{-1} km^{-1} s in Cepheus-Polaris to $(0.99 \pm 0.08\,^{+0.18}_{-0.10}) \times 10^{20}$ cm^{-2} K^{-1} km^{-1} s in R CrA (Ackermann et al. 2012a; Abdo et al. 2010). A slightly higher factor, close to $(1.07 \pm 0.02) \times 10^{20}$ cm^{-2} K^{-1} km^{-1} s, has been measured to higher W_{CO} intensities, with no departure from linearity, in the more massive Orion clouds (Ackermann et al. 2012e).

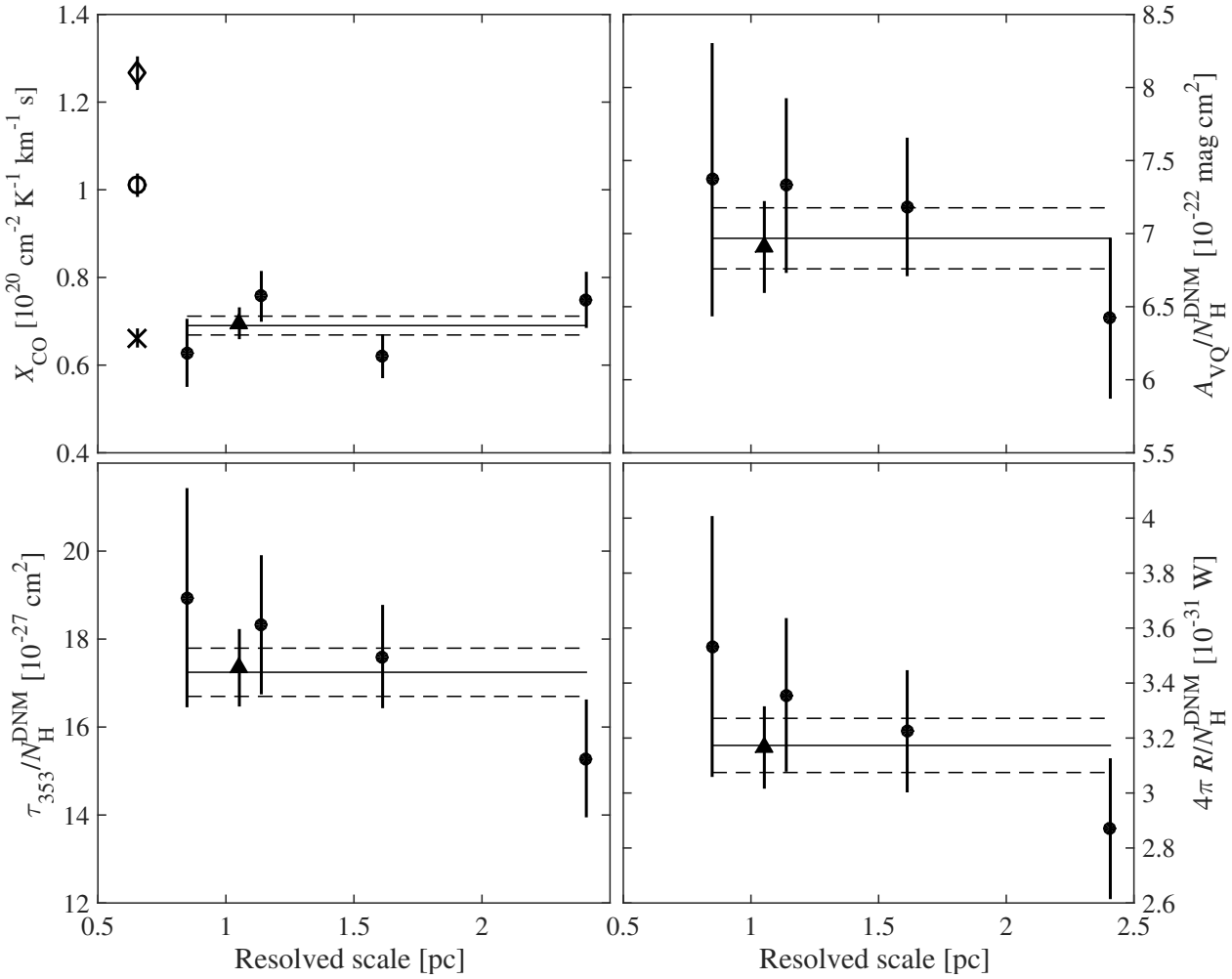

Fig. 9. Evolution of the X_{CO} factors and of the average dust properties per gas nucleon in the DNM, as measured in γ rays for different linear resolutions in the clouds. The black triangles mark the γ-ray measurements in the overall energy band, in close agreement with the weighted average of the other four independent estimates (thin lines) and their $\pm 1\,\sigma$ errors (dashed lines). The X_{CO} factors obtained from the dust fits are shown as open symbols (circle for A_{VQ}, diamond for τ_{353}, and cross for R).

The factors found in this work are moderately smaller than the previous estimate of $(0.96 \pm 0.06_{\rm stat}\,^{+0.15}_{-0.12^{\rm sys}}) \times 10^{20}$ cm^{-2} K^{-1} Km^{-1} s obtained in the Chamaeleon clouds (Ackermann et al. 2012a). The difference stems from the improved component separation performed here, in particular to extract the local $q_{\rm H\,I}$ emissivity that enters the X_{CO} calculation: higher angular resolution of the H I data to reduce the cross talk with other components; separation of the local H I gas from the contributions in the IVA and Galactic disc; better separation of the diffuse H I and IC components across a wider region in latitude. The difference also stems from the use of optically thin H I data to improve the γ-ray fit. For a spin temperature of 125 K, as in previous works, we obtain a larger X_{CO} factor of $(0.79 \pm 0.03) \times 10^{20}$ cm^{-2} K^{-1} km^{-1} s.

The X_{CO} factors obtained so far in γ rays in nearby clouds are consistent with a value of 0.9×10^{20} cm^{-2} K^{-1} km^{-1} s and rms dispersion of 0.3×10^{20} cm^{-2} K^{-1} km^{-1} s. The latter is mostly driven by uncertainties in H I spin temperature and in component separation between gas phases. These uncertainties prevent any claim of cloud-to-cloud variations in X_{CO} until all clouds are modelled with the same set of approximations and same set of linear resolutions.

Similarly hypothesizing a uniform dust-to-gas mass ratio and uniform emission coefficient κ_{353} for the grains, one can infer X_{CO} from the dust fits as $X_{CO} = y_{CO}/(2y_{\rm HI\,Cha})$. The $X_{\rm COAvQ}$ and $X_{\rm CO\tau}$ values inferred from the dust extinction and optical depth are found to be at variance with those obtained with the dust radiance and with the γ-ray estimates (Fig. 9). The latter estimates, on the contrary, are consistent around 0.7×10^{20} cm^{-2} K^{-1} km^{-1} s. Variations in the dust-to-gas mass ratio, or the per cent level of contamination of the dust SED by CO line emission leaking into the *Planck* filters, would affect all dust estimates similarly. The 40% (80%) discrepancy between $X_{\rm COAvQ}$ ($X_{\rm CO\tau}$) and the other values thus has another cause. It can stem from dust evolution, where dust properties change with environment, and which has been invoked to explain a roughly 3-fold increase in dust emissivity in molecular regions (Stepnik et al. 2003; Martin et al. 2012; Roy et al. 2013; Planck Collaboration Int. XVII 2014). The evidence we present in Sect. 9 of a marked increase in $A_{VQ}/N_{\rm H}$ and $\tau_{353}/N_{\rm H}$ in the molecular environment indeed biases the dust derivation of X_{CO} upward.

Variations in dust emissivity or opacity in the CO phase can explain why the X_{CO} factors derived in previous studies, from the intensity of the thermal dust emission or from its colour-corrected optical depth, were systematically higher than the γ-ray estimates, typically by a factor of more than 2 (e.g. Dame et al. 2001; Planck Collaboration XIX 2011; Grenier et al. 2005). Finding the cause of the discrepancy was hampered by the use of different H I and CO calibrations, different

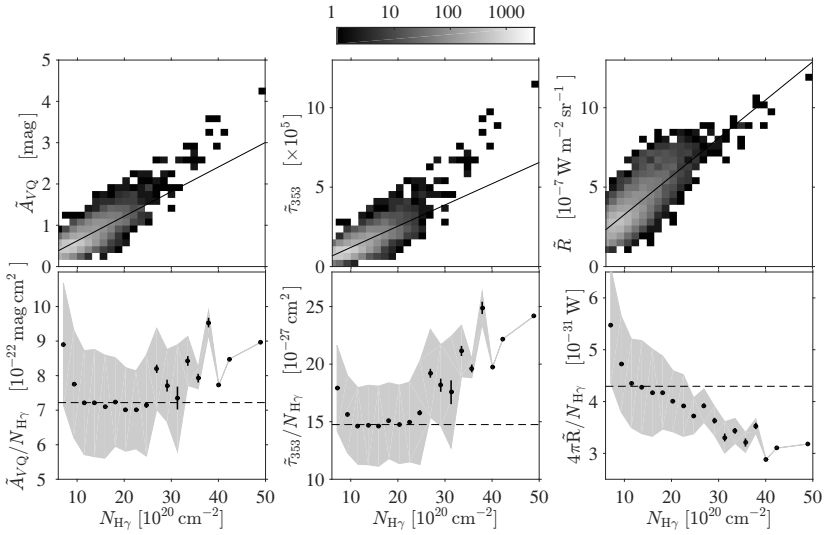

Fig. 10. *Upper row*: 2D histograms of the correlations between the total gas column density, $N_{H\gamma}$, measured by the $10^{2.6-5}$ MeV interstellar γ rays, and the dust tracers convolved with the LAT response for an interstellar spectrum. The maps were sampled on a 0.°375 pixel grid. The solid lines mark the best linear regressions through the data points of the maps. *Lower row*: evolution of the dust properties per gas nucleon in bins of $N_{H\gamma}$. The error bars and shaded areas respectively give the standard error of the means and the standard deviations in each bin. The dashed lines give the mean ratios at low N_H, in the $(1-2.2)\times10^{21}$ cm^{-2} interval.

correlation methods, and different angular resolutions. These limitations have been alleviated here. The results provide new insight into this recurrent problem by establishing, through the convergence between $X_{CO\gamma}$ and X_{COR}, that the difference does not stem from a γ-ray versus dust-tracing problem, but rather from dust evolution that must be compensated for to trace the total dust column.

Bolatto et al. (2013) commented that the lower Xco values obtained from γ-ray analyses relative to dust ones is due to a difference in X_{CO} definition, namely that the CO-faint H_2 envelope of molecular clouds is included in the dust derivation and not in the γ-ray one because of the use of a DNM template. This is not the case here since both dust and γ-ray analyses include a DNM component, but this reason cannot be invoked in general because, by construction, the DNM component contains mass with column densities that do not correlate with the W_{CO} intensity. Its inclusion (or not) in the analysis does not remove (or add) gas that scales with W_{CO}. Thus to first order, its inclusion does not have an impact on the linear scaling factor $\frac{N_{H_2}}{W_{CO}}$ that defines X_{CO}. In the component separation of the total gas, the CO-related component gathers the whole gas column density that *correlates* with W_{CO}, independently of its chemical form and of its location inside the CO-bright clumps or in their peripheral CO-faint envelopes. Grenier et al. (2005) have verified the stability of X_{CO} with respect to the addition of a DNM component, for three different dust DNM templates, and taking advantage of extensive CO maps across the sky to alleviate the impact of the residual cross-talk between the different gas components. They found that X_{CO} increased (instead of decreased) by only 2–4% when adding a DNM component. With the higher resolution of the present study, we further show in Appendix D that X_{CO} as well as the dust and γ-ray emissivities in the H I are biased upward when omitting the DNM structure from the model; they artificially increase to partially compensate for the missing gas, but the best-fit model then largely over-predicts the data toward the CO cores, thereby signalling that the X_{CO} ratio is too large.

The convergence between $X_{CO\gamma}$ and X_{COR} opens the way to additional studies in nearby clouds to quantify the amplitude of cloud-to-cloud variations in X_{CO} and to investigate why the dust-derived factors in the Chamaeleon clouds are significantly lower than previous estimates based on the same type of data, for instance $(1.8\pm0.3)\times10^{20}$ cm^{-2} K^{-1} km^{-1} s at $|b| > 5°$ from the 100 μm intensity data (Dame et al. 2001), and $(2.54\pm0.13)\times10^{20}$ cm^{-2} K^{-1} km^{-1} s at $|b| \geq 10°$ from the 0.1–3 mm optical depth (Planck Collaboration XIX 2011). We defer the derivation of X_{CO} from dust reddening to subsequent work. We note, however, that X_{COR}, which is less biased by dust evolution in the CO clouds, is less than half the values measured elsewhere with reddening measurements (e.g. an average of $(1.67\pm0.08)\times10^{20}$ cm^{-2} K^{-1} km^{-1} s at $|b| > 10°$ and near 2.1×10^{20} cm^{-2} K^{-1} km^{-1} s in the Taurus cloud, Pineda et al. 2010; Paradis et al. 2012) using the Two Micron All Sky Survey (Skrutskie et al. 2006, 2MASS). As discussed above, detailed comparisons based on the same methods, gas tracers, and resolutions are required to investigate the origin of these differences.

We also note a systematic difference, by a factor greater than two, between the X_{CO} factors measured in γ rays at parsec scales in well resolved nearby clouds and the averages closer to 2×10^{20} cm^{-2} K^{-1} km^{-1} s obtained on a kiloparsec scale in spiral arms (Abdo et al. 2010; Ackermann et al. 2011b; Bolatto et al. 2013). X_{CO} may vary with metallicity and UV-flux gradients across the Galaxy, but the discrepancy is already present within 1–1.5 kpc in the local spiral arm (Abdo et al. 2010; Ackermann et al. 2011b, 2012b), while *Herschel* observations of nearby galaxies indicate rather uniform X_{CO} values to large radii past the central kiloparsec (Sandstrom et al. 2013). Other observational and physical explanations for this discrepancy include the following.

- Given the overwhelming mass locked up in the atomic phase, a small error in the H I-CO phase separation can have a large impact on X_{CO}. Wrongly attributing 10–20% of the clumpy CNM to the CO structure, because of inadequate resolution and thus an increased level of cross-talk at large distances, would be sufficient. The study of nearby galaxies shows that X_{CO} tends to increase when measured in confused environments. Systematically larger X_{CO} values are found in highly inclined galaxies than in face-on galaxies with less pile-up along the lines of sight (Sandstrom et al. 2013).
- Separation of the DNM and CO phases when seen at large distance is even more problematic because of the DNM disposition around the CO and because of a more difficult DNM prediction from dust residuals along long sightlines. C^+ observations further suggest a systematic rise in the CO-dark to CO-bright H_2 abundance with increasing radius in the Galaxy (Pineda et al. 2013; Langer et al. 2014). The larger DNM abundance and increasing difficulty in the

Table 2. A_{VQ}/N_{H} ratios, opacities, and specific powers of the dust averaged over the different gas phases or clouds.

Component	$\overline{A_{VQ}/N_{H}}$ [10^{-22} mag cm^2]	$\overline{\tau_{353}/N_{H}}$ [10^{-27} cm^2]	$4\pi\overline{R/N_{H}}$ [10^{-31} W]
H I Galactic disc	$7.41 \pm 0.09^{+0}_{-0.22}$	$12.4 \pm 0.2^{+0}_{-0.5}$	$6.08 \pm 0.06^{+0}_{-0.08}$
H I IVA	$7.31 \pm 0.07^{+0}_{-0.26}$	$14.8 \pm 0.2^{+0}_{-0.6}$	$4.59 \pm 0.05^{+0}_{-0.09}$
H I Cha	$8.11 \pm 0.09^{+0}_{-0.37}$	$16.3 \pm 0.2^{+0}_{-0.8}$	$4.85 \pm 0.06^{+0}_{-0.13}$
DNM	$7.0 \pm 0.2^{+0}_{-0.3}$	$17.2 \pm 0.5^{+0}_{-1.0}$	$3.17 \pm 0.10^{+0}_{-0.07}$
CO[a]	$11.9 \pm 0.4^{+0}_{-0.5}$	$32 \pm 1^{+0}_{-2}$	$4.06 \pm 0.16^{+0}_{-0.09}$

Notes. [(a)] The values for the CO phase assume the corresponding $X_{CO\gamma}$ factor derived in γ rays.

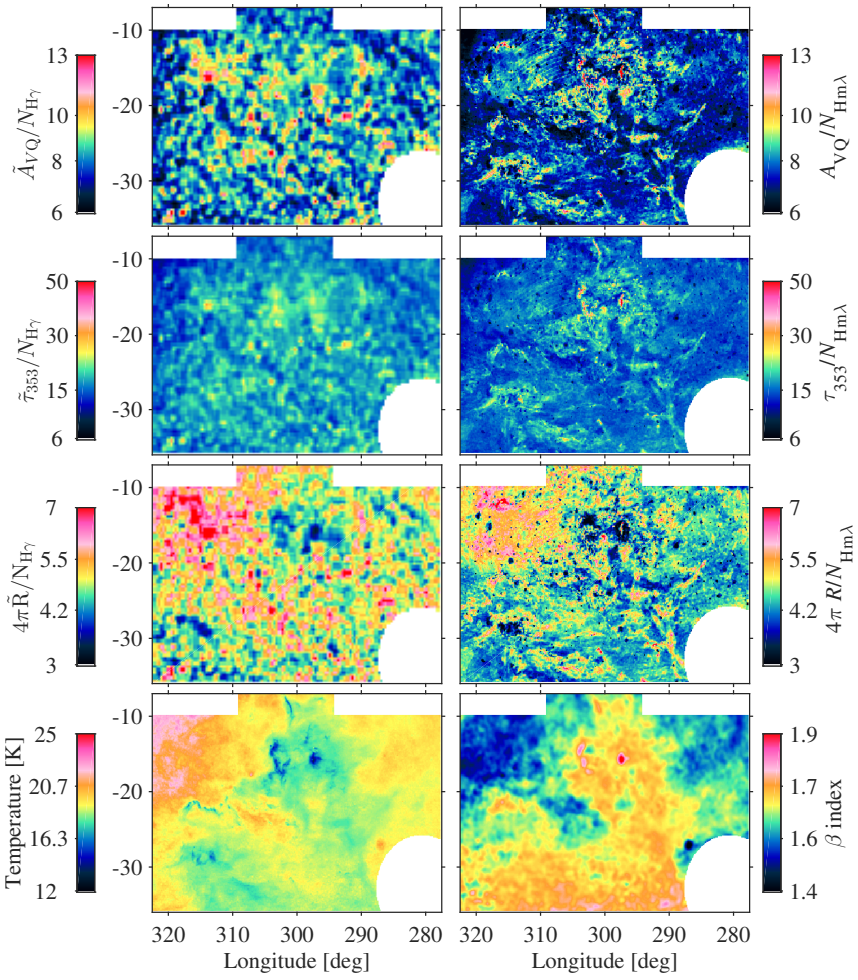

Fig. 11. *Three upper rows*: spatial variations of the dust properties per gas nucleon with the total gas measured by $N_{H\gamma}$ on a 0.°375 pixel grid (*left*) and by $N_{Hm\lambda}$ on a 0.°125 pixel grid (*right*). *Lower row*: colour temperature and β index of the dust SED, measured at 5' resolution by Planck Collaboration XI (2014) and displayed on a 0.°125 pixel grid. The A_{VQ}/N_{H} values are in units of 10^{-22} mag cm^2, τ_{353}/N_{H} in 10^{-27} cm^2, and $4\pi R/N_{H}$ in 10^{-31} W.

DNM-CO separation conspire to bias the X_{CO} factor upward in the outer Galaxy.

– X_{CO} is expected to increase from the dense, cold molecular cores to the more diffuse, warmer molecular envelopes where CO is more exposed to photo-dissociation and the lines are weakly excited (Bolatto et al. 2013). Sampling a larger fraction of envelopes in well resolved clouds should therefore bias X_{CO} upward, contrary to the observations. On the other hand, the CO abundance relative to H_2 gradually changes from a square root dependence ($N_{CO}/N_{H_2} \propto N_{H_2}^{0.5\pm0.2}$) to a quadratic one ($\propto N_{H_2}^{2.1\pm0.7}$) with a transition around N_{H_2} $\sim 2.5\times10^{20}$ cm^{-2} (Sheffer et al. 2008), so local changes in the balance between chemistry and photo-dissociation can cause large variations in X_{CO}. It was suggested, however, that the variations average out in the mix of situations along the lines of sight (Liszt et al. 2010; Liszt & Pety 2012).

More tests are needed to disentangle the origin of the discrepancy. With larger photon statistics at high energy in γ rays, we will soon be able to investigate how the angular resolution and cross-talk between gas phases affect the X_{CO} calibration beyond the solar neighbourhood.

8. Mean dust properties in each phase

Our analyses yield average dust properties per gas nucleon in each phase. The best-fit y_{HI} coefficients, respectively, give

Table 3. Average $N_{\rm H}/E(B-V)$ ratios measured in the different gas phases or clouds.

Component	$\left(\overline{\frac{N_{\rm H}}{E(B-V)}}\right)_{A_{VQ}}$ [10^{21} cm^{-2}]	$\left(\overline{\frac{N_{\rm H}}{E(B-V)}}\right)_{\tau}$ [10^{21} cm^{-2}]	$\left(\overline{\frac{N_{\rm H}}{E(B-V)}}\right)_{R}$ [10^{21} cm^{-2}]
H I Galactic disc	$4.19 \pm 0.05^{+0.13}_{-0}$	$5.4 \pm 0.1^{+0.2}_{-0}$	$3.83 \pm 0.07^{+0.05}_{-0}$
H I IVA	$4.24 \pm 0.04^{+0.16}_{-0}$	$4.5 \pm 0.1^{+0.2}_{-0}$	$5.07 \pm 0.10^{+0.10}_{-0}$
H I Cha	$3.82 \pm 0.04^{+0.19}_{-0}$	$4.11 \pm 0.10^{+0.23}_{-0}$	$4.80 \pm 0.10^{+0.13}_{-0}$
DNM	$4.4 \pm 0.1^{+0.2}_{-0}$	$3.9 \pm 0.1^{+0.2}_{-0}$	$7.3 \pm 0.3^{+0.2}_{-0}$
CO	$2.6 \pm 0.2^{+0.1}_{-0}$	$2.1 \pm 0.2^{+0.1}_{-0}$	$5.7 \pm 0.3^{+0.1}_{-0}$

the average $A_{VQ}/N_{\rm H}$ ratio, opacity, and specific power in the three H I structures; they are listed in Table 2. The dust properties compare reasonably well in the local Chamaeleon cloud and in the IVA, despite the broad wings of the H I lines in the latter, which reflect an unusual dynamical state (perhaps shocked gas) or large internal shear. The relatively warm ($\gtrsim$20 K) dust in the Galactic disc, lying at large height above the plane, exhibits an equivalent $A_{VQ}/N_{\rm H}$ ratio, but a 30% lower opacity and 30% higher power than in the foreground clouds. All opacities and powers appear to be significantly larger than the values of $(7.1 \pm 0.6) \times 10^{-27}$ cm^2 and 3.6×10^{-31} W measured in high-latitude cirrus clouds exposed to the local ISRF (Planck Collaboration Int. XVII 2014; Planck Collaboration XI 2014). We further discuss in Sect. 9 how the dust characteristics evolve with environment.

The strong correlations found between the γ-ray intensity and dust emission in the DNM yield a first measure of the average dust characteristics per gas nucleon in this phase. Their values are given by the $q_{\rm HI\,Cha}/q_{\rm DNM}$ ratios under the assumption of a uniform CR flux across the H I and DNM phases. This hypothesis is corroborated by the same γ-ray emissivity spectra and moderate volume densities of the gas in both phases. From the fits in the four independent energy bands, we find the weighted averages listed in Table 2. They closely match those obtained with the high photon statistics of the overall energy band. Figure 9 shows a marginally significant decreasing trend from 0.4 to 2.3 pc in sampling scale. It relates to the dust evolution discussed in the next section.

We derive mean dust properties in the CO-bright phase from the values of $y_{\rm CO}$ and the corresponding γ-ray $X_{{\rm CO}\gamma}$ factors. The results are given in Table 2. They complement the measures in the H I and DNM phases to reveal a pronounced rise in opacity, a milder one in $A_{VQ}/N_{\rm H}$, and a 30% decrease in specific power as the gas becomes denser across the phases. The power decrease may be due to the loss of optical/UV radiation from the diffuse envelopes to the dense CO clouds. This moderate evolution biases the $X_{\rm COR}$ derivation only slightly downward. We note, however, that the average $4\pi\overline{R/N_{\rm H}}^{\rm CO}$ power in the CO-bright phase is larger than $4\pi\overline{R/N_{\rm H}}^{\rm DNM}$ in the DNM, while we expect a fainter ISRF in the more shaded CO cores. This inversion is due to the presence of a few high-power spots in the CO clouds. Their high values maintain the average at a high level, despite the marked power decrease around them (see Figs. 11 and 12 of Sect. 9).

All-sky averages of the $E(B-V)/R$ and $E(B-V)/\tau_{353}$ ratios have been measured from the correlation between the dust emission data and quasar colours (Planck Collaboration XI 2014). We have used these ratios to convert the opacities and specific powers of Table 2 into $N_{\rm H}/E(B-V)$ ratios. We have also used $R_V = 3.1$ to convert the $A_{VQ}/N_{\rm H}$ ratios. The results are presented in Table 3. We note a significant dispersion according to the choice of dust tracer in all gas components. The dispersion greatly exceeds the statistical errors. The values in the CO phase are at clear variance because of the dust evolution that is discussed in the next section. Departures from the canonical $N_{\rm H} = 5.8 \times 10^{21}$ cm^{-2} $E(B-V)$ relation (Bohlin et al. 1978) have been recently noted as a function of Galactic latitude (Liszt 2014). The reported all-sky averages span values from around 4 to 9×10^{21} cm^{-2}. The values we find in the Chamaeleon complex are generally lower than the canonical one, but not unreasonably so for medium-latitude clouds (compare with Fig. 5 of Liszt 2014). Beyond these latitude variations, the results of our study call for caution in: (i) the choice of dust emission tracer to derive $N_{\rm H}/E(B-V)$ estimates; and (ii) the application of an all-sky average to a particular environment as the dust properties evolve.

9. Dust evolution between gas phases

Dust opacities at submillimetre frequencies provide information on the dust-to-gas mass ratio and on the mass emission coefficient of the big grains. Their values often serve to estimate gas masses from dust emission at submillimetre and millimetre wavelengths within our Galaxy or in external galaxies. Establishing the evolution, or lack of evolution, of dust opacities across the various gas phases is therefore essential for numerous studies using dust to trace interstellar matter. Maps of $\tau_{353}/N_{\rm H}$ and $4\pi R/N_{\rm H}$ across the clouds can jointly serve to investigate whether the lower temperatures found in the dense regions result from an increased emission coefficient due to grain structural or chemical evolution, and/or from the ISRF attenuation in shaded areas. Under the assumptions that the large grains are well mixed with gas, that they have reached equilibrium temperatures between the heating rate and radiated power, and that the modified blackbody fits reliably characterize their SEDs, the specific-power map follows the first-order variations in heating rate.

To map spatial variations of the dust properties per gas nucleon around the averages discussed in Sect. 8, we have produced two different sets of total $N_{\rm H}$ column densities. They enable a check of the impact of the current limitations in tracers of the total gas.

– For the first set, which we denote $N_{{\rm H}\,\gamma}$, we have converted the interstellar γ-ray intensity into gas column density using the emission rate found in the local atomic gas. The γ-ray intensity from the ISM is obtained from the LAT data in the overall energy band after subtraction of the γ-ray counts unrelated to gas (using the best fit parameters for the ancillary

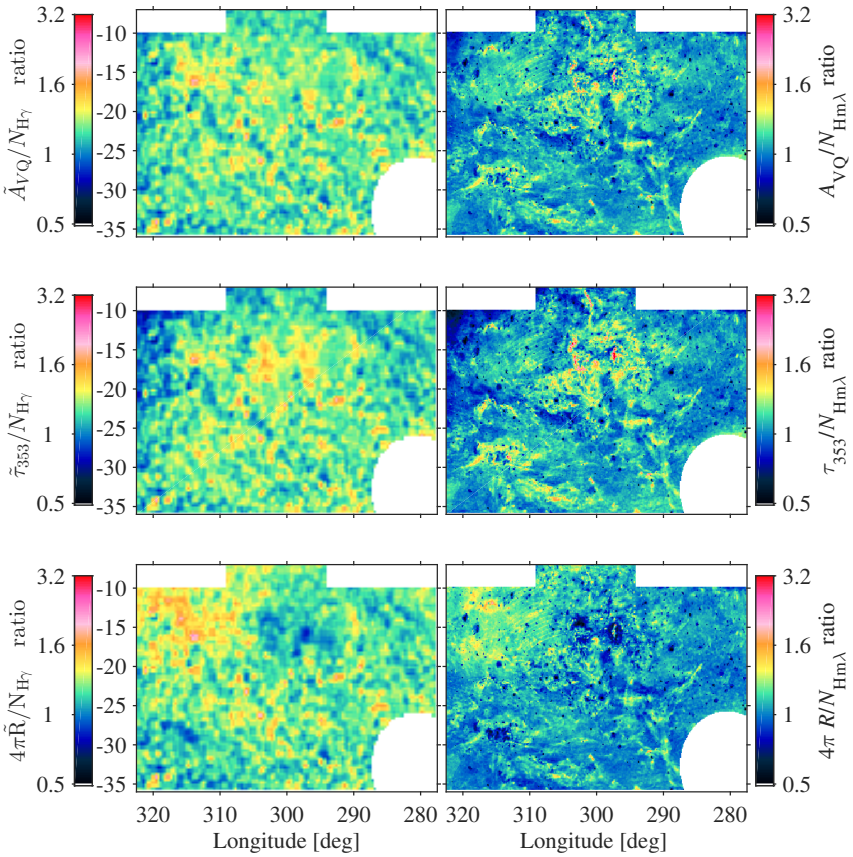

Fig. 12. Spatial variations of the dust properties per gas nucleon, relative to the average values obtained at low N_H, in the $(1-2.2)\times10^{21}$ cm^{-2} interval for $N_{H\gamma}$ (*left column*), and in the $(0.4-2)\times10^{21}$ cm^{-2} interval for $N_{Hm\lambda}$ (*right column*). As in the previous figure, the total gas is measured by $N_{H\gamma}$ on a 0.°375 pixel grid (*left*) and by $N_{Hm\lambda}$ on a 0.°125 pixel grid (*right*). Colours saturate for ratios below 0.5 and above 3.2.

components of Eq. (3)). We have checked that the other four independent energy bands yield similar maps. We have downgraded the binning to 0.°375 to reduce the Poisson noise and photon discretization. On the one hand, $N_{H\gamma}$ does not take into account the small (<20%) γ-ray emissivity variations between the H I structures; on the other hand no assumption is made, beyond the uniformity of the CR flux, on the irregular H I optical depth, uneven CO-to-H_2 conversion, and DNM structure. $N_{H\gamma}$ therefore gives an estimate of the total N_H, independently of the chemical or thermodynamic state of the gas.

– For the second set, which we denote $N_{Hm\lambda}$, we have used the higher-resolution multiwavelength information from the N_{HI}, W_{CO}, and γ-ray $N_{H_{DNM}}$ maps. We have included the gas from all phases and velocity components, with optically thin H I and the γ-ray $X_{CO\gamma}$ factor deduced from the γ+A_{VQ} analysis that best matches the LAT data. We warn the reader that the corresponding maps of the dust properties per gas nucleon are less reliable at the smallest angular scales because $N_{Hm\lambda}$ uses approximations assessed over the whole complex (e.g. uniform $X_{CO\gamma}$, optically thin H I, etc.). We stress that the use of the higher values of X_{COAvQ} and $X_{CO\tau}$ for the construction of the A_{VQ}/N_H and τ_{353}/N_H maps hardly lowers their contrast because of the large quantities of H I and DNM gas that do not depend on X_{CO}.

To investigate non-linear departures from the average properties discussed in Sect. 8, we have produced four sets of plots in Figs. 10 to 13.

– Figure 10 directly explores the correlations between the dust and γ-ray signals produced in the gas, with a common 0.°375 binning. The slope follows the evolution of the dust properties per gas nucleon in intervals of increasing $N_{H\gamma}$.
– Figures 11 and 12 explore the spatial variations of the dust properties per gas nucleon as traced side by side with $N_{H\gamma}$ and $N_{Hm\lambda}$, in absolute and in relative units.
– Figure 13 explores the evolution of the mean dust properties in intervals of increasing N_H, of increasing molecular fraction in N_H, and of increasing dust temperature. The values have been obtained with $N_{Hm\lambda}$ binned at 0.°125.

Together these investigations provide compelling evidence for dust evolution across the Chamaeleon complex. Figure 10 illustrates the tight correlations that exist between the γ-ray flux emerging from the gas and the dust maps, $\tilde{A}_{VQ}$, $\tilde{\tau}_{353}$ and $\tilde{R}$, convolved with the LAT response. We obtain Pearson's correlation coefficients of 0.8 for all cases. We detect curvature in all correlations, with a gradual downward curvature for $\tilde{R}$, a marked upward curvature for $\tilde{\tau}_{353}$, and a milder one for $\tilde{A}_{VQ}$.

These curvatures, together with the significant trends shown in Fig. 13 and the spatial coherence of the variations seen in Fig. 11, provide evidence that the dust opacity at 353 GHz varies by a factor of 2 to 4.6 and that the radiative emissivity of the grains (via A_{VQ}/N_H) varies by a factor of 1.5 to 2.9, according to the environmental conditions in the gas density and chemistry.

We can readily recognize the cloud structures in the A_{VQ}/N_H and τ_{353}/N_H gradients across the field, so the maps depict a gradual evolution of the dust properties across the complex, with gradients of comparable magnitude in several clouds. The rise is already perceptible in the DNM phase, even though the column-density range over which it is extracted largely overlaps that of the H I. The rise steepens near or in the brightest CO cores. The higher angular resolution of the $N_{Hm\lambda}$ map captures the large dynamic range in the compact regions of highest density, with a 4-fold contrast in opacity and a 3-fold contrast in A_{VQ}/N_H ratio between those peaks and the diffuse H I. The opacity peaks are confirmed in the $N_{H\gamma}$ map, with a lower contrast due to

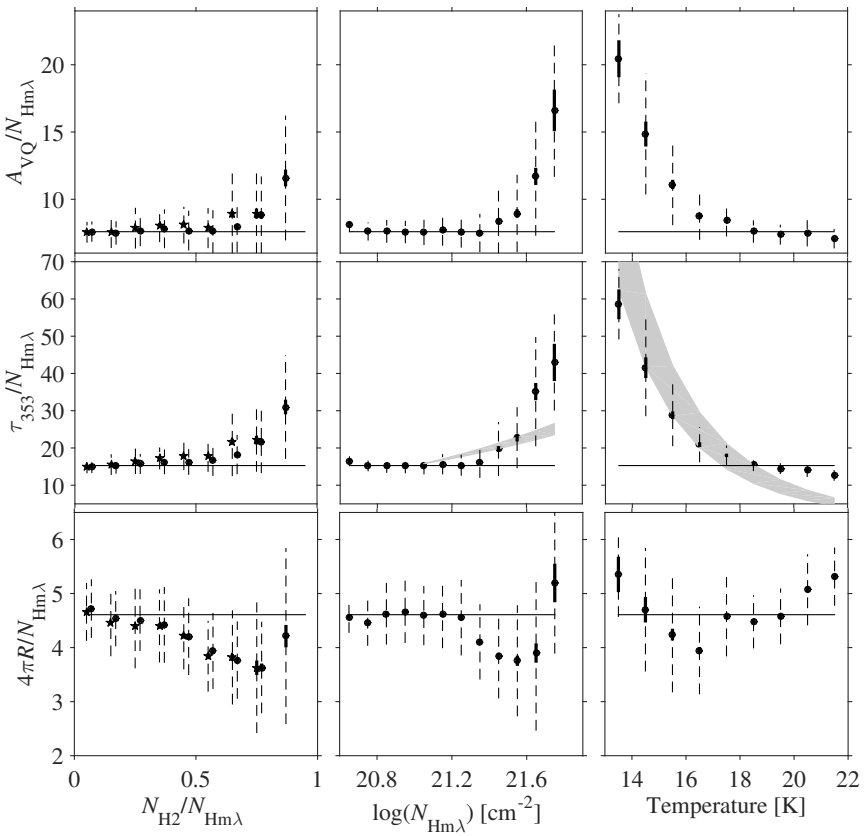

Fig. 13. Evolution of the dust properties per gas nucleon in intervals of molecular fraction in the gas column (*left*), of total gas column density $N_{H\,m\lambda}$ (*middle*), and of dust colour temperature (*right*). The A_{VQ}/N_H ratios are in units of 10^{-22} mag cm^2, τ_{353}/N_H in 10^{-27} cm^2, and $4\pi R/N_H$ in 10^{-31} W. To estimate the molecular fraction in N_H, we have assumed a DNM composition between half (stars) and fully (dots) molecular. The solid and dashed error bars respectively give the error on the means and the standard deviations in each sample. The thin lines mark the average values found in the $(0.4–2)\times10^{21}$ cm^{-2} range. The shaded area in the temperature plot shows the expectation for uniform radiated powers ranging between 3.4 and 5×10^{-31} W H^{-1}, with the mean index $\beta = 1.65$ in the region. A power-law variation in opacity, $\sigma_{353} \propto {N_H}^{0.28\pm0.03}$, has been reported above 10^{21} cm^{-2} in Orion. The shaded curve in the central plot shows this trend scaled at the value of the Chamaeleon complex opacity at $N_{H\,m\lambda} = 10^{21}$ cm^{-2}.

the lower angular resolution. The gradual evolution of the dust properties is responsible for the change in mean A_{VQ}/N_H and τ_{353}/N_H values across the gas phases in Table 2. The values in the DNM phase may be driven up by the large column densities in excess of 10^{21} cm^{-2} observed around the brightest CO cores of Cham I, II, and III. However, Fig. 13 indicates that these ratios start to rise as soon as H_2 molecules dominate over H atoms in the gas column.

The opacities measured at 353 GHz in the Chamaeleon complex are interestingly larger than the average trends previously found over the whole sky. In pure H I, in the $(0.4–2.0)\times10^{21}$ cm^{-2} range, we measure a mean (standard deviation) opacity of 14.3 $(2.3)\times10^{-27}$ cm^2 for a radiated power of 4.5 $(0.4)\times10^{-31}$ W. This is a factor of 2 larger than the value estimated in the high-latitude H I cirrus clouds where the radiated power is 25% lower than in the Chamaeleon complex (Planck Collaboration Int. XVII 2014). So, we confirm large opacity variations within the atomic phase at column densities below 10^{21} cm^{-2}, away from the conditions that cause dust evolution in the cold molecular environments. This large change within the diffuse atomic phase challenges the dust evolution models. Figure 13 further shows a constant opacity near 15×10^{-27} cm^2 in the $(0.4–2.0)\times10^{21}$ cm^{-2} interval in total N_H, whereas the all-sky average rises from 7.3 to 12×10^{-27} cm^2 over the same N_H range (Planck Collaboration XI 2014). Augmenting the H I optical depth correction at the 2σ confidence limit in spin temperature does not reconcile these measurements. The discrepancy extends to the CO phase, with peak opacities in the Chamaeleon clouds that are 3.5 times larger than the all-sky average over the same N_H range (see Fig. 21 of Planck Collaboration XI 2014). Figure 13 shows that the opacity rise in the Chamaeleon complex is also steeper than the $\tau_{353}/N_H \propto N_{Htot}^{0.28\pm0.01\pm0.03}$ dependence found in the Orion clouds, even though it was measured to much larger gas column densities (using near-infrared stellar reddening, Roy et al. 2013). The X_{CO} factor in the Chamaeleon clouds is not abnormally low compared to that in other nearby clouds (see Sect. 7). Its value cannot cause a large overestimation of the grain opacities in the Chamaeleon molecular cores.

The dust specific powers vary only moderately, by less than a factor of 2, inside the DNM and CO clouds in Figs. 11 and 12. The power variations hardly relate to the gas structure, except for two notable trends. The first is seen toward the denser DNM filaments, where both the radiated power and opacity exceed the surrounding values by 30–50%. The second is a power decline by a factor of 2 toward the bright CO clouds of Cham I, II, III, and East II, in regions where the dust temperature drops below 18 K and the column density exceeds about 2×10^{21} cm^{-2}. Figure 13 shows that the power drop relates to the presence of molecular gas. The low-power regions extend well beyond the densest filaments with the largest opacities (see Fig. 11); they are detected with both $N_{H\,\gamma}$ and $N_{H\,m\lambda}$.

We have found no explanation for the 30% to 60% larger powers measured in the north-eastern corner of the field, where the opacities are close to the average, but the grain temperatures exceed 20 K. The IC emission map of Fig. 3 gives the integral along sightlines of the CR interactions with the global Galactic ISRF. Its asymmetry in longitude at $b > -20°$ suggests an enhanced ISRF, thus an enhanced heating rate, toward the warm grains. Yet, the warm region extends beyond our analysis perimeter and its global spatial distribution does not follow the smooth distribution of the Galactic ISRF, nor any gas structure (see Fig. 9 of Planck Collaboration XI 2014). The abrupt change in dust SEDs, with $\beta < 1.6$ in this zone, also warns us that the temperature excess may not relate to large-scale stellar distributions.

The clear anti-correlation we see in Fig. 13 between the dust opacity and temperature confirms the early results obtained in

the diffuse ISM (Planck Collaboration XXIV 2011) and in high-latitude cirrus clouds (Planck Collaboration Int. XVII 2014), now with the independent gas-tracing capability of the γ rays. It reveals, however, a more complex situation than the anticipated temperature response of the grains to an opacity change while exposed to a uniform heating rate. On the one hand, since A_{VQ} has been corrected to first order for an ISRF-related bias, the residual change in $A_{VQ}/N_{\rm H}$ revealed in Figs. 10 and 13 suggests an emissivity rise due to a structural or chemical evolution of the grains. On the other hand, the grains are less heated in the regions of low $4\pi R/N_{\rm H}$ in the CO phase. The maps show a variety of situations inside the clouds, but two notable trends emerge. The lowest temperatures near 15 K correspond to regions of median power and highest opacity, so they may be due to the enhanced radiative cooling of the grains. Conversely, the regions of lowest power exhibit median opacities, so the low temperatures near 17 K in these environments may primarily result from a reduced heating rate.

The chemical composition of the DNM is likely to encompass varying fractions of optically thick H I and CO-dark H_2 along different lines of sight, as they approach the CO edges. Optically thick H I has been proposed to explain the excesses of dust emission over the thin $N_{\rm H\,I}$ and $W_{\rm CO}$ expectations, which would make it the dominant form of DNM (Fukui et al. 2014, 2015). Thick H I would not explain the $\tau_{353}/N_{\rm H}$ variations by a factor above 3 seen in the thin H I cirrus clouds at $N_{\rm H\,I}$ column densities predominantly below a few 10^{20} cm^{-2} (Planck Collaboration Int. XVII 2014). Nor would it explain the $\tau_{353}/N_{{\rm H}\,\gamma}$ variations seen in γ rays across the H I and DNM phases, independently of H I depth corrections and $X_{\rm CO}$ conversions. It would be difficult to invoke thick H I to explain large cloud-to-cloud variations in $\tau_{353}/N_{\rm H}$ over the same $N_{\rm H}$ range in the different clouds. Dust evolution thus currently prevents the use of dust emission to study optically thick H I. The magnitude of the observed rise in $\tau_{353}/N_{\rm H}$ or of the ISRF-corrected $A_{VQ}/N_{\rm H}$ with $N_{\rm H}$ is such that it would systematically lead to a substantial overestimation of $N_{\rm H\,I}$.

10. Gas phase interfaces

In this section we compare the gas column densities inferred in the different phases of the local clouds.

We note in the solid angle distributions of Fig. 14 that all three phases reach comparable peak column densities between 1 and 3 $\times 10^{21}$ cm^{-2} in these modest clouds. For the DNM, the histograms confirm the good correspondence in the three analyses between the column densities derived in γ rays and those derived from the dust and calibrated in mass with the γ rays. The differences stem from the lower resolution in γ rays (see Fig. 8). Figure 14 stresses that the mean dust properties given for each phase in Table 2 originate from broad and largely overlapping $N_{\rm H}$ ranges.

Figure 15 compares the spatial distributions in each phase for the γ+A_{VQ} analysis. The other analyses yield comparable maps. They illustrate how the DNM filamentary structure generally extends at the transition between the diffuse H I and the compact CO cores of the Chamaeleon complex, but that the transition substantially varies inside the complex. For instance, the elongated, snaky CO filament that stretches along $b = -22°$ in Cha-East I is not surrounded by DNM gas, while the similar Musca CO filament, extending at low latitude along $l = 301°$, is embedded in a rich DNM structure. The CO cloudlet at $l = 301°$, $b = -24°$ is free of DNM while the DNM cloud near $l = 307°$, $b = -10°$ is almost free of CO emission (see the *Planck* TYPE 3 CO map, Planck Collaboration XIII 2014).

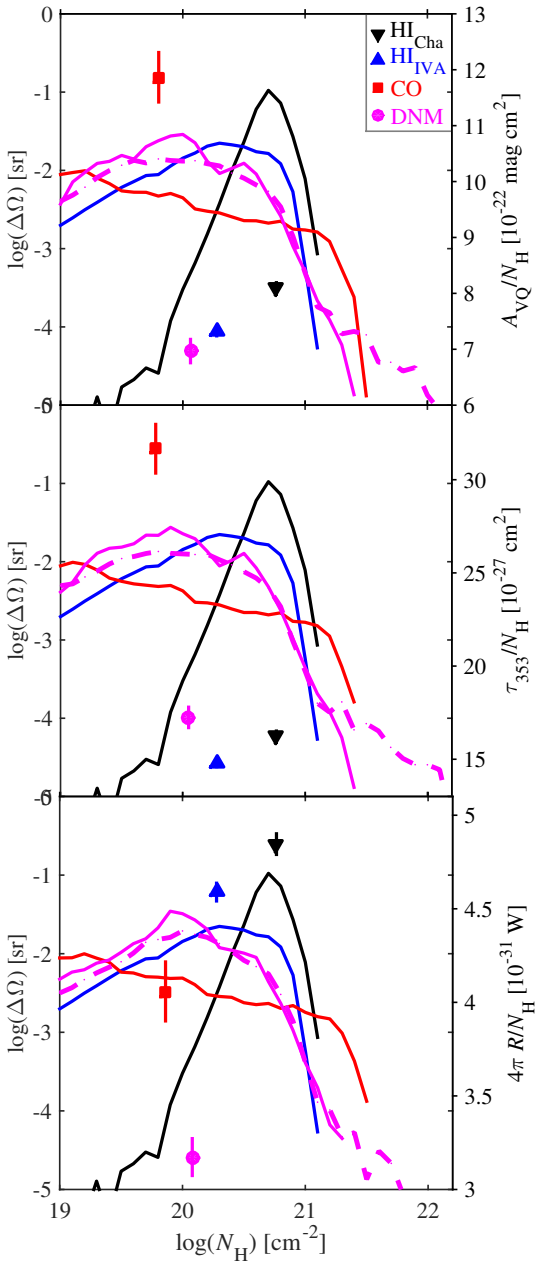

Fig. 14. Solid angle distributions of $N_{\rm H}$ in the different gas phases from the three analyses: in the optically thin H I gas of the local cloud and intermediate-velocity arc; in the DNM gas as traced in γ rays (solid) or in dust (dashed); and in the CO phase with the γ-ray derived $X_{\rm CO}$ factors. The data points give the mean dust properties ($A_{VQ}/N_{\rm H}$, opacity, and specific power) in each phase. They are placed at the position of the average column density in each phase. The insert gives the colour code and symbol for each phase.

The bright DNM clouds at $l < 296°$ and $b < -20°$ are almost free of CO emission down to 1 K km s^{-1}. Whether they relate to the IVA would be worth investigating in the hope of finding a test case to explore the impact of unusual gas dynamics on the transition from atomic to molecular gas.

Masses in the local Chamaeleon system have been derived for a common distance of 150 pc and with the γ-ray DNM maps, despite their lower angular resolution, in order to be less sensitive to dust evolution. With the γ+A_{VQ} analysis, we obtain

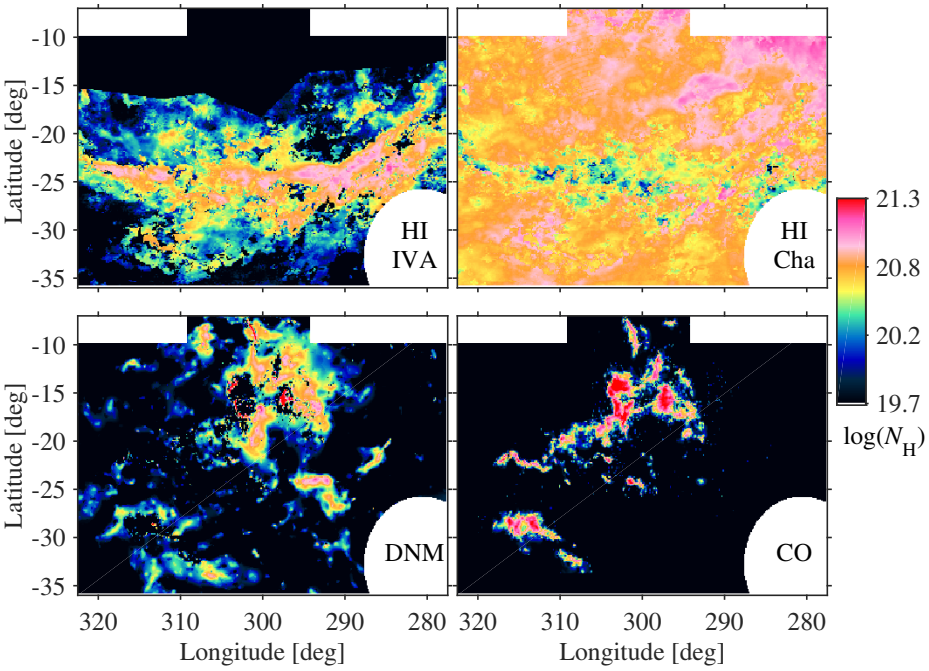

Fig. 15. $N_{\rm H}$ maps (in cm^{-2}) for the different gas phases in the analysis region: H I in the intermediate velocity arc and, inside the Chamaeleon complex, gas in the H I, DNM, and CO-bright phases. The maps are based on the γ+A_{VQ} analysis, with the assumption of optically thin H I, the value of $X_{\rm CO\gamma}$, and the dust DNM template calibrated in mass with the γ rays.

masses of $44\,900^{+1600}_{-0}$ $M_\odot$ in the H I, $9000 \pm 500^{+400}_{-0}$ $M_\odot$ in the DNM, and $5000 \pm 200^{+200}_{-0}$ $M_\odot$ in the CO-bright H_2. They primarily reflect the compactness of the various phases. The DNM is the second most important contributor to the total mass because of its wide $N_{\rm H}$ range and large spatial extent. We obtain comparable masses within ±4% in the DNM and within $^{+15}_{-5}$% in the CO phase with the other analyses.

We have studied the relative contributions and transitions between the different phases for the local Chamaeleon complex and for five of its sub-structures, as listed in Sect. 2.5 and outlined in Fig. 2. They have been chosen to lie outside the zone where H I lines may overlap between the local and IVA components. To build the fractional curves of Fig. 16, we have used the γ+A_{VQ} analysis, the $X_{\rm CO\gamma}$ factor, the γ-ray $N_{\rm H_{DNM}}$ map, and a DNM composition between half and fully molecular. The other analyses yield similar curves. In the text below, we have translated $N_{\rm H}$ into visible extinction with the $N_{\rm H}/A_V$ ratio of $(2.15 \pm 0.14) \times 10^{21}$ cm^{-2} mag^{-1} measured with the Far Ultraviolet Spectroscopic Explorer (FUSE, Rachford et al. 2009). To study the variations in DNM or dark-H_2 fraction with A_V, we have directly used the A_V map constructed from the 2MASS stellar data, with the median colour excess of the 49 stars nearest to each direction (Rowles & Froebrich 2009). We have resampled the map into our analysis grid. The visual extinctions are quoted in magnitudes.

All the clouds exhibit similar fractional trends. The H I fractions sharply decline beyond about 8×10^{20} cm^{-2} (or $A_V \sim 0.4$), in agreement with previous measurements, which indicate an H I saturation at (3–5), (4–5), and $(8–14) \times 10^{20}$ cm^{-2} respectively with FUSE observations of H_2 (Gillmon et al. 2006), OH observations (Barriault et al. 2010), and dust observations in Perseus (Lee et al. 2012). Models indeed require $N_{\rm H\,I}$ near 10^{21} cm^{-2} to shield H_2 against UV dissociation for clouds of solar metallicity (Krumholz et al. 2009; Liszt 2014).

The DNM is concentrated in the 10^{20}–10^{21} cm^{-2} interval. It is systematically present before the onset of CO. The H I-DNM transition occurs well into the translucent zone (van Dishoeck & Black 1988), yet at different thresholds ranging from 2 to 8×10^{20} cm^{-2} (or 0.09 to 0.4 in A_V) for the different clouds.

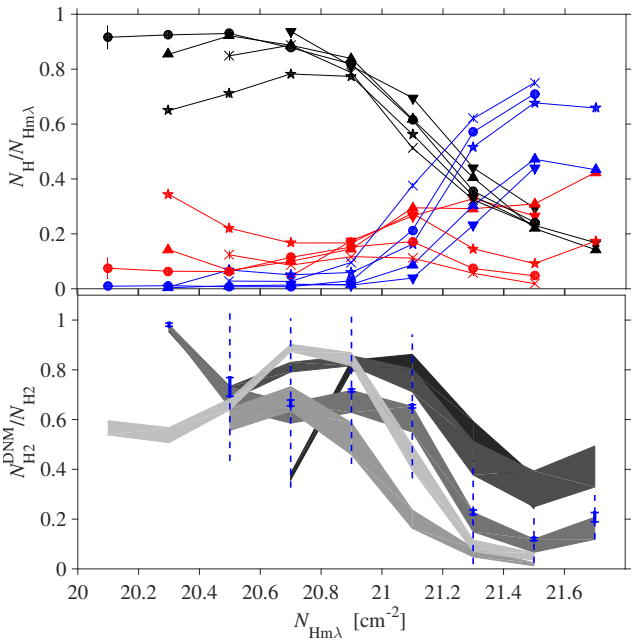

Fig. 16. Variations with $N_{\rm Hm\lambda}$, in five separate clouds, of the fraction of the total column density in each phase (*upper panel*, H I in black, DNM in red, CO in blue) and of the fraction of the total H_2 column density that is CO dark (*lower panel*). Downward and upward triangles, stars, crosses, and circles refer to Musca, Cham I, Cham II+III, Cham East I, and Cham East II, respectively. The dark to light grey curves correspond to the clouds in the same order. The shaded areas cover the chosen uncertainty in DNM composition from 50% to 100% H_2. The dotted and solid error bars give the standard deviations and errors on the mean in each $N_{\rm H}$ bin; they are shown for only one cloud and the fully molecular DNM case.

The transition to CO appears to be more stable, with all five clouds requiring about 1.5×10^{21} cm^{-2} (or $A_V \simeq 0.7$) to efficiently shield CO against photodissociation in the local ISRF. The transition cannot be attributed to the sensitivity threshold of the CO survey. It is consistent with the $A_V \simeq 0.5$ transition noted

Table 4. For the whole local complex and for separate substructures: total gas mass; fractions of the total mass in the three gas phases; mean and peak extinctions within the CO boundaries; and mass fractions of the H_2 that is CO dark.

Structure	$M_{\rm tot}$ [$M_\odot$]	$f_{\rm H\,I}$ [a]	$f_{\rm DNM}$	$f_{\rm H_2\,CO}$
Cham complex	58 900 ± 500	0.76 ± 0.01	0.15 ± 0.01	0.08 ± 0.01
Musca	5100 ± 100	0.70 ± 0.01	0.24 ± 0.01	0.06 ± 0.01
Cha I	10 200 ± 100	0.64 ± 0.01	0.23 ± 0.01	0.12 ± 0.01
Cha II+III	7700 ± 100	0.57 ± 0.01	0.19 ± 0.01	0.24 ± 0.01
Cha East I	3100 ± 100	0.74 ± 0.01	0.10 ± 0.01	0.15 ± 0.01
Cha East II	10 100 ± 100	0.78 ± 0.01	0.13 ± 0.01	0.08 ± 0.01
	$\overline{A_V}$ [mag]	$A_V^{\rm max}$ [mag]	$f_{\rm dark\,H_2}$ [b]	$f_{\rm dark\,H_2}$ [c]
Cham complex	0.7	7.1	0.48 ± 0.03	0.64 ± 0.04
Musca	0.9	4.3	0.68 ± 0.05	0.81 ± 0.06
Cha I	0.8	7.1	0.48 ± 0.03	0.65 ± 0.04
Cha II+III	0.7	6.5	0.29 ± 0.02	0.45 ± 0.03
Cha East I	0.4	2.2	0.25 ± 0.02	0.40 ± 0.03
Cha East II	0.6	2.9	0.45 ± 0.03	0.62 ± 0.04

Notes. [a] For optically thin H I. [b] For a half molecular DNM. [c] For a fully molecular DNM.

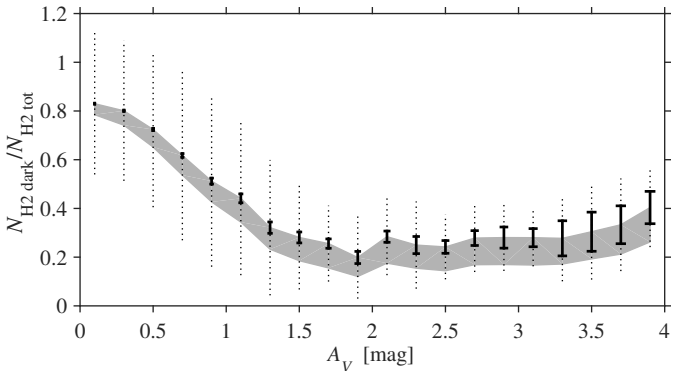

Fig. 17. Evolution of the CO-dark to total H_2 column-density ratio with the 2MASS visual extinction. The molecular fraction in the DNM varies from 50% (lower grey bound) to 100% (upper bound). The gas column densities in the CO and DNM phases have been obtained with the $X_{\rm CO\gamma}$ factor and the γ-ray $N_{\rm H_{DNM}}$ map from the γ+A_{VQ} analysis. The other analyses yield equivalent curves. The thick and dotted lines respectively give the standard error of the mean and the standard deviation of the ratios for each A_V bin, in the case of a fully molecular DNM.

for the formation of the OH molecule that is one of the precursors of CO in the chemical evolution (Barriault et al. 2010).

We have not noted any obvious difference in H I column densities or line widths that could relate to the variable DNM onset at low $N_{\rm H}$. However, simultaneous H I and H_2 observations with FUSE have suggested a rather complex and variable H I–to–H_2 interface, with $2N_{\rm H_2}/(N_{\rm H\,I} + 2N_{\rm H_2})$ rapidly fluctuating between 0.1 and 0.7 up to $A_V \simeq 2.6$ (Rachford et al. 2009). Figure 15 exhibits rather steep CO edges that occur in an $N_{\rm H}$ regime where an equilibrium set of reactions involving C^+ and OH leads to CO formation (Sheffer et al. 2008). So the DNM variations at lower $N_{\rm H}$ may conversely reflect the non-equilibrium chemistry that prevails in more diffuse gas. They may also reflect local variations in the H I optical thickness that could not be taken into account in our analyses.

We have followed the variation of the CO-dark to total H_2 ratio in column density, assuming that the DNM consists of 50% or 100% molecular hydrogen. Figure 16 shows the trend with $N_{\rm H}$ in the individual clouds and Fig. 17 shows the average evolution with A_V over the whole complex of local and IVA clouds. To compute the latter, we have subtracted the extinction associated with the Galactic background $N_{\rm H\,I}$ using the $N_{\rm H}/A_V$ ratio of FUSE. We obtain substantially the same profiles with the γ+τ_{353} and γ+R analyses. As expected, the dark-H_2 fraction steeply rises to 80% in regions heavily exposed to the ISRF and the CO-bright phase rapidly takes over the molecular fraction once CO is fully shielded, at $A_V > 1.2$. This is deeper into the clouds than the theoretical prediction of $A_V \gtrsim 0.5$–0.7 for optically thick CO in a $10^5\,M_\odot$ cloud with an incident UV flux extrapolated to the local ISRF (see Fig. 7 of Wolfire et al. 2010). The DNM contributes more than half of the molecular gas up to $A_V \simeq 0.9$. It retains 10–30% of the molecular column densities to high A_V as the lines of sight intersect envelopes of the CO-bright clouds. This is consistent with the theoretical finding that 20% of H_2 is not traced by CO even at the density peak (Levrier et al. 2012).

The fractions of CO-dark to total H_2 in mass, $f_{\rm dark\,H_2}$, are listed for each cloud in Table 4 for the two choices of DNM composition. The fractions indicate there is often as much molecular mass in the inconspicuous DNM as in the CO-bright cores. They also often exceed the 32% prediction for CO cloudlets exposed to the local ISRF (Levrier et al. 2012), or the 25% prediction based on the PDR modelling of the outer layers of a $10^5\,M_\odot$ spherical cloud if we extrapolate its illumination to the local ISRF (Wolfire et al. 2010). The latter model suggests that the extinction difference, ΔA_V, between the H I-H_2 and the H_2-CO transitions is a weak function of the outside UV flux. However, as the mean extinction, $\overline{A_V}$, through the cloud measures the total molecular mass, the dark-H_2 mass fraction should decline with increasing $\overline{A_V}$. It is difficult to transpose the mean extinction in the homogenous, spherical, and giant ($10^6\,M_\odot$) cloud of the model with the average extinction in the observations. To help the comparison, we have taken averages, $\overline{A_V}^{\rm CO}$, within the well-defined CO edges at $W_{\rm CO} > 1\,{\rm K\,km\,s^{-1}}$. The model predicts $f_{\rm dark\,H_2} > 70\%$ for the $0.4 \lesssim \overline{A_V} \lesssim 0.9$ range of the present clouds. We find lower fractions in the observations in Table 4. The model also predicts a strong decline in $f_{\rm dark\,H_2}$ with

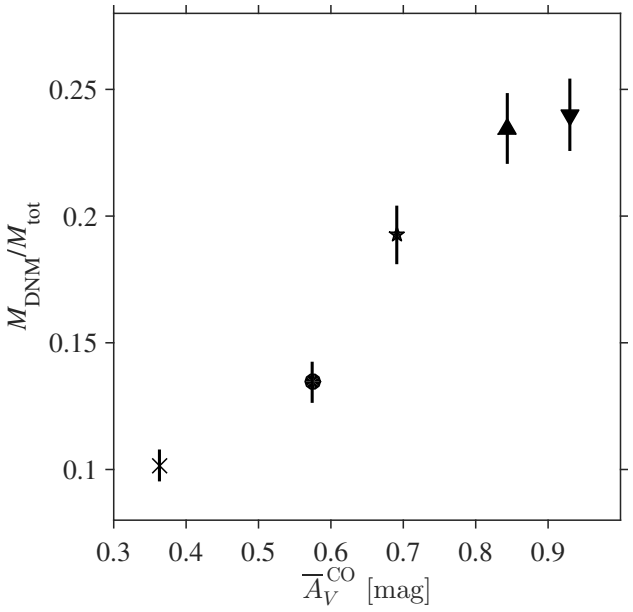

Fig. 18. Evolution of the DNM mass fraction with the average 2MASS extinction measured within the CO boundaries of each cloud. Downward and upward triangles, stars, crosses, and circles refer to Musca, Cham I, Cham II+III, Cham East I, and Cham East II, respectively.

increasing $\overline{A_V}$, whereas the data in Table 4 hint at an opposite trend, with a Pearson's correlation coefficient of 0.81 for a rise.

The DNM contains 10% to 24% of the total gas mass in individual clouds as well as in the whole complex (see $f_{\rm DNM}$ in Table 4). These mass fractions do not depend on the DNM chemical composition. The fraction for the whole complex is consistent with the early estimate based on more limited, but independent data (EGRET in γ rays and DIRBE-IRAS for the dust; Grenier et al. 2005). It is, however, lower than the mean (43 ± 18)% fraction derived from C^+ lines in CO clouds of the Galactic disc for a comparable sensitivity in ^{12}CO (Langer et al. 2014). The early γ-ray analyses suggested that $f_{\rm DNM}$ decreases as the mass locked in the CO phase grows. The recent C^+ line results also indicate reduced fractions of 18% toward dense ^{13}CO clouds and 13% toward the denser $C^{18}O$ cores (Langer et al. 2014). In the Chamaeleon complex, we find no correlation between $f_{\rm DNM}$ and any of the cloud masses (correlation coefficients of 0.1, 0.2, and 0.3, respectively for the H I, CO-bright, and total-cloud mass). Figure 18, however, exhibits a correlation, with a Pearson's coefficient of 0.98, between $f_{\rm DNM}$ and the $\overline{A}_V^{\rm CO}$ extinction averaged inside the CO contours. We stress that the mass fractions and extinctions are based on independent data. Whereas a decline of $f_{\rm DNM}$ or $f_{\rm dark\,H_2}$ with increasing $\overline{A_V}$ can be explained by a shorter screening length to protect the CO phase against photo-dissociation, a rising trend with $\overline{A}_V^{\rm CO}$ is unexpected. It is confirmed for both $f_{\rm DNM}$ and $f_{\rm dark\,H_2}$ in the γ+τ_{353} analysis. Five clouds constitute too scarce a sample to claim a definite increase in DNM abundance with $\overline{A}_V^{\rm CO}$, but the correlation in Fig. 18 calls for the observation of other test cases in more massive molecular complexes, and the discrepancy with theory calls for more detailed predictions for medium-size clouds and more realistic geometries.

11. Conclusions and perspectives

We have explored the gas, dust, and cosmic-ray content of several clouds in the local Chamaeleon complex and in an intermediate-velocity H I arc crossing the field. We have conducted three parallel analyses, coupling the H I, CO, and γ-ray data with different dust tracers, namely the optical depth at 353 GHz, the radiance, and the $U_{\rm min}$-corrected A_{VQ} extinction. Jackknife tests have verified that the uniform set of parameters of the γ-ray and dust models apply statistically to the whole region under analysis. We find that the A_{VQ} map, which includes a linear correction for the ISRF strength in the Draine & Li (2007) model, provides the best fit to the interstellar γ rays. Yet, the corrected extinction still rises significantly above the linear γ-ray expectation as the gas becomes denser. We find an even more pronounced upward curvature in dust optical depth with increasing interstellar γ-ray intensity, and conversely a saturation in dust radiance.

We summarize the main results for each topic as follows.

- *On cosmic rays*: at the precision level of the current γ-ray data, the CR spectrum is shown to be uniform across the gas phases and to follow the energy distribution of the local-ISM average. The γ-ray emissivity per nucleon in the Chamaeleon complex is equivalent to other measurements in the solar neighbourhood. It exceeds the average emissivity found along the solar circle in the Galaxy by only (22 ± 5)%. We find no spectral signature of non-uniform CR penetration to the denser molecular cores traced in ^{12}CO. We provide a first measurement of the γ-ray emissivity in an intermediate-velocity cloud. It is 20% lower than in the Chamaeleon clouds at all energies. We need further measurements in similarly sheared clouds and a distance estimate to the IVA to assess whether the small change in CR flux is due to a larger altitude above the Galactic plane or to the unusual dynamical state of the clouds.
- *On the DNM*: the γ-ray flux and dust tracers reveal large amounts of DNM gas with comparable spatial distributions and mass columns at the interface between the H I-bright and the CO-bright phases of the local complex. We have combined the dust and γ-ray analyses to build reliable DNM templates and to reduce the bias on the H I- and CO-related parameters due to the DNM presence. With the equivalent of a fifth of the H I mass and nearly twice the CO-bright mass, the inconspicuous DNM appears as a major constituent of the complex. Its spatial extent is intermediate between the diffuse H I and compact CO phases. It dominates the molecular column densities up to $A_V \simeq 0.9$.
- *On dust evolution*: we provide average dust properties per gas nucleon ($A_{VQ}/N_{\rm H}$ ratio, $\tau_{353}/N_{\rm H}$ opacity, and $4\pi R/N_{\rm H}$ specific power) in the different gas phases and we follow their spatial variations across the clouds by means of two separate $N_{\rm H}$ maps. The lower resolution one, $N_{{\rm H}\,\gamma}$, is inferred from the γ-ray data. It traces the total gas without any assumption on the in situ, non-uniform H I opacities, $X_{\rm CO}$ conversions, and DNM extraction. It relies only on the uniform CR flux. The higher resolution map, $N_{{\rm H}\,m\lambda}$, uses the radio data and H I, DNM, and CO decomposition with the $\overline{A_{VQ}/N_{\rm H}}^{\rm DNM}$ and $X_{{\rm CO}\gamma}$ factors measured in γ rays. Both means provide evidence for a 2 to 4.6-fold rise in $\tau_{353}/N_{\rm H}$ and a more limited 1.5 to 2.9-fold rise in $A_{VQ}/N_{\rm H}$ over a single decade in $N_{\rm H}$. The dust emissivity is seen to gradually evolve from the diffuse H I to the modest CO cores of the Chamaeleon complex. This variation cannot be attributed to changes in the heating rate of the grains, since we find little variation in specific power in the H I and DNM phases and a 2-fold decline in the dense CO clouds. These results confirm and extend into the DNM and CO-bright phases

the earlier indications of opacity changes found in the atomic gas (Planck Collaboration XI 2014; Planck Collaboration Int. XVII 2014). They confirm with independent radio and γ-ray data the variations suggested by the comparison of dust emission and reddening (Martin et al. 2012; Roy et al. 2013). These variations appear to be intimately linked to the gas structure as the density and molecular fractions grow. They presumably reflect a chemical or structural evolution of the grains. Their magnitude severely limits the use of dust emission to trace the total gas to $N_{\rm H} < 2\times10^{21}$ cm^{-2} in the Chamaeleon clouds. We also find that the dust grains in the Chamaeleon complex radiate 2 to 3 times more per unit mass, or are 2 to 3 times more numerous per gas nucleon, than on average over the whole sky. Within the H I gas, the origin of the two-fold increase in opacity for a 25% higher power compared to the high-latitude H I cirrus clouds also requires elucidation. Cloud-to-cloud variations of this magnitude further limit the gas-tracing capability of the thermal dust emission until we understand their cause. The ISRF-related correction applied to A_{VQ} partially, but not completely, alleviates the upward curvature in dust emissivity. We may be witnessing structural/chemical evolution of the dust grains.

– *On* $X_{\rm CO}$: we provide mean $X_{\rm CO}$ conversion factors in the local clouds. The results elucidate a recurrent disparity between earlier γ-ray and dust calibrations of this factor. The disparity likely finds its origin in the pronounced $\tau_{353}/N_{\rm H}$ rise in the molecular clouds, a rise that induces a significant upward bias, by a factor of 1.9, on $X_{{\rm CO}\tau}$ compared to $X_{{\rm CO}\gamma}$ or $X_{\rm COR}$. Further assessing the magnitude of the bias in more massive, but well resolved, molecular complexes has important implications for extragalactic studies that compare dust emission and CO observations to infer star formation efficiencies. The preferred γ-ray calibration of $X_{\rm CO} \simeq 0.7\times10^{20}$ cm^{-2} K^{-1} km^{-1} s in the Chamaeleon clouds agrees with other estimates in the solar neighbourhood. It stresses, however, an unexplained discrepancy, by a factor of 2, between the measurements in nearby clouds (at parsec scales and with limited spatial confusion between the gas phases) and the averages obtained at a kiloparsec scale in spiral arms (in particular in the Local Arm for the same metallicity and UV flux as in the local ISM). Larger photon statistics are required above a GeV in order to investigate how the sampling resolution and cross-talk between gas phases affect the $X_{\rm CO}$ calibration beyond the solar neighbourhood.
– *On phase transitions*: we have explored how each phase contributes to the total gas column density and to the total mass in five separate clouds. They all show a marked decline in H I fraction around 8×10^{20} cm^{-2} and an onset of CO near 1.5×10^{21} cm^{-2}. The DNM retains 10–30% of the gas column densities to large extinctions because the lines of sight intercept DNM-rich envelopes around the CO-bright interiors. We find that the H I-DNM transition varies from cloud to cloud across the $(2-8)\times10^{20}$ cm^{-2} range, without an obvious explanation in H I intensities or kinematics. The CO-dark to CO-bright H_2 mass fraction often exceeds 50% in the clouds of the complex, as predicted by theory for rather translucent clouds. The DNM contributions to the total cloud masses are low (10%–24%) and they surprisingly scale with the stellar extinction averaged within the boundaries of the CO phase. This trend needs confirmation in a larger sample.

Short-term plans include a thorough investigation of the non-linear rise of the dust emission coefficient per unit mass to higher $N_{\rm H}$ values, together with measurements of the ratio of the emission to absorption cross-sections of the grains as a function of $N_{\rm H}$. The present analyses illustrate the potential of confronting γ-ray, dust, and radio tracers to gauge the amount of gas in the DNM and CO phases in order to follow the dust evolution. We have started to exploit the *Fermi* LAT, *Planck*, and stellar data toward these goals in the case of more massive, well resolved clouds.

Future prospects also include a study of the variable DNM abundance and its relation to the total cloud mass and $\overline{A}_V^{\rm CO}$. The pronounced dust evolution prevents the use of the thermal emission of the grains to gauge the amount of optically thick H I gas in the complex H I–to–H_2 transition (Fukui et al. 2014, 2015). In the absence of extensive H I absorption measurements, OH and CH surveys of the DNM interface can help uncover the cause of the variable DNM abundance. UV spectroscopy shows that the CH-to-H_2 abundance is constant over two decades in $N_{\rm H_2}$ ($10^{19.5-21.5}$ cm^{-2}) in the translucent regime. OH is widespread at $A_V > 0.5$ and it rarely correlates with the surveyed CO (Barriault et al. 2010; Allen et al. 2012). CH and OH surveys can therefore provide key information on the DNM composition and why its relative mass varies from cloud to cloud. Constraining the latter is essential to extrapolate the local DNM abundances to Galaxy-wide values. Early γ-ray estimates suggested a Galactic DNM mass as large as in the CO-bright phase (Grenier et al. 2005). In dust emission, the DNM contribution to $N_{\rm H}$ ranges from 10% in the outer Galaxy to 60% in the inner regions (Planck Collaboration XXI 2011). In C^+ line emission, the DNM amounts to 30% of the Galactic molecular mass and it is as massive as the cold H I (CNM) and CO-bright phases in the outer Galaxy (Pineda et al. 2013). However, the limited angular resolution of the γ-ray data, the changes in the dust radiative properties across gas phases, and the difficult separation of C^+ from the CNM, DNM, and ionized regions, all hamper our ability to reliably measure the DNM mass to large distances. Adding the kinematical information of the CH and OH lines opens promising avenues.

Acknowledgements. The development of *Planck* has been supported by: ESA; CNES and CNRS/INSU-IN2P3-INP (France); ASI, CNR, and INAF (Italy); NASA and DoE (USA); STFC and UKSA (UK); CSIC, MICINN, J.A., and RES (Spain); Tekes, AoF, and CSC (Finland); DLR and MPG (Germany); CSA (Canada); DTU Space (Denmark); SER/SSO (Switzerland); RCN (Norway); SFI (Ireland); FCT/MCTES (Portugal); and PRACE (EU). A description of the Planck Collaboration and a list of its members, including the technical or scientific activities in which they have been involved, can be found at http://www.sciops.esa.int/index.php?project=planck&page=Planck_Collaboration. The *Fermi* LAT Collaboration acknowledges generous ongoing support from a number of agencies and institutes that have supported both the development and the operation of the LAT as well as scientific data analysis. These include the National Aeronautics and Space Administration and the Department of Energy in the United States, the Commissariat à l'Énergie Atomique and the Centre National de la Recherche Scientifique / Institut National de Physique Nucléaire et de Physique des Particules in France, the Agenzia Spaziale Italiana and the Istituto Nazionale di Fisica Nucleare in Italy, the Ministry of Education, Culture, Sports, Science and Technology (MEXT), High Energy Accelerator Research Organization (KEK) and Japan Aerospace Exploration Agency (JAXA) in Japan, and the K. A. Wallenberg Foundation, the Swedish Research Council and the Swedish National Space Board in Sweden. Additional support for science analysis during the operations phase is gratefully acknowledged from the Istituto Nazionale di Astrofisica in Italy and the Centre National d'Études Spatiales in France. Support from the Institut Universitaire de France is acknowledged.

References

Abdo, A. A., Ackermann, M., Ajello, M., et al. 2010, ApJ, 710, 133
Ackermann, M., Ajello, M., Allafort, A., et al. 2011a, Science, 334, 1103
Ackermann, M., Ajello, M., Baldini, L., et al. 2011b, ApJ, 726, 81

Ackermann, M., Ajello, M., Allafort, A., et al. 2012a, ApJ, 755, 22
Ackermann, M., Ajello, M., Allafort, A., et al. 2012b, A&A, 538, A71
Ackermann, M., Ajello, M., Albert, A., et al. 2012c, ApJS, 203, 4
Ackermann, M., Ajello, M., Atwood, W. B., et al. 2012d, ApJ, 750, 3
Ackermann, M., Ajello, M., Allafort, A., et al. 2012e, ApJ, 756, 4
Ackermann, M., Ajello, M., Allafort, A., et al. 2013, ApJ, 778, 82
Ackermann, M., Albert, A., Atwood, W. B., et al. 2014, ApJ, 793, 64
Allen, R. J., Ivette Rodríguez, M., Black, J. H., & Booth, R. S. 2012, AJ, 143, 97
Atwood, W. B., Abdo, A. A., Ackermann, M., et al. 2009, ApJ, 697, 1071
Barriault, L., Joncas, G., Lockman, F. J., & Martin, P. G. 2010, MNRAS, 407, 2645
Blitz, L., Bazell, D., & Desert, F. X. 1990, ApJ, 352, L13
Bohlin, R. C., Savage, B. D., & Drake, J. F. 1978, ApJ, 224, 132
Bolatto, A. D., Wolfire, M., & Leroy, A. K. 2013, ARA&A, 51, 207
Boulanger, F., Bronfman, L., Dame, T. M., & Thaddeus, P. 1998, A&A, 332, 273
Casandjian, J.-M. 2012, AIM Conf. Ser., 1505, 37
Cesarsky, C. J., & Volk, H. J. 1978, A&A, 70, 367
Corradi, W. J. B., Franco, G. A. P., & Knude, J. 2004, MNRAS, 347, 1065
Dame, T. M. 2011, ArXiv e-prints [arXiv:1101.1499]
Dame, T. M., Ungerechts, H., Cohen, R. S., et al. 1987, ApJ, 322, 706
Dame, T. M., Hartmann, D., & Thaddeus, P. 2001, ApJ, 547, 792
Draine, B. T., & Li, A. 2007, ApJ, 657, 810
Fatuzzo, M., Melia, F., Todd, E., & Adams, F. C. 2010, ApJ, 725, 515
Fukui, Y., Okamoto, R., Kaji, R., et al. 2014, ApJ, 796, 59
Fukui, Y., Torii, K., Onishi, T., et al. 2015, ApJ, 798, 6
Gillmon, K., Shull, J. M., Tumlinson, J., & Danforth, C. 2006, ApJ, 636, 891
Gold, B., Odegard, N., Weiland, J. L., et al. 2011, ApJS, 192, 15
Grenier, I. A., Casandjian, J.-M., & Terrier, R. 2005, Science, 307, 1292
Heiles, C., & Troland, T. H. 2003, ApJ, 586, 1067
Hunter, S. D., Bertsch, D. L., Catelli, J. R., et al. 1997, ApJ, 481, 205
Kalberla, P. M. W., Burton, W. B., Hartmann, D., et al. 2005, A&A, 440, 775
Kalberla, P. M. W., McClure-Griffiths, N. M., Pisano, D. J., et al. 2010, A&A, 521, A17
Krumholz, M. R., McKee, C. F., & Tumlinson, J. 2009, ApJ, 693, 216
Langer, W. D., Velusamy, T., Pineda, J. L., Willacy, K., & Goldsmith, P. F. 2014, A&A, 561, A122
Lee, M.-Y., Stanimirović, S., Douglas, K. A., et al. 2012, ApJ, 748, 75
Levrier, F., Le Petit, F., Hennebelle, P., et al. 2012, A&A, 544, A22
Liszt, H. 2014, ApJ, 783, 17
Liszt, H. S., & Pety, J. 2012, A&A, 541, A58
Liszt, H. S., Pety, J., & Lucas, R. 2010, A&A, 518, A45
Magnani, L., Chastain, R. J., Kim, H. C., et al. 2003, ApJ, 586, 1111
Martin, P. G., Roy, A., Bontemps, S., et al. 2012, ApJ, 751, 28
McClure-Griffiths, N. M., Pisano, D. J., Calabretta, M. R., et al. 2009, ApJS, 181, 398
Mizuno, A., Yamaguchi, R., Tachihara, K., et al. 2001, PASJ, 53, 1071
Mohan, R., Dwarakanath, K. S., & Srinivasan, G. 2004, JA&A, 25, 185
Neyman, J., & Pearson, E. S. 1933, Phil. Trans. R. Soc. Lond. A, 231, 289
Nolan, P. L., Abdo, A. A., Ackermann, M., et al. 2012, ApJS, 199, 31
Padovani, M., & Galli, D. 2011, A&A, 530, A109
Paradis, D., Dobashi, K., Shimoikura, T., et al. 2012, A&A, 543, A103
Pineda, J. L., Goldsmith, P. F., Chapman, N., et al. 2010, ApJ, 721, 686
Pineda, J. L., Langer, W. D., Velusamy, T., & Goldsmith, P. F. 2013, A&A, 554, A103
Planck Collaboration XIX. 2011, A&A, 536, A19
Planck Collaboration XXI. 2011, A&A, 536, A21
Planck Collaboration XXIV. 2011, A&A, 536, A24
Planck Collaboration XI. 2014, A&A, 571, A11
Planck Collaboration XIII. 2014, A&A, 571, A13
Planck Collaboration Int. XVII. 2014, A&A, 566, A55
Planck Collaboration Int. XXIX. 2015, A&A, submited [arXiv:1409.2495]
Rachford, B. L., Snow, T. P., Destree, J. D., et al. 2009, ApJS, 180, 125
Reach, W. T., Koo, B.-C., & Heiles, C. 1994, ApJ, 429, 672
Reach, W. T., Wall, W. F., & Odegard, N. 1998, ApJ, 507, 507
Rowles, J., & Froebrich, D. 2009, MNRAS, 395, 1640
Roy, A., Martin, P. G., Polychroni, D., et al. 2013, ApJ, 763, 55
Sandstrom, K. M., Leroy, A. K., Walter, F., et al. 2013, ApJ, 777, 5
Schlafly, E. F., Green, G., Finkbeiner, D. P., et al. 2014, ApJ, 786, 29
Schlegel, D. J., Finkbeiner, D. P., & Davis, M. 1998, ApJ, 500, 525
Sheffer, Y., Rogers, M., Federman, S. R., et al. 2008, ApJ, 687, 1075
Skilling, J., & Strong, A. W. 1976, A&A, 53, 25
Skrutskie, M. F., Cutri, R. M., Stiening, R., et al. 2006, AJ, 131, 1163
Sodroski, T. J., Odegard, N., Arendt, R. G., et al. 1997, ApJ, 480, 173
Starck, J.-L., & Pierre, M. 1998, A&AS, 128, 397
Stepnik, B., Abergel, A., Bernard, J.-P., et al. 2003, A&A, 398, 551
Strong, A. W. 1985, A&A, 150, 273
Strong, A. W., Bloemen, J. B. G. M., Dame, T. M., et al. 1988, A&A, 207, 1
Strong, A. W., Moskalenko, I. V., & Reimer, O. 2004, ApJ, 613, 962
Su, M., Slatyer, T. R., & Finkbeiner, D. P. 2010, ApJ, 724, 1044
van Dishoeck, E. F., & Black, J. H. 1988, ApJ, 334, 771
Wolfire, M. G., Hollenbach, D., & McKee, C. F. 2010, ApJ, 716, 1191
Ysard, N., Juvela, M., Demyk, K., et al. 2012, A&A, 542, A21
Ysard, N., Abergel, A., Ristorcelli, I., et al. 2013, A&A, 559, A133

[1] APC, AstroParticule et Cosmologie, Université Paris Diderot, CNRS/IN2P3, CEA/lrfu, Observatoire de Paris, Sorbonne Paris Cité, 10 rue Alice Domon et Léonie Duquet, 75205 Paris Cedex 13, France
[2] African Institute for Mathematical Sciences, 6−8 Melrose Road, Muizenberg, 7950 Cape Town, South Africa
[3] Agenzia Spaziale Italiana Science Data Center, via del Politecnico snc, 00133 Roma, Italy
[4] Agenzia Spaziale Italiana, Viale Liegi 26, 00186 Roma, Italy
[5] Astrophysics Group, Cavendish Laboratory, University of Cambridge, J J Thomson Avenue, Cambridge CB3 0HE, UK
[6] Astrophysics & Cosmology Research Unit, School of Mathematics, Statistics & Computer Science, University of KwaZulu-Natal, Westville Campus, Private Bag X54001, Durban 4000, South Africa
[7] Atacama Large Millimeter/submillimeter Array, ALMA Santiago Central Offices, Alonso de Cordova 3107, Vitacura, Casilla 763 0355 Santiago, Chile
[8] CITA, University of Toronto, 60 St. George St., Toronto, ON M5S 3H8, Canada
[9] CNRS, IRAP, 9 Av. colonel Roche, BP 44346, 31028 Toulouse Cedex 4, France
[10] California Institute of Technology, Pasadena, A 91125 California, USA
[11] Centro de Estudios de Física del Cosmos de Aragón (CEFCA), Plaza San Juan, 1, planta 2, 44001 Teruel, Spain
[12] Computational Cosmology Center, Lawrence Berkeley National Laboratory, Berkeley, CA94720 California, USA
[13] Consejo Superior de Investigaciones Científicas (CSIC), 117 Madrid, Spain
[14] DSM/Irfu/SPP, CEA-Saclay, 91191 Gif-sur-Yvette Cedex, France
[15] DTU Space, National Space Institute, Technical University of Denmark, Elektrovej 327, 2800 Kgs. Lyngby, Denmark
[16] Département de Physique Théorique, Université de Genève, 24 Quai E. Ansermet, 1211 Genève 4, Switzerland
[17] Departamento de Física, Universidad de Oviedo, Avda. Calvo Sotelo s/n, 33003 Oviedo, Spain
[18] Department of Astrophysics/IMAPP, Radboud University Nijmegen, PO Box 9010, 6500 GL Nijmegen, The Netherlands
[19] Department of Physics & Astronomy, University of British Columbia, 6224 Agricultural Road, Vancouver, BC V6T 1Z1 British Columbia, Canada
[20] Department of Physics and Astronomy, Dana and David Dornsife College of Letter, Arts and Sciences, University of Southern California, Los Angeles, CA 90089, USA
[21] Department of Physics and Astronomy, University College London, London WC1E 6BT, UK
[22] Department of Physics, Florida State University, Keen Physics Building, 77 Chieftan Way, Tallahassee, FL32306 Florida, USA
[23] Department of Physics, Gustaf Hällströmin katu 2a, University of Helsinki, 00014 Helsinki, Finland
[24] Department of Physics, Nagoya University, Chikusa-ku, 464-8602, Nagoya, Japan
[25] Department of Physics, Princeton University, Princeton, New Jersey, NJ 08544 USA
[26] Department of Physics, University of California, Santa Barbara, California CA93106, USA
[27] Department of Physics, University of Illinois at Urbana-Champaign, 1110 West Green Street, Urbana, Illinois, Il 61801 USA
[28] Dipartimento di Fisica e Astronomia G. Galilei, Università degli Studi di Padova, via Marzolo 8, 35131 Padova, Italy
[29] Dipartimento di Fisica e Scienze della Terra, Università di Ferrara, via Saragat 1, 44122 Ferrara, Italy
[30] Dipartimento di Fisica, Università La Sapienza, P.le A. Moro 2, 00185 Roma, Italy

[31] Dipartimento di Fisica, Università degli Studi di Milano, via Celoria, 16, 20122 Milano, Italy
[32] Dipartimento di Fisica, Università degli Studi di Trieste, via A. Valerio 2, 34128 Trieste, Italy
[33] Dipartimento di Fisica, Università di Roma Tor Vergata, via della Ricerca Scientifica, 1 00133 Roma, Italy
[34] Discovery Center, Niels Bohr Institute, 17 Blegdamsvej, 2100 Copenhagen, Denmark
[35] Dpto. Astrofísica, Universidad de La Laguna (ULL), 38206 La Laguna, Tenerife, Spain
[36] European Southern Observatory, ESO Vitacura, Alonso de Cordova 3107, Vitacura, Casilla 19001, Santiago, Chile
[37] European Space Agency, ESAC, Planck Science Office, Camino bajo del Castillo, s/n, Urbanización Villafranca del Castillo, 28692 Villanueva de la Cañada, Madrid, Spain
[38] European Space Agency, ESTEC, Keplerlaan 1, 2201 AZ Noordwijk, The Netherlands
[39] Facoltà di Ingegneria, Università degli Studi e-Campus, via Isimbardi 10, 22060 Novedrate (CO), Italy
[40] HGSFP and University of Heidelberg, Theoretical Physics Department, Philosophenweg 16, 69120 Heidelberg, Germany
[41] Helsinki Institute of Physics, Gustaf Hällströmin katu 2, University of Helsinki, 00100 Helsinki, Finland
[42] INAF−Osservatorio Astrofisico di Catania, via S. Sofia 78, 95123 Catania, Italy
[43] INAF−Osservatorio Astronomico di Padova, Vicolo dell'Osservatorio 5, 35122 Padova, Italy
[44] INAF−Osservatorio Astronomico di Roma, via di Frascati 33, 00040 Monte Porzio Catone, Italy
[45] INAF−Osservatorio Astronomico di Trieste, via G.B. Tiepolo 11, 34131 Trieste, Italy
[46] INAF/IASF Bologna, via Gobetti 101, 40127 Bologna, Italy
[47] INAF/IASF Milano, via E. Bassini 15, 20133 Milano, Italy
[48] INFN, Sezione di Bologna, via Irnerio 46, 40126 Bologna, Italy
[49] INFN, Sezione di Roma 1, Università di Roma Sapienza, Piazzale Aldo Moro 2, 00185 Roma, Italy
[50] INFN/National Institute for Nuclear Physics, via Valerio 2, 34127 Trieste, Italy
[51] IPAG: Institut de Planétologie et d'Astrophysique de Grenoble, Université Grenoble Alpes, IPAG, 38000 Grenoble, CNRS, France, IPAG, 38000 Grenoble, France
[52] Imperial College London, Astrophysics group, Blackett Laboratory, Prince Consort Road, London, SW7 2AZ, UK
[53] Infrared Processing and Analysis Center, California Institute of Technology, Pasadena, CA 91125, USA
[54] Institut Universitaire de France, 103 Bd Saint-Michel, 75005 Paris, France
[55] Institut d'Astrophysique Spatiale, CNRS (UMR8617) Université Paris-Sud 11, Bâtiment 121, 91405 Orsay, France
[56] Institut d'Astrophysique de Paris, CNRS (UMR7095), 98bis Boulevard Arago, 75014 Paris, France
[57] Institute for Space Sciences, 077125 Bucharest-Magurale, Romania
[58] Institute of Astronomy, University of Cambridge, Madingley Road, Cambridge CB3 0HA, UK
[59] Institute of Theoretical Astrophysics, University of Oslo, 1029 Blindern, Oslo, Norway
[60] Instituto de Astrofísica de Canarias, C/vía Láctea s/n, La Laguna, 38205 Tenerife, Spain
[61] Instituto de Física de Cantabria (CSIC-Universidad de Cantabria), Avda. de los Castros s/n, 39005 Santander, Spain
[62] Jet Propulsion Laboratory, California Institute of Technology, 4800 Oak Grove Drive, Pasadena, CA91109 California, USA
[63] Jodrell Bank Centre for Astrophysics, Alan Turing Building, School of Physics and Astronomy, The University of Manchester, Oxford Road, Manchester, M13 9PL, UK
[64] Kavli Institute for Cosmology Cambridge, Madingley Road, Cambridge, CB3 0HA, UK
[65] LAL, Université Paris-Sud, CNRS/IN2P3, 91400 Orsay, France
[66] LERMA, CNRS, Observatoire de Paris, 61 Avenue de l'Observatoire, 75014 Paris, France
[67] Laboratoire AIM, IRFU/Service d'Astrophysique – CEA/DSM – CNRS – Université Paris Diderot, Bât. 709, CEA-Saclay, 91191 Gif-sur-Yvette Cedex, France
[68] Laboratoire Traitement et Communication de l'Information, CNRS (UMR 5141) and Télécom ParisTech, 46 rue Barrault 75634 Paris Cedex 13, France
[69] Laboratoire de Physique Subatomique et de Cosmologie, Université Joseph Fourier Grenoble I, CNRS/IN2P3, Institut National Polytechnique de Grenoble, 53 rue des Martyrs, 38026 Grenoble Cedex, France
[70] Laboratoire de Physique Théorique, Université Paris-Sud 11 & CNRS, Bâtiment 210, 91405 Orsay, France
[71] Lawrence Berkeley National Laboratory, Berkeley, California, USA
[72] Max-Planck-Institut für Astrophysik, Karl-Schwarzschild-Str. 1, 85741 Garching, Germany
[73] Max-Planck-Institut für Extraterrestrische Physik, Giessenbachstraße, 85748 Garching, Germany
[74] McGill Physics, Ernest Rutherford Physics Building, McGill University, 3600 rue University, Montréal, QC, H3A 2T8, Canada
[75] National University of Ireland, Department of Experimental Physics, Maynooth, Co. Kildare, Ireland
[76] Niels Bohr Institute, Blegdamsvej 17, 2100 Copenhagen, Denmark
[77] Observational Cosmology, Mail Stop 367-17, California Institute of Technology, Pasadena, CA, 91125, USA
[78] SISSA, Astrophysics Sector, via Bonomea 265, 34136 Trieste, Italy
[79] School of Physics and Astronomy, Cardiff University, Queens Buildings, The Parade, Cardiff, CF24 3AA, UK
[80] Space Research Institute (IKI), Russian Academy of Sciences, Profsoyuznaya Str, 84/32, 117997 Moscow, Russia
[81] Space Sciences Laboratory, University of California, Berkeley, California 94720, USA
[82] Special Astrophysical Observatory, Russian Academy of Sciences, Nizhnij Arkhyz, Zelenchukskiy region, 369167 Karachai-Cherkessian Republic, Russia
[83] Sub-Department of Astrophysics, University of Oxford, Keble Road, Oxford OX1 3RH, UK
[84] UPMC Univ. Paris 06, UMR7095, 98bis boulevard Arago, 75014 Paris, France
[85] Université de Toulouse, UPS-OMP, IRAP, 31028 Toulouse Cedex 4, France
[86] Universities Space Research Association, Stratospheric Observatory for Infrared Astronomy, MS 232-11, Moffett Field, CA 94035, USA
[87] University of Granada, Departamento de Física Teórica y del Cosmos, Facultad de Ciencias, 18071 Granada, Spain
[88] University of Granada, Instituto Carlos I de Física Teórica y Computacional, 18071 Granada, Spain
[89] W. W. Hansen Experimental Physics Laboratory, Kavli Institute for Particle Astrophysics and Cosmology, Department of Physics and SLAC National Accelerator Laboratory, Stanford University, Stanford, CA 94305, USA
[90] Warsaw University Observatory, Aleje Ujazdowskie 4, 00-478 Warszawa, Poland

Pages 28 to 32 are available in the electronic edition of the journal at http://www.aanda.org

Appendix A: H I component separation

We have developed a careful kinematical separation of the four H I structures present within the analysis region, namely:

- the H I gas associated with the star-forming CO clouds of the Chamaeleon complex at velocities between about −4 and +15 km s^{-1};
- the gas in an intermediate velocity arc (IVA), crossing the whole region around −25° in latitude, at negative velocities down to −40 km s^{-1};
- the background H I lying at high altitude above the Galactic disc, at velocities below about +170 km s^{-1};
- gas in the LMC and its tidal tails at the highest velocities.

These components are visible in Fig. A.1.

Because of the broad widths of H I lines, the procedure aims to correct the velocity spillover from one component to the next in the column-density derivation. To do so for each direction in the sky, we have: detected all significant lines in the measured H I spectrum; fitted them with pseudo-Voigt profiles; used the line centroids in velocity to distribute the lines between the components; and integrated each line profile to add its contribution to the column-density map of the relevant component.

The core of the method is based on fitting every spectrum in brightness temperature, $T_B(v)$, with a sum of lines across the whole $-164.1 \leq v \leq 409$ km s^{-1} velocity interval exhibiting significant line emission. The first step is to find the number and approximate velocity of the lines to be fitted. For each (l, b) pixel direction, we have smoothed the spectrum in velocity with a Gaussian kernel of 1.48 km s^{-1}. We have measured the rms dispersion in temperature, T_{rms}, outside the bands with significant emission. We have clipped the data to zero outside regions with $T(v) > T_{rms}$ in 3 adjacent channels. The clipping limits the number of fake line detections triggered by strong noise fluctuations in bands devoid of emission. We have then computed the curvature d^2T_B/dv^2 in each channel by using the 5-point-Lagrangian differentiation twice. We have detected the line peaks and shoulders by finding the negative minima in d^2T_B/dv^2. We have eliminated peak detections caused by the edges of the clipped bands. An average line FWHM of 8.2 km s^{-1} was found in the line fits. We have merged potential lines when separated by less than one half width at half maximum (HWHM) in velocity. Weak lines ($T_{peak} < 3$ K) were also merged when closer than one FWHM in order to limit the number of fake detections on noise fluctuations in faint line wings. When merging lines, the new velocity centroid was set to the average between the parent velocities. The final number of detected peaks and shoulders and their velocities have been used as input parameters for fitting multiple lines across the spectrum.

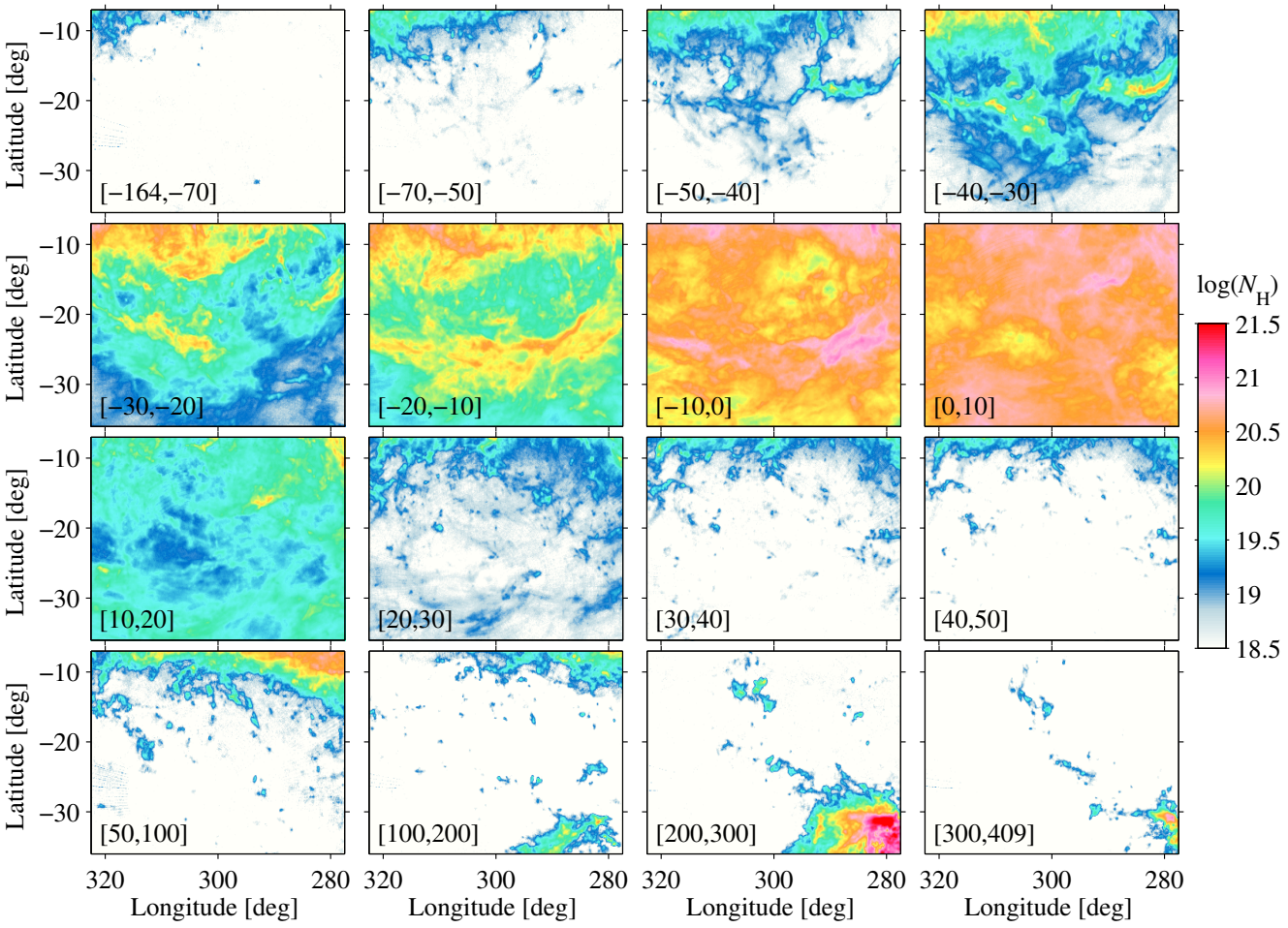

Fig. A.1. Maps of the N_{HI} column densities (in cm^{-2}) obtained at 14.′5, resolution from the GASS survey for optically thin emission and integrated over contiguous velocity intervals between the values given in km s^{-1} on the lower left corner of each map.

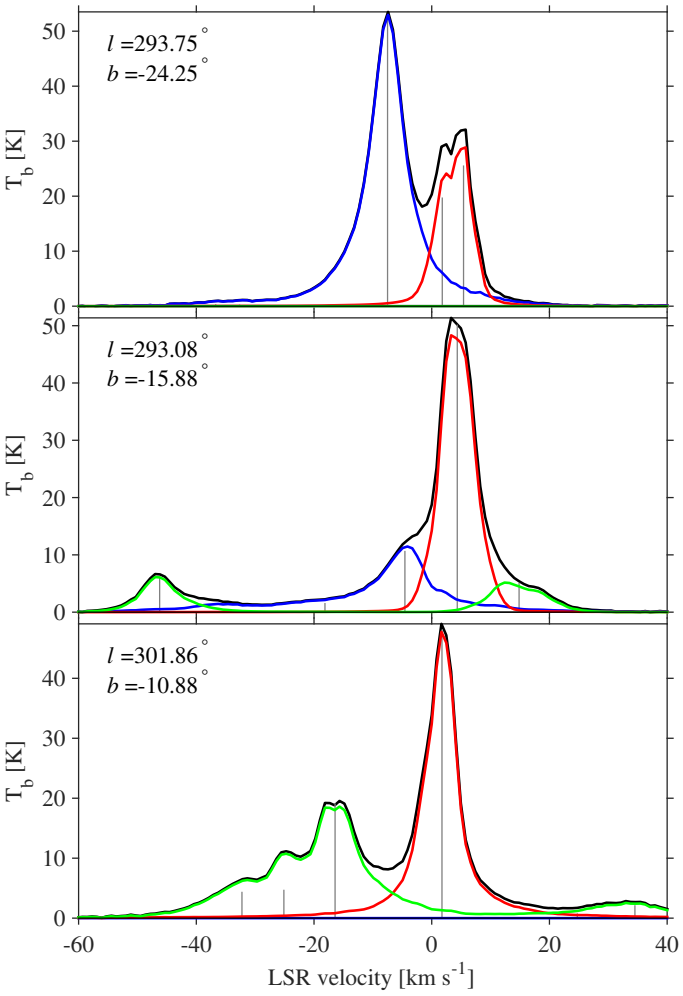

Fig. A.2. H I GASS spectra, in brightness temperature, measured toward the three directions indicated on the plots. The best line fits attributed to the local (red), IVA (blue), and Galactic (green) components sum up as the black curve, which closely follows the original data. The grey lines indicate the central velocity and temperature of the individual lines that contribute to a component.

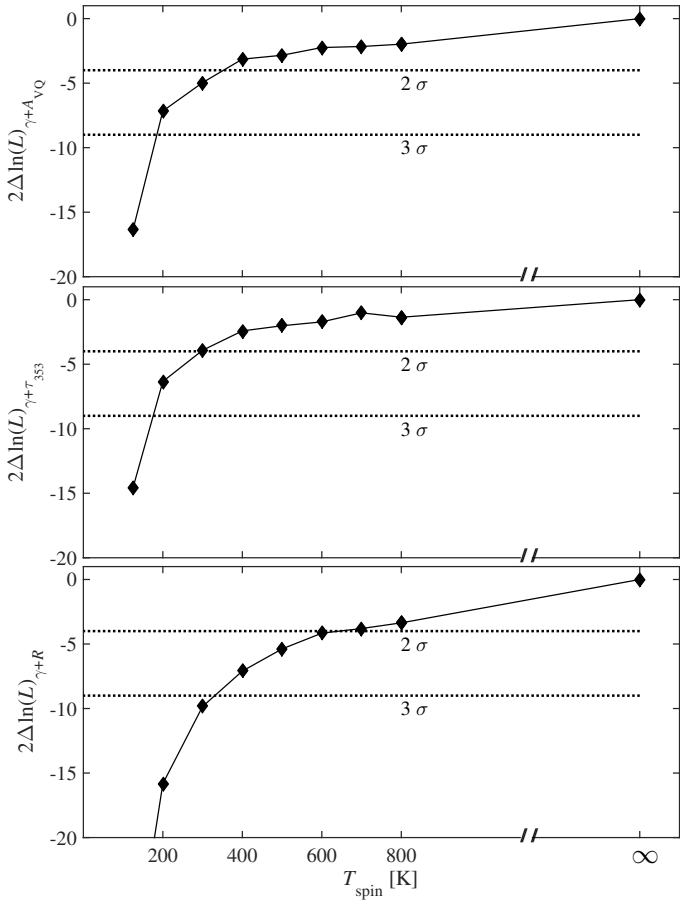

Fig. B.1. Evolution of the log-likelihood ratios of the γ-ray fits with the H I spin temperature, using the four independent energy bands in the γ+A_{VQ} (*top*), γ+τ_{353} (*middle*), and γ+R (*bottom*) analyses.

We have fitted each spectrum with a sum of pseudo-Voigt line profiles, one for each detected peak or shoulder. Such a profile combines a Gaussian and a Lorentzian with the same velocity centroid, width, and height, and a relative weight that spans the interval from 0 (pure Gaussian) to 1 (pure Lorentzian). The velocity centroid was allowed to move within $\pm 3.3\,\mathrm{km\,s^{-1}}$ (± 4 channels) around the original peak velocity. We have manually checked the precision of many fits across the region. All fits were checked to yield a total line intensity to better than 80–90% of the data integral over the whole spectrum.

In order to preserve the total H I intensity observed in each direction, the small residuals (positive and negative) between the observed and modelled spectra have been distributed between the lines in proportion to the height of each line at each velocity. The line profiles have been corrected accordingly and integrated for a given choice of spin temperature to correct the resulting column-density for the H I optical depth.

Each line was attributed to one of the four components according to its velocity centroid in the (l, b) direction. The spatial separation between the IVA and Galactic disc components runs along a broken line of minimum intensity starting at $b = -12°$ at low longitude, reaching $b = -18.^{\circ}5$ at $l = 300°$, and moving up to $b \simeq -16°$ at the highest longitude; the frontier can be seen in Fig. 2. Lines pertaining to the local Chamaeleon clouds were selected at $-4\,\mathrm{km\,s^{-1}} \leq v < 14.8\,\mathrm{km\,s^{-1}}$ for latitudes below this curve, and at $-7.4\,\mathrm{km\,s^{-1}} \leq v < 14.8\,\mathrm{km\,s^{-1}}$ above the border. The lines of the IVA cloud were selected in the $-40\,\mathrm{km\,s^{-1}} \leq v < -4\,\mathrm{km\,s^{-1}}$ interval at latitudes below the curve. The latitude cut between the Galactic disc and LMC components runs linearly from $(l, b) = (273.^{\circ}4, -13.^{\circ}75)$ to $(326.^{\circ}6, -8.^{\circ}5)$. The LMC lines were selected at $v \geq 131.9\,\mathrm{km\,s^{-1}}$ below the latitude cut and at $v \geq 174\,\mathrm{km\,s^{-1}}$ for all latitudes. The rest of the data was attributed to the Galactic disc component. A selection of spectra is given in Fig. A.2 to illustrate the separation of the local, IVA, and Galactic components.

We have summed the column densities derived for each line associated with a component to produce the maps of Fig. 2. We have tested different velocity cuts around $-4\,\mathrm{km\,s^{-1}}$ between the local and IVA clouds. A change of 1 or $2\,\mathrm{km\,s^{-1}}$ changes the related maps by 3 to 6% in total mass, mostly in the overlap region near $l = 283°$ and $b = -25°$. The overall structure and contrast in each map, which drive the correlation studies, remain largely unchanged.

Appendix B: H I spin temperature

For all analyses and for each energy band, we have found that the maximum likelihood value of the γ-ray fit increases with decreasing H I opacity, thus with increasing spin temperature.

Table C.1. Linear regression parameters and correlation coefficients between the W_{CO} intensities measured with NANTEN, CfA, and *Planck*.

y-axis	*x*-axis	Slope	Intercept	Corr. coeff.
NANTEN	CfA	1.015 ± 0.008	0.92 ± 0.06	0.95
NANTEN	*Planck* CO "Type 3"	0.951 ± 0.002	0.12 ± 0.01	0.97
Planck CO "Type 1"	CfA	0.96 ± 0.02	2.54 ± 0.18	0.74
CfA	*Planck* CO "Type 3"	0.747 ± 0.006	0.96 ± 0.06	0.94

The data in each band being independent, one can sum the log-likelihoods of each fit to constrain the spin temperature. Figure B.1 indicates that uniform temperatures of $T_S > 340$ K, >300 K, and >640 K are preferred at the 2σ confidence levels for the γ+A_{VQ}, γ+τ_{353}, and γ+R analyses, respectively. The maximum in brightness temperature in the whole data cube is 152 K. This indicates that optically thin conditions largely prevail across the whole velocity range.

In view of these results and with the added arguments that the CR spectrum inside the three H I structures is close to the local one and that the γ-ray intensities have been shown to scale linearly with N_{HI} to higher, less transparent, column densities in more massive clouds (Ackermann et al. 2012b), so that γ rays apparently trace all the H I gas, we follow the γ-ray results and consider the optically thin H I case as that which best represents the data.

Appendix C: CO calibration checks

Checks on the NANTEN data cube have revealed several artefacts that we have corrected before integrating the spectra to obtain the W_{CO} intensities given in Fig. 2. We have removed significant negative lines, probably caused by the presence of a line in the off band in frequency-switching. High-order polynomial residuals were also present in the baseline profiles outside the main CO lines. They did not average out to zero in the W_{CO} map, so we have filtered them from the regions void of significant CO intensity. Moment-masking is commonly used to clean H I and W_{CO} maps (Dame 2011). It was not applicable here because the residuals, unlike noise, extended over several contiguous channels. We have filtered the original W_{CO} map using the multiresolution support method implemented in the `MR filter` software (Starck & Pierre 1998), with seven scales in the bspline-wavelet transform (à trous algorithm). For the Gaussian noise of W_{CO}, denoising with a hard 4σ threshold led to robust results. The final map shown in Fig. 2 is composed of the original, unfiltered, W_{CO} intensity where the filtered one exceeded 1 K km s^{-1}, and of the filtered intensity outside these faint edges. Particular attention was paid to preserve the faint cloud edges which hold a fair fraction of the cloud mass because of their large volume.

Figure C.1 illustrates the correlations found between the W_{CO} intensities measured over the region with NANTEN (after the corrections described above), with CfA from the moment-masked, fully sampled observations of the Chamaeleon complex (Boulanger et al. 1998), and with *Planck* (Planck Collaboration XIII 2014). It shows that the data from the *Planck* `TYPE 1` map is too noisy for our purpose. The other data sets show tight correlations. The correlation coefficients and the slope and intercept of the regression lines are given in Table C.1. They indicate that the *Planck* `TYPE 3` method systematically

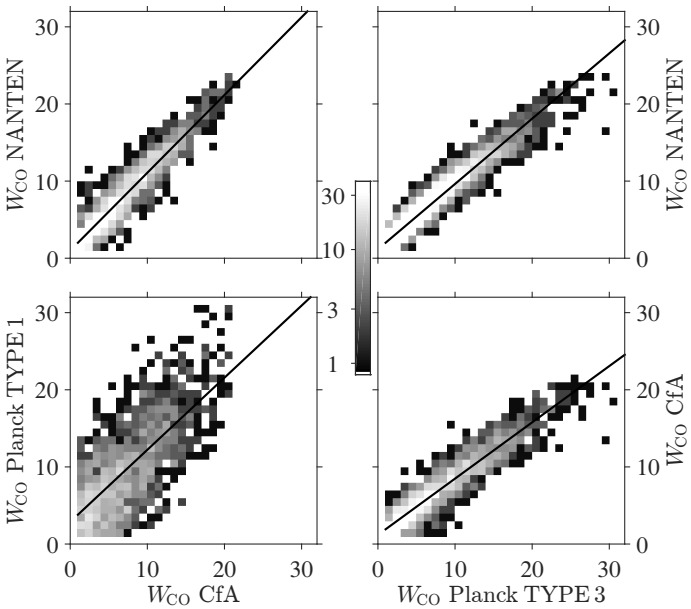

Fig. C.1. Correlations and linear regressions between the NANTEN, CfA, and *Planck* `TYPE 3` and `TYPE 1` W_{CO} intensities in the analysis region. The data are sampled at 0.°125 and the intensities are given in K km s^{-1}. The best-fit slopes are given in Table C.1

overpredicts the intensities in this region compared to the consistent yield of both radio telescopes. An earlier comparison of the NANTEN and CfA surveys across the sky had found 24% larger intensities on average in the NANTEN maps (Planck Collaboration XIX 2011). Figure C.1 shows that the NANTEN and CfA photometries fully agree in the Chamaeleon region. The data are consistent with a unit slope over the whole intensity range. The intercept is compatible with the sensitivity of the NANTEN observations, which varies between 1.5 and 2 K km s^{-1} across the region.

Appendix D: independent γ-ray and dust fits without DNM templates

In order to check for the presence of substantial amounts of gas not traced by the H I and CO line intensities in the independent γ-ray and dust data sets, we have fitted the γ-ray and dust data with models that do not include a DNM template. All the other components described in Sects. 3.2 and 3.3 have been kept free. The resulting best fits are of significantly lower quality than those obtained with models including the DNM (see Sect. 4). The residual maps, however, are interesting in that they exhibit

comparable regions of positive residuals in the independent dust and γ-ray data, as shown in Fig. D.1.

We also note that, in the absence of a DNM template, the best fits yield systematically larger contributions from the H I and CO components than in models that include the DNM. These components, in particular the CO one, are amplified to partially compensate for the missing gas structure. We find 4−13% larger γ-ray emissivities for the local H I and IVA components, and 22% to 57% larger CO γ-ray emissivities. The dust fits respond the same way, with 7−12% larger A_{VQ}/N_H, 9−15% larger opacities and 4−7% larger specific powers for the local H I and IVA components, and 25% to 40% larger CO contributions. As a consequence, the best-fit models often over-predict the data toward the CO clouds (see the negative residuals toward Cha II+III and Cha East I and II in Fig. D.1). These results prompted us to iterate the construction of DNM templates between the γ-ray and dust analyses in order to reduce the DNM bias on the determination of the H I and CO parameters.

Appendix E: Best-fit interstellar coefficients

See Table E.1.

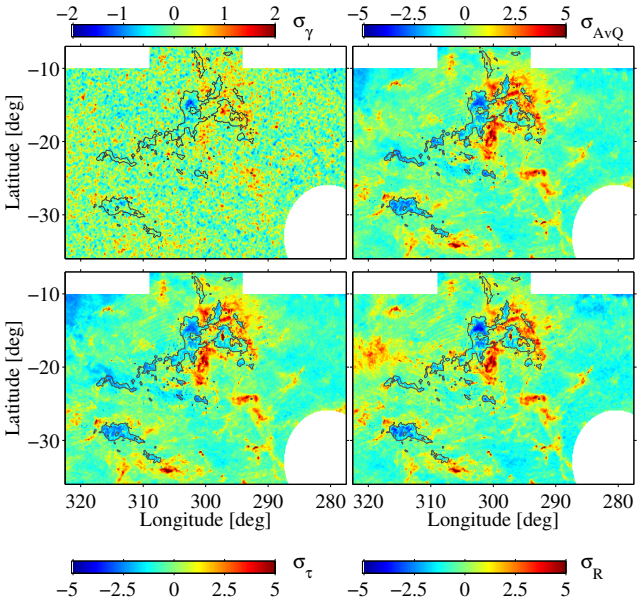

Fig. D.1. Maps of residuals (data minus best-fit model, in sigma units) obtained when fitting the γ-ray, A_{VQ}, R, or τ_{353} data (clockwise) with optically thin H I and W_{CO}, but no DNM. In all plots, the grey contours outline the shape of the CO clouds at the 2.3 K km s^{-1} level.

Table E.1. Best-fit coefficients of the γ-ray models (q for each energy band) and of the dust models (y) for the γ+A_{VQ} (*top*), γ+τ_{353} (*middle*), and γ+R (*bottom*) analyses.

Energy band	$q_{\rm HI\,Cha}$	$q_{\rm HI\,IVA}$	$q_{\rm HI\,Gal}$	$q_{\rm CO}{}^{a}$	$q_{\rm DNM}{}^{b1}$	$q_{\rm IC}$	$q_{\rm iso}$
$10^{2.6}$–$10^{2.8}$ MeV	$1.34 \pm 0.07^{+0}_{-0.09}$	$1.22 \pm 0.06^{+0}_{-0.04}$	$1.17 \pm 0.08^{+0}_{-0.03}$	$2.01 \pm 0.12^{+0}_{-0.03}$	$20.9 \pm 1.3^{+0.5}_{-0}$	$1.32 \pm 0.13^{+0.01}_{-0}$	$0.8 \pm 0.2^{+0.1}_{-0}$
$10^{2.8}$–$10^{3.2}$ MeV	$1.42 \pm 0.06^{+0}_{-0.06}$	$1.16 \pm 0.05^{+0}_{-0.04}$	$1.20 \pm 0.07^{+0}_{-0.03}$	$1.762 \pm 0.112^{+0.006}_{-0}$	$19.8 \pm 1.0^{+0}_{-0.2}$	$1.44 \pm 0.13^{+0}_{-0.01}$	$0.6 \pm 0.3^{+0.1}_{-0}$
$10^{3.2}$–$10^{3.6}$ MeV	$1.34 \pm 0.07^{+0}_{-0.07}$	$1.17 \pm 0.06^{+0}_{-0.04}$	$1.38 \pm 0.08^{+0}_{-0.04}$	$2.027 \pm 0.102^{+0}_{-0.009}$	$18.27 \pm 1.12^{+0.08}_{-0}$	$1.285 \pm 0.151^{+0.006}_{-0}$	$1.13 \pm 0.32^{+0.10}_{-0}$
$10^{3.6}$–$10^{5.0}$ MeV	$1.64 \pm 0.13^{+0}_{-0.07}$	$1.43 \pm 0.11^{+0}_{-0.05}$	$1.29 \pm 0.17^{+0}_{-0.03}$	$2.065 \pm 0.176^{+0}_{-0.001}$	$22.31 \pm 2.12^{+0.07}_{-0}$	$1.25 \pm 0.20^{+0}_{-0.03}$	$0.53 \pm 0.28^{+0.06}_{-0}$
$10^{2.6}$–$10^{5.0}$ MeV	$1.38 \pm 0.04^{+0}_{-0.05}$	$1.20 \pm 0.03^{+0}_{-0.04}$	$1.25 \pm 0.04^{+0}_{-0.04}$	$1.921 \pm 0.072^{+0}_{-0.010}$	$19.99 \pm 0.67^{+0.02}_{-0}$	$1.33 \pm 0.08^{+0.01}_{-0}$	$0.83 \pm 0.15^{+0.05}_{-0}$
	$y_{\rm HI\,Cha}{}^{c1}$	$y_{\rm HI\,IVA}{}^{c1}$	$y_{\rm HI\,Gal}{}^{c1}$	$y_{\rm CO}{}^{d1}$	$y_{\rm DNM}{}^{c1}$		$y_{\rm iso}{}^{e1}$
	$8.11 \pm 0.09^{+0}_{-0.37}$	$7.31 \pm 0.07^{+0}_{-0.26}$	$7.41 \pm 0.09^{+0}_{-0.22}$	$16.38 \pm 0.34^{+0}_{-0.04}$	$7.1 \pm 0.2^{+0}_{-0.4}$		$-16.4 \pm 0.5^{+1.2}_{-0}$
Energy band	$q_{\rm HI\,Cha}$	$q_{\rm HI\,IVA}$	$q_{\rm HI\,Gal}$	$q_{\rm CO}{}^{a}$	$q_{\rm DNM}{}^{b2}$	$q_{\rm IC}$	$q_{\rm iso}$
$10^{2.6}$–$10^{2.8}$ MeV	$1.36 \pm 0.07^{+0}_{-0.06}$	$1.22 \pm 0.06^{+0}_{-0.04}$	$1.05 \pm 0.08^{+0}_{-0.04}$	$1.91 \pm 0.13^{+0}_{-0.02}$	$8.88 \pm 0.59^{+0.06}_{-0}$	$1.54 \pm 0.13^{+0.03}_{-0}$	$0.63 \pm 0.23^{+0.05}_{-0}$
$10^{2.8}$–$10^{3.2}$ MeV	$1.45 \pm 0.06^{+0}_{-0.04}$	$1.17 \pm 0.05^{+0}_{-0.03}$	$1.09 \pm 0.07^{+0}_{-0.03}$	$1.695 \pm 0.121^{+0}_{-0.007}$	$8.23 \pm 0.43^{+0}_{-0.03}$	$1.69 \pm 0.13^{+0}_{-0.01}$	$0.28 \pm 0.27^{+0.07}_{-0}$
$10^{3.2}$–$10^{3.6}$ MeV	$1.37 \pm 0.07^{+0}_{-0.07}$	$1.19 \pm 0.06^{+0}_{-0.05}$	$1.27 \pm 0.09^{+0}_{-0.02}$	$1.977 \pm 0.106^{+0}_{-0.004}$	$7.50 \pm 0.51^{+0}_{-0.02}$	$1.498 \pm 0.150^{+0}_{-0.008}$	$0.8 \pm 0.3^{+0.2}_{-0}$
$10^{3.6}$–$10^{5.0}$ MeV	$1.70 \pm 0.13^{+0}_{-0.09}$	$1.45 \pm 0.11^{+0}_{-0.04}$	$1.16 \pm 0.17^{+0}_{-0.03}$	$2.021 \pm 0.180^{+0}_{-0.004}$	$8.97 \pm 0.93^{+0.02}_{-0}$	$1.388 \pm 0.200^{+0.010}_{-0}$	$0.37 \pm 0.28^{+0.07}_{-0}$
$10^{2.6}$–$10^{5.0}$ MeV	$1.42 \pm 0.04^{+0}_{-0.06}$	$1.21 \pm 0.03^{+0}_{-0.04}$	$1.13 \pm 0.05^{+0}_{-0.04}$	$1.87 \pm 0.08^{+0}_{-0.02}$	$8.20 \pm 0.33^{+0.09}_{-0}$	$1.556 \pm 0.080^{+0.006}_{-0}$	$0.52 \pm 0.15^{+0.09}_{-0}$
	$y_{\rm HI\,Cha}{}^{c2}$	$y_{\rm HI\,IVA}{}^{c2}$	$y_{\rm HI\,Gal}{}^{c2}$	$y_{\rm CO}{}^{d2}$	$y_{\rm DNM}{}^{c2}$		$y_{\rm iso}{}^{e2}$
	$1.63 \pm 0.02^{+0}_{-0.06}$	$1.48 \pm 0.02^{+0}_{-0.04}$	$1.24 \pm 0.02^{+0}_{-0.04}$	$4.130 \pm 0.102^{+0.002}_{-0}$	$1.73 \pm 0.05^{+0}_{-0.09}$		$-4.0 \pm 0.1^{+0.2}_{-0}$
Energy band	$q_{\rm HI\,Cha}$	$q_{\rm HI\,IVA}$	$q_{\rm HI\,Gal}$	$q_{\rm CO}{}^{a}$	$q_{\rm DNM}{}^{b3}$	$q_{\rm IC}$	$q_{\rm iso}$
$10^{2.6}$–$10^{2.8}$ MeV	$1.31 \pm 0.08^{+0}_{-0.01}$	$1.20 \pm 0.06^{+0}_{-0.06}$	$1.55 \pm 0.08^{+0}_{-0.03}$	$2.33 \pm 0.12^{+0}_{-0.01}$	$5.73 \pm 0.38^{+0}_{-0.06}$	$0.59 \pm 0.14^{+0.09}_{-0}$	$1.45 \pm 0.24^{+0}_{-0.05}$
$10^{2.8}$–$10^{3.2}$ MeV	$1.40 \pm 0.06^{+0}_{-0.17}$	$1.13 \pm 0.05^{+0}_{-0.06}$	$1.59 \pm 0.07^{+0.07}_{-0}$	$2.045 \pm 0.108^{+0.003}_{-0}$	$5.5 \pm 0.3^{+0.3}_{-0}$	$0.6 \pm 0.1^{+0}_{-0.2}$	$1.6 \pm 0.3^{+0.8}_{-0}$
$10^{3.2}$–$10^{3.6}$ MeV	$1.35 \pm 0.07^{+0}_{-0.05}$	$1.15 \pm 0.06^{+0}_{-0.07}$	$1.73 \pm 0.09^{+0}_{-0.12}$	$2.25 \pm 0.10^{+0}_{-0.02}$	$5.0 \pm 0.3^{+0}_{-0.1}$	$0.6 \pm 0.2^{+0.1}_{-0}$	$1.81 \pm 0.32^{+0.08}_{-0}$
$10^{3.6}$–$10^{5.0}$ MeV	$1.7 \pm 0.1^{+0}_{-0.2}$	$1.42 \pm 0.11^{+0}_{-0.06}$	$1.75 \pm 0.18^{+0}_{-0.01}$	$2.32 \pm 0.17^{+0}_{-0.02}$	$5.9 \pm 0.6^{+0}_{-0.2}$	$0.68 \pm 0.22^{+0}_{-0.06}$	$0.9 \pm 0.3^{+0.3}_{-0}$
$10^{2.6}$–$10^{5.0}$ MeV	$1.38 \pm 0.04^{+0}_{-0.10}$	$1.173 \pm 0.031^{+0}_{-0.001}$	$1.626 \pm 0.045^{+0.008}_{-0}$	$2.201 \pm 0.078^{+0.005}_{-0}$	$5.49 \pm 0.19^{+0.01}_{-0}$	$0.57 \pm 0.08^{+0.02}_{-0}$	$1.5 \pm 0.1^{+0.2}_{-0}$
	$y_{\rm HI\,Cha}{}^{c3}$	$y_{\rm HI\,IVA}{}^{c3}$	$y_{\rm HI\,Gal}{}^{c3}$	$y_{\rm CO}{}^{d3}$	$y_{\rm DNM}{}^{c3}$		$y_{\rm iso}{}^{e3}$
	$3.86 \pm 0.04^{+0}_{-0.05}$	$3.65 \pm 0.04^{+0}_{-0.04}$	$4.84 \pm 0.05^{+0}_{-0.07}$	$5.10 \pm 0.13^{+0}_{-0.02}$	$2.72 \pm 0.09^{+0}_{-0.01}$		$-4.7 \pm 0.3^{+0.2}_{-0}$

Notes. The first uncertainties are statistical, the second result from changes in H I spin temperature over the 2σ confidence interval from the optically thin case. The latter do not include the 8% systematic uncertainty in the LAT sensitive area for the q parameters. Model uncertainties have been used to optimize the dust fits. $^{(a)}$ In 10^{20} cm^{-2} K^{-1} km^{-1} s, $^{(b1)}$ In 10^{20} cm^{-2} mag^{-1}, $^{(b2)}$ In 10^{25} cm^{-2}, $^{(b3)}$ In 10^{31} sr W^{-1}, $^{(c1)}$ In 10^{-22} mag cm^{2}, $^{(c2)}$ In 10^{-26} cm^{2}, $^{(c3)}$ In 10^{-32} W sr^{-1}, $^{(d1)}$ In 10^{-2} mag K^{-1} km^{-1} s, $^{(d2)}$ In 10^{-6} K^{-1} km^{-1} s, $^{(d3)}$ In 10^{-8} W m^{-2} sr^{-1} K^{-1} km^{-1}, $^{(e1)}$ In 10^{-2} mag, $^{(e2)}$ In 10^{-6}, $^{(e3)}$ In 10^{-8} W m^{-2} sr^{-1}.